

Phase Transitions in Biological Tissue Mechanics

by Junxiang Huang

B.S. in Mathematics, Wuhan University  
M.S. in Physics, Xiamen University

A dissertation submitted to

The Faculty of  
the College of Science of  
Northeastern University  
in partial fulfillment of the requirements  
for the degree of Doctor of Philosophy

November 28, 2023

Dissertation Committee

Prof. Dapeng Bi (advisor)

Prof. Herbert Levine

Prof. Armen Stepanyants

Prof. Calina Copos

## Acknowledgements

I would like to extend my heartfelt appreciation to my research mentor, Prof. Dapeng (Max) Bi, whose guidance led me into the fascinating realm of biological and soft matter physics. I deeply value Max's mentorship, his unwavering patience, and the constant encouragement he provided throughout this journey. Max is not only an exceptional researcher but also a dedicated mentor and a dependable collaborator. His experience and insight have been a constant help in completing my research goals. This dissertation owes its existence to Max's invaluable contributions and support.

I would also like to thank my committee members – Prof. Herbert Levine, Prof. Armen Stepanyants, and Prof. Calina Copos – for their constructive comments on my dissertation and for taking the time to serve on my thesis defense committee. I also thank my collaborators Prof. Herbert Levine, Prof. M Cristina Marchetti, Prof. Suzanne M Fielding, and James O Cochran.

I am grateful for the camaraderie and support extended to me by all my classmates and groupmates. Their collective efforts and shared experiences have enriched this academic journey in immeasurable ways.

Lastly, I want to convey my deepest gratitude to my parents and wife for their boundless love, unwavering support, and constant encouragement. I consider myself incredibly fortunate to have them as pillars of strength in my life. Their presence has been a source of immense comfort and inspiration throughout this journey, and I am forever thankful for their enduring presence in my life.

## Abstract of Dissertation

Biological systems exhibit states analogous to physical states of matter such as solid, liquid, and gas, resulting from cellular interactions that manifest in macroscopic properties such as fluidity, rigidity, and resistance to shape and volume changes [1]. These transitions, where tissues change their structural and functional states, are key to phenomena like embryogenesis, wound healing, and tumor development. In this dissertation, we employ numerical frameworks to probe the phase transition and mechanical responses of dense biological tissues under varying conditions. First, we employ a Voronoi-based vertex model to investigate the nonlinear mechanical behavior of dense biological tissue subjected to shear deformations. We show that solid-like tissues exhibit pronounced nonlinear tendencies and stress-stiffening behaviors, aligning with empirical observations, and fluid-like tissues could undergo strain-induced solidification upon surpassing a critical strain threshold. A mean-field theory is proposed to explain these phenomena. In addition, we introduce an Active Finite Voronoi (AFV) model, which exhibits an additional non-confluent phase than traditional vertex models, enabled by the potential for intercellular gaps. This uncouples the confluence transition from tissue aggregation and glassy transitions. This rich phase diagram has been systematically studied. The study employs a combination of theoretical modeling and computational simulations, leveraging tools from non-equilibrium statistical mechanics, soft matter physics, and topological mechanics. This comprehensive approach allows us to span a diverse range of topics within the realm of biophysics.

## Table of Contents

Acknowledgements . . . . .	2
Abstract of Dissertation . . . . .	3
Table of Contents . . . . .	4
List of Figures . . . . .	6
Chapter 1 : Introduction and Background . . . . .	13
1.1 Biological Tissues as Active Matter . . . . .	13
1.2 Epithelial Tissues . . . . .	15
1.2.1 Epithelial Tissue Morphogenesis . . . . .	16
1.2.2 Computational Models for Epithelial Tissues . . . . .	18
1.2.3 Phase Transitions in Epithelial Tissues . . . . .	20
Chapter 2 : Rheology of Biological Tissues . . . . .	24
2.1 Voronoi Model under Simple Shear . . . . .	25
2.2 Nonlinear Shear Response . . . . .	29
2.3 Strain-driven Solidification . . . . .	34
2.4 Correlating Mechanical Response and Cell Shapes . . . . .	37
2.5 Mean-Field Model of Sheared Tissues . . . . .	44
2.6 Discussion and Conclusion . . . . .	49
Chapter 3 : Beyond Confluence: A Voronoi-based Model with Extracellular Spaces . . . . .	51
3.1 Active Finite Voronoi (AFV) Model . . . . .	55
3.2 Motility and Cell-Cell Interactions Induce a Clustering Transition . . . . .	60

3.3	Epithelial-Mesenchymal Transition Driven by Cell-Shape Changes and Motility . . .	68
3.4	Glassy Dynamics in Confluent and Non-Confluent Regimes . . . . .	71
3.5	Phase Diagram of the AFV Model . . . . .	74
3.6	Discussion and Conclusion . . . . .	77
Chapter 4 : Summary and Outlook . . . . .		80
Bibliography . . . . .		82

## List of Figures

Figure 1.1 <b>Examples of epithelial tissue morphogenesis.</b> (a) Formation of the ventral furrow in the Drosophila embryo. For each time, the single-plane images (top), YZ projections (side), and maximum intensity projections (bottom) are shown with a scale bar of 10 mm. Image reproduced from [19]. (b) A schematic illustration of the molecular mechanisms of cell shape adaption in epithelial tissue. Upon cell-cell contact, cells adapt their shapes via actin-myosin contractility (green arrows) and adhesion (blue arrows) in response to mechanical forces. Image reproduced from [20]. (c) Villus—longitudinal section in mice gut with the scale bar being 40 mm. Boxed regions are shown in high magnification. Image reproduced from [21]. . . . .	17
Figure 1.2 <b>Schematic diagram of 2D and 3D vertex models reproduced from [27].</b> (a) The apical view and cross-sectional representation of the wing imaginal disc epithelium in the Drosophila embryo is depicted. (b) A schematic illustration of an epithelial tissue is presented. Cytoskeletal elements exert intracellular forces, which are mechanically transmitted to adjacent cells and the basement membrane. (c, d) Apical vertex models delineate epithelial cells by their apical surfaces, which assume polygonal forms in 2D or 3D. (e) In 2D lateral vertex models, cells are represented by their lateral cross-sections. (f) In 3D vertex models, the tissue is represented by its apical and basal geometry. . . . .	19

Figure 1.3 <b>Density-driven and density-independent phase transitions in biological tissue models.</b>	20
(a) The particle jamming model predicts that a jamming transition in tissue could result from increased cell density, increased cell-cell adhesion, or decreased cell motility. Image reproduced from [28].	
(b) Using a model parameter $p_0$ that encodes cell–cell adhesion and cortical tension, the phase diagram of the vertex model can be presented in one dimension, providing an explanation for mechanical rigidity transitions in confluent tissues under constant cell density. Image reproduced from [29].	
Figure 2.1 Illustration of the Lees-Edwards boundary conditions applied in a vertex model simulation under simple shear deformation. The central highlighted region depicts a lattice with cells outlined in blue and vertices marked by pink dots, undergoing shear deformation indicated by the solid black arrows. The periodic boundary conditions are visualized by the tiling of the central lattice configuration in the surrounding space, allowing for the seamless transition of cells across opposite boundaries. The shear strain is denoted by $\gamma$ and $L$ represents the linear dimension of the simulation box.	27
Figure 2.2 Representative tissue stress trace and tension network snapshots with $p_0 = 3.75$ as an example of $p_0 < p_0^*$ . The strains of snapshots are $\gamma = 0, 1, 4$ , respectively, which are marked by red dots on the trace. The snapshot edges are color-coded according to the edge tension defined by Eq. (2.3).	29
Figure 2.3 The shear modulus $G$ vs. stress $\sigma$ at various $p_0 < p_0^*$ and $\kappa_A = 0$ .	31
Figure 2.4 Rescaled $G/G_0$ vs $\sigma/\sigma_c$ for the same set of $p_0$ values as in Fig. 2.3.	33
Figure 2.5 Representative tissue stress trace and tension network snapshots with $p_0 = 3.89$ as an example of $p_0 > p_0^*$ . The strain values of the sample snapshots are $\gamma = 0, 0.65, 2.66$ , respectively, which are marked by red dots on the trace. The snapshot edges are color-coded according to the edge tension defined by Eq. (2.3).	34

Figure 2.6 <b>Strain-driven rigidity transition.</b> (a) The shear modulus $G$ near the onset of the strain-driven solidification for $p_0 = 3.84$ and varying values of area elasticity $\kappa_A = 0, 10^{-10}, 10^{-8}, 10^{-6}, 10^{-4}, 0.05$ . Here, the colors correspond to the legend in panel (b). <b>Inset:</b> The value of $G$ immediately below and above the transition show a gap that narrows with increasing $\kappa_A$ . The dashed line indicates a slope of 1 on the log-log plot. The transition is discontinuous in $G$ at $\gamma = \gamma_C$ (b) The Non-affinity parameter $\Delta\Gamma$ near the onset of the transition for $p_0 = 3.84$ and varying values of area elasticity $\kappa_A$ . Maps of non-affine cell displacements before (c) and at (d) the onset of strain stiffening for $\kappa_A=0$ .	36
Figure 2.7 <b>Tissue stress and cell shapes under shear.</b> (a) A plot of $\sigma$ as a function of $\gamma_{\text{true}}$ for different $p_0$ 's spanning the solid and liquid regimes at $\kappa_A = 0$ . (b) The cell shape index $q$ vs the true strain $\gamma_{\text{true}}$ for the same range of $p_0$ as in (a).	42
Figure 2.8 <b>Correlating cell shapes and tissue stress.</b> (a) A plot of $\delta q \equiv q - p_0^*$ vs. $\sigma$ for various values of $p_0$ as indicated with $\kappa_A = 0$ . (b) Replotting of the data from (a) using the universal scaling ansatz (as defined in Eq.(2.19)). Here $\Delta = 3/2$ and $\phi = 1$ .	43

Figure 2.9 **The mechanical response of epithelial tissue to applied shear strain as a function of  $p_0$  with  $\kappa_A = 0$ .** (a) The average stress  $\langle \sigma \rangle$  as a function of strain for tissues. The vertical arrows indicate the corresponding critical strain  $\gamma_C$ , where  $\langle \sigma \rangle$  starts to become positive. The horizontal dashed lines are the yield stress  $\sigma_{yield}$  of tissues, which is the average of steady-state stress. (b) The critical strain  $\gamma_C$  as function of  $p_0$ . The solid black curve is the median over 28 samples, and the gray shadow shows the standard deviation. The arrow indicates the transition point at  $p_0^* = 3.81$ . (c) The yield stress  $\sigma_{yield}$  as function of  $p_0$  averaged over 28 samples at  $\gamma$  ranging from 1 to 5. . . . . 44

Figure 2.10 **Illustration of the Mean Field Theory (MFT).** (a) We use a single polygon as a representative cell in the MFT. When the perimeter of a polygon is larger than that of its regular counterpart, deformations can lead to a family of isoperimetric shapes defined by the contours shown for a 5-sided polygon at various values of  $P > P_{reg} \approx 3.812$ . (b) The MFT energy landscape as a function of  $(D_{xx} - 1, D_{xy})$  for  $t > 0$  has a unique ground state at  $D_{xx} = 1, D_{xy} = 0$ , as depicted in Eq.(2.23). (c) The MFT energy landscape as a function of  $(D_{xx} - 1, D_{xy})$  for  $t < 0$  has degenerate ground states which are connected by Goldstone modes in the  $\delta\theta$  direction, as depicted in Eq.(2.23). . . . . 47

Figure 3.1 The static phases of the Finite Voronoi model (FVM) adapted from [42]. The shown snapshots are systems starting from the same initial condition with  $N = 100$  cells and zero temperature. Green lines are straight edges between adjacent cells, and red lines are the non-contacting edges in the form of circular arcs. The purple line below each configuration is of length  $R = 1$  to see the different scales. . . . . 56



Figure 3.4 <b>The fluctuation in <math>N_{GC}/N</math> for dispersed states.</b> (a) Two sample $N_{GC}/N$ traces at $v_0 = 1$ . The solid lines correspond to realizations of $P_0 = 4$ and $P_0 = 8$ , respectively. The cyan dashed line indicates the average value of $P_0 = 8$ as visual aids. (b) The $N_{GC}/N$ average values of different $P_0$ at $v_0 = 0.1$ and $v_0 = 1$ , respectively, with the shaded band representing the standard deviation. (c) The autocorrelation time of the giant cluster size, $\tau_{N_{GC}}$ , at different $P_0$ and $v_0 = 1$ . For $P_0 < 5$ , the $\tau_{N_{GC}}$ values go to infinity and are not displayed on the plot. . . . .	66
Figure 3.5 <b>Tissue confluency properties.</b> (a) $\Omega$ [defined in Eq. (3.10)] as a function of $v_0$ for various $P_0$ values ranging from 4 to 8.8 with an increment of 0.2. The black arrow indicates the curves ordered with increasing $P_0$ . (b) Tissue confluency phase diagram for $\Lambda = 0.2$ in the $v_0$ - $P_0$ plane. The marker color indicates the tissue $\Omega$ value. The black dashed line corresponds to $\Omega = 0.5$ and is used as a boundary between the epithelial/confluent state and the mesenchymal/nonconfluent state. (c-d) Illustrative snapshots of a nonconfluent/confluent hexagonal tissue, respectively, were used for our mean-field analysis. . . . .	68
Figure 3.6 <b>Tissue glassy properties.</b> (a) MSD traces for different $P_0$ ranging from 4 to 8 with $\Lambda = 0.2$ and $v_0 = 0.4$ . (b) MSD trace for different $v_0$ with a fixed $P_0 = 5.6$ . (c) shows $D_{eff}$ as a function of $v_0$ for different $P_0$ . The black dashed line corresponds to $D_{eff} = 10^{-8}$ . (d) Tissue diffusivity phase diagram as a function of $P_0$ and $v_0$ . Orange data points correspond to glassy tissue with vanishing $D_{eff}$ ; green points correspond to flowing tissues (finite $D_{eff}$ ). . .	72
Figure 3.7 The cumulative T1 number traces for different $P_0$ ranging from 4 to 8 with $\Lambda = 0.2$ and $v_0 = 0.4$ . . . . .	73

Figure 3.8 **Summary of the phase diagram.** (a) shows the phase diagram with all three phase boundaries on the  $P_0$ - $v_0$  plane for  $\Lambda = 0.2$ . It is qualitatively robust for all values of  $\Lambda$ . (b) shows sample snapshots of four phases. The  $(P_0, v_0)$  values for each state are: Clustered Epithelial phase (4, 0.1); Clustered Mesenchymal phase (8.8, 0.1); Dispersed Epithelial phase (4.4, 2.6); Dispersed Mesenchymal phase (8.8, 2.6). Note that a clustered state could be glassy or unjammed, but a dispersed state must be unjammed. . . . . 74

# **Chapter 1**

## **Introduction and Background**

### **1.1 Biological Tissues as Active Matter**

Distinguished from its inert counterpart, the term “active matter” encompasses a diverse array of non-equilibrium systems wherein constituent elements or individual agents engage in the conversion of free energy into kinetic motions and stresses. An expedient method for categorizing active matter lies in scrutinizing the underlying energy conversion process. Classification based on energy types reveals two principal categories: biological systems, which encompass phenomena such as the collective behavior of animal flocks or herds, aggregations of cells, and elements of the cellular cytoskeleton; and synthetic systems, exemplified by entities such as artificial self-propelled particles, camphor, droplet swimmers, and magnetic rollers [2, 3, 4].

While inert matter is known to undergo phase transitions upon the introduction of external temperature tuning or shear stress, active systems possess the intriguing capacity to exhibit new and rich unexplored phases beyond the equilibrium regime, which have drawn attention from researchers across different disciplines [5]. Notably, many active systems exhibit large-scale spatial and/or temporal organized structures with rich and intriguing properties. For instance, a dense swarm of bacteria could flow akin to a living fluid, thereby exhibiting complex regular patterns via self-organization [6]. Suspensions of active colloids can self-assemble into ordered structures with emergent properties, showcasing the potential for harnessing active matter in materials design [7]. Furthermore, active matters share similarities with bird flocks in terms of that coordinated motion emerges from individual agents’ interactions, exemplifying nature’s remarkable ability to achieve collective behavior in complex systems [8]. The emergence of these unique phenomena within active systems has ignited considerable interest in the scientific community, as they represent a de-

parture from conventional equilibrium behavior and offer new avenues for exploration in various fields of research.

In the past decades, a large portion of this growing interest has focused on living active matters, including attempts to bridge the gap between inanimate and living systems. As Erwin Schrodinger insightfully discussed in his landmark work, ‘What is Life? The Physical Aspect of the Living Cell’ [9], living organisms are inherently active-matter systems that consume energy to generate motion and force. This convergence in properties between living and non-living matters has prompted researchers to explore a universal framework that could elucidate the dynamics governing both domains. Once we delve into the intricacies of living organisms, it becomes apparent that they are complex systems composed of specialized cells and extracellular materials, organized not randomly but in regions of high density. Especially in many tissues that have a minimal amount of extracellular matrix, the cells are in close mechanical contact with one another, resulting in the formation of a sustained network structure at their boundaries. These dense biological tissues can be broadly categorized into four primary types: 1) Epithelial tissue, forming the protective covering or lining of all internal and external body surfaces, is characterized by tightly packed cells that serve as barriers against pathogens, mechanical injury, and fluid loss. This type of tissue will be the main focus of the current thesis. 2) Connective tissue is the most abundant and diverse type, which supports, binds and protects organs. It is composed of fewer cells embedded in an extracellular matrix of fibers and ground substance. 3) Muscle tissue, specialized for contraction, facilitates movement and force. 4) Nervous tissue, central to the nervous system, comprises neurons and glial cells. These biological tissues are subject to a diverse array of physical and chemical forces, demonstrating how structural and functional properties are influenced by external factors. For instance, muscles and bones are continuously exposed to mechanical stress, while blood vessels and hearts endure dynamic fluid flow and pressure variations. To fulfill complex functions and react to varying environments, dense biological tissues exhibit a complex network of various cell types and

supporting extracellular matrix. For instance, in cardiac tissue, the muscle cells specialize in contraction and blood pumping, while endothelial cells form the linings of blood vessels, showing the intricate interplay of different cellular functions. Similarly, in neural tissues, neurons are responsible for transmitting electrical signals, with glial cells providing essential structural support and nourishment [10]. The heterogeneity of cells within a dense biological tissue creates a dynamic interplay of functions that are essential for the tissue's overall health and survival [11]. The extracellular matrix contributes significantly by providing mechanical support, influencing cell growth and differentiation, and regulating cellular behavior [12].

## 1.2 Epithelial Tissues

All surfaces of organs and body cavities are covered by confluent and dense biological tissues, of which the most common form is epithelial tissues, consisting of collectives of epithelial cells. Within epithelial tissues, typically composed of one to a few cell layers in thickness, cells are tightly connected to nearby ones via intercellular junctions, establishing stable networks of protective cell-cell interfaces. These tissues, fundamental to the architecture of multicellular organisms, serve as protective barriers, sensory interfaces, intermediaries of nutrient transportation and absorption, and more.

Epithelial tissues play an important role in various developmental processes within the body. For instance, during embryonic development, the neural tube, which eventually gives rise to the brain and spinal cord, forms from an epithelial sheet that rolls into a tube [13]. Any disruption in the epithelial cells during this process can lead to neural tube defects, highlighting the critical importance of epithelial tissues in development. In addition, epithelial tissues also frequently play pivotal roles in pathological such as cancer, inflammation, and infection [14, 15, 16]. These interesting properties render epithelial tissue a great research object for elucidating the intricate interactions and mechanisms that have piqued the interest of both biologists and physicists. Recent advancements in cell imaging, manipulation technologies, and deep learning methods have been

revealing more and more new phenomena of epithelial tissue behaviors, allowing a more in-depth comprehension [17, 18].

### 1.2.1 Epithelial Tissue Morphogenesis

Epithelial tissue morphogenesis is commonly used in biology and developmental biology to describe a complex developmental process that entails the reorganization and differentiation of epithelial cells to form the diverse array of tissues and organs seen in multicellular organisms [22, 20]. During the process of epithelial tissue morphogenesis, epithelial cells coordinate their movements, shape changes, and functional differentiation in response to both intrinsic genetic programs and signals from their environment, and organize themselves into the various structures of the body, involving multiple signaling pathways, cell-cell interactions, and mechanical forces.

One of the most well-studied examples of epithelial tissue morphogenesis is the formation of the ventral furrow in the fruit fly (*Drosophila melanogaster*) during embryonic development. As shown in Fig. 1.1(a), at the onset of this process, the epithelial cells form an ellipsoidal shape around a yolk. Then on a timescale of about 20 minutes, this process involves a coordinated series of movements where cells in the ventral region of the embryo constrict their apical surfaces, leading to an inward folding of the tissue that is fundamental for subsequent steps of gastrulation [23, 19]. To complete such a series of highly controlled steps involving cell proliferation, migration, adhesion, and apoptosis, the contacting cells need to self-organize and coordinate. Fig. 1.1(b) shows that epithelial cells change their shapes and form tissue structure during this morphogenetic process driven by actin-myosin contraction and cellular adhesion mediated by cadherin proteins [20].

In addition to embryonic development, epithelial morphogenesis is equally pivotal in adult organisms, as evidenced by the cellular dynamics within the mammalian gut epithelium. This tissue exhibits one of the most rapid turnover rates, characterized by perpetual cycles of cellular proliferation, differentiation, and programmed cell death (apoptosis), which collectively sustain the structural and functional integrity of the intestinal lining. This regenerative capacity is not only

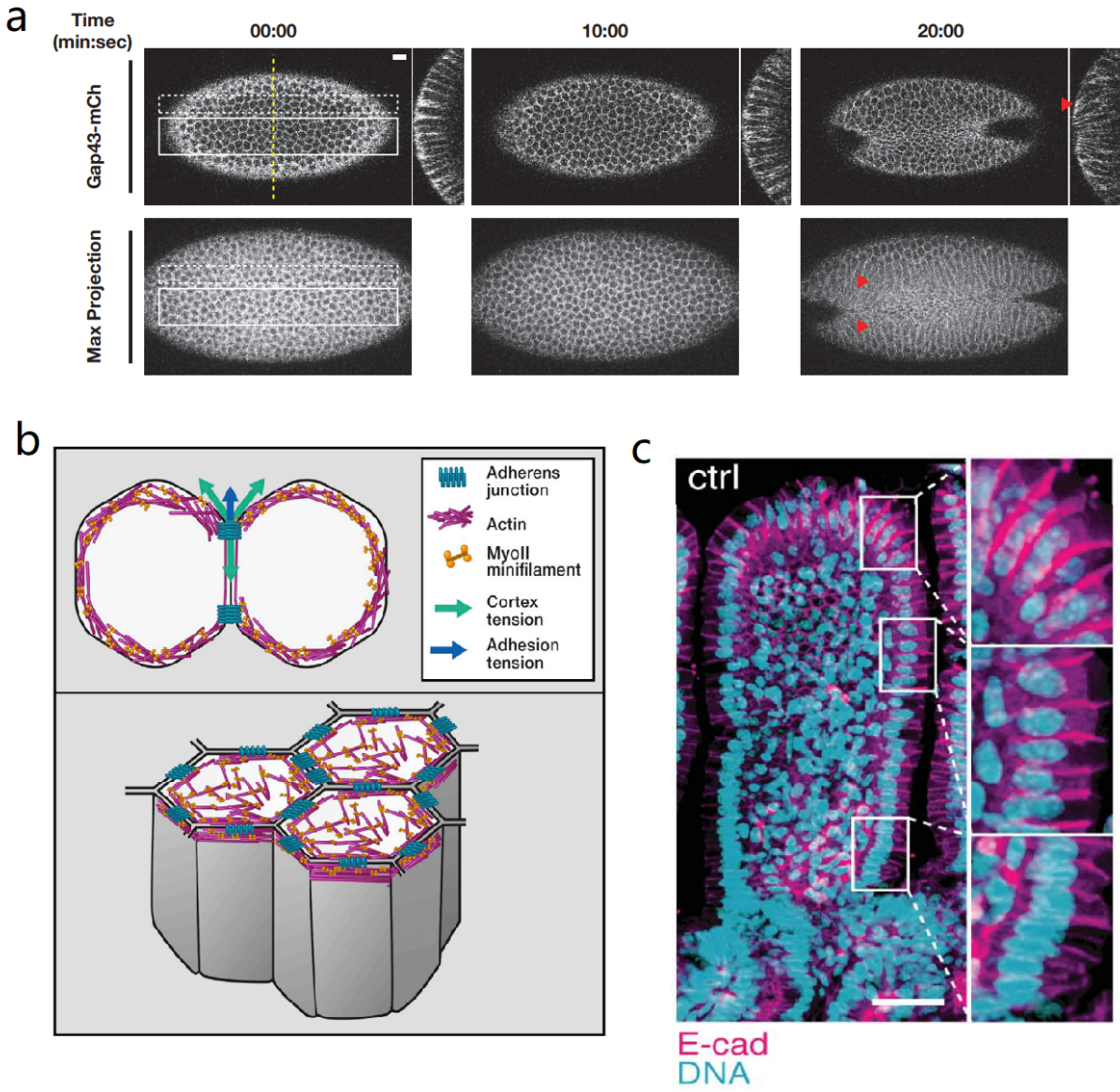


**Figure 1.1: Examples of epithelial tissue morphogenesis.** (a) Formation of the ventral furrow in the Drosophila embryo. For each time, the single-plane images (top), YZ projections (side), and maximum intensity projections (bottom) are shown with a scale bar of 10 mm. Image reproduced from [19]. (b) A schematic illustration of the molecular mechanisms of cell shape adaption in epithelial tissue. Upon cell-cell contact, cells adapt their shapes via actin-myosin contractility (green arrows) and adhesion (blue arrows) in response to mechanical forces. Image reproduced from [20]. (c) Villus—longitudinal section in mice gut with the scale bar being 40 mm. Boxed regions are shown in high magnification. Image reproduced from [21].

crucial for the absorption of nutrients but also plays an integral role in preserving the barrier function of the gut, thereby preventing pathogenic invasion and disease emergence. Figure 1.1(c) delineates the highly ordered architecture of the gut epithelium, with particular emphasis on the villi—projections lined with a continuous epithelial sheet that undergoes constant renewal. Traditionally, this gut turnover is assumed to be driven by mitotic pressure from the stem cells within the intestinal crypts. Recent literature reports that active cellular migration is also a significant contributory mechanism [21], indicating that the synergy between mitotic proliferation and directed cell movement orchestrates a complex and efficient system for tissue maintenance.

### 1.2.2 Computational Models for Epithelial Tissues

Epithelial tissues are an excellent research object for understanding dense biological tissue because of their unique organization and function. Their distinctive attributes, such as polarity, cell-cell adhesion, and intercellular communication, render them an interesting model to study the underlying mechanisms that govern tissue formation and maintenance. However, many experimental methodologies, while providing a wealth of data, usually face the challenge of dissecting the complex interplay of forces at the cellular and subcellular levels. This complexity underscores the need for computational models that can complement experimental data, offering a more granular understanding of the dynamics at play within epithelial tissues.

The vertex model simulation is a particularly potent tool in this domain. In the realm of material science and fluid dynamics, the vertex model was originally used to study foam structures, for example, the dynamics of soap film collisions or ‘flips’ in two-dimensional foams [24, 25]. Due to the vertex model’s capacity to unravel the intricate interplay of forces and configurations at the microscopic level, researchers then applied it in the study of cellular patterns and dynamics in epithelial tissues by mapping the physical properties of cells, such as their shape, elasticity, and adhesion, onto the parameters used in the vertex model [26]. As shown in Fig. 1.2, by representing epithelial tissues as a tessellation of polygons, where each vertex corresponds to a cellular junc-

tion, this model offers a unique perspective on tissue mechanics. The interactions among these vertices, governed by a set of equations, can replicate the mechanical and topological characteristics inherent to epithelial tissues. One of the primary motivations for employing the vertex model is its adeptness at capturing the equilibrium of forces, including those of adhesion, tension, and cortical contractility. Such forces are not only central to maintaining tissue integrity but also play a decisive role in the dynamic processes that these tissues undergo.

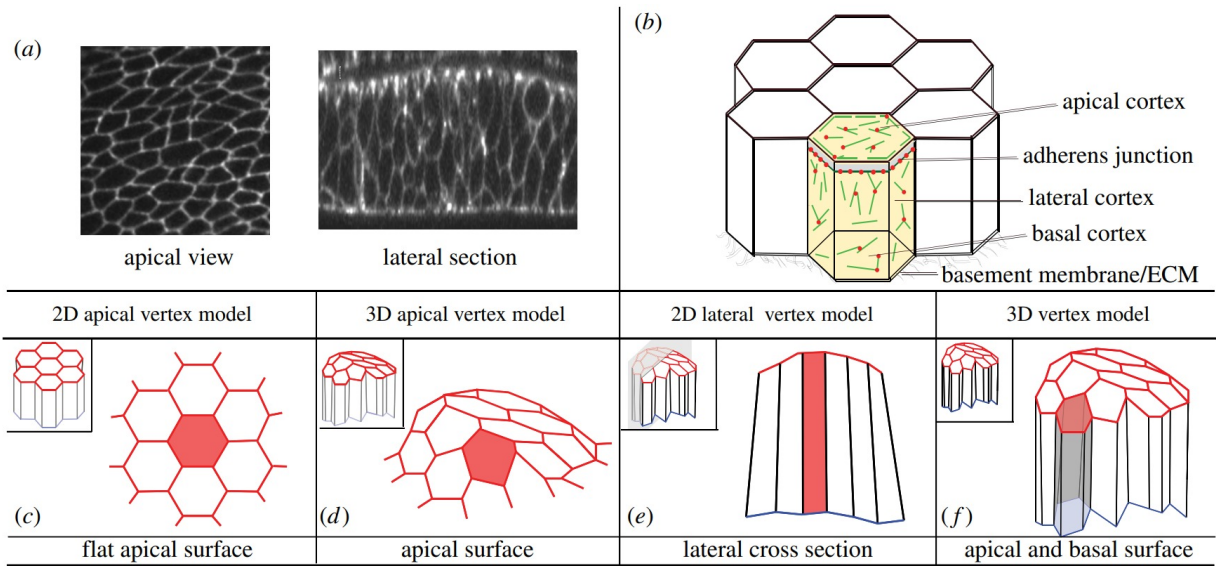


**Figure 1.2: Schematic diagram of 2D and 3D vertex models reproduced from [27].** (a) The apical view and cross-sectional representation of the wing imaginal disc epithelium in the *Drosophila* embryo is depicted. (b) A schematic illustration of an epithelial tissue is presented. Cytoskeletal elements exert intracellular forces, which are mechanically transmitted to adjacent cells and the basement membrane. (c, d) Apical vertex models delineate epithelial cells by their apical surfaces, which assume polygonal forms in 2D or 3D. (e) In 2D lateral vertex models, cells are represented by their lateral cross-sections. (f) In 3D vertex models, the tissue is represented by its apical and basal geometry.

The vertex model provides a versatile framework adaptable to specific biological contexts. Various parameters, such as cell proliferation rate, apoptosis rate, or differential adhesion, could be incorporated to simulate different processes of interest, from tissue growth and gut turnover to tissue folding and tumor invasion.

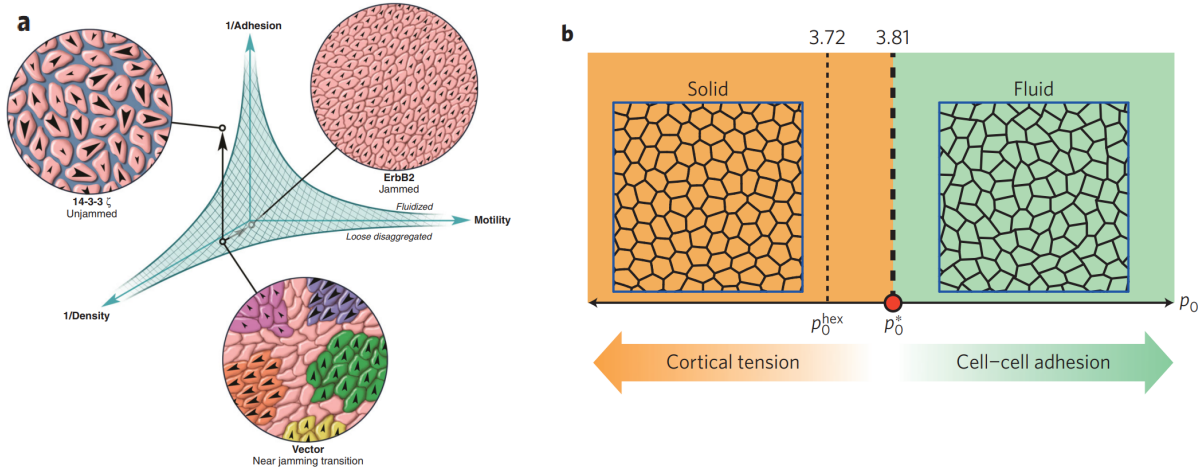


**Figure 1.3: Density-driven and density-independent phase transitions in biological tissue models.** (a) The particle jamming model predicts that a jamming transition in tissue could result from increased cell density, increased cell-cell adhesion, or decreased cell motility. Image reproduced from [28]. (b) Using a model parameter  $p_0$  that encodes cell-cell adhesion and cortical tension, the phase diagram of the vertex model can be presented in one dimension, providing an explanation for mechanical rigidity transitions in confluent tissues under constant cell density. Image reproduced from [29].

### 1.2.3 Phase Transitions in Epithelial Tissues

Over the past decades, people have revealed many non-trivial rheological properties and phase transitions of epithelial tissues. For example, it has been observed that tissues can enter a ‘glassy’ state in which cells are caged by their neighbors and have very limited ability to rearrange. These phase transitions in epithelial tissues usually occur as a result of changes in the mechanical properties of the tissue, such as changes in cell-cell adhesion and communication, changes in the cytoskeleton, or changes in the mechanical properties of the extracellular matrix. Studying the phase transitions that govern tissue behavior can provide insight into the development and evolution of these tissues. For instance, studying the phase transitions during gut development tells us how the gut has evolved to absorb nutrients and protect the body from harmful pathogens.

Additionally, studying phase transitions in epithelial tissues as adaptations to different physiological conditions or environments could reveal the underlying causes of related diseases. For

example, primary human bronchial epithelial tissues could undergo jamming transitions with increased air pressure that mimics asthmatic bronchospasm. The loss of cell-cell adhesion and communication is critical to metastasis. Changes in the mechanical properties of the extracellular matrix can contribute to the development of fibrosis and other diseases.

Researchers have revealed characteristics of glassy dynamics and rigidity transitions in in-vitro dense biological tissues [30, 31, 32, 33], which are identified as related to physiological functions and multiple pathologies. For example, in homeostatic circumstances, the epithelial collective forms barriers restricting the passage of solutes and integrating the cytoskeletons of constituent cells into a mechanical syncitium by remaining effectively solid-like and sedentary. On the other hand, during morphogenesis, remodeling, or wound healing, the epithelial collective can repair and reform by becoming fluid-like and migratory via a rigidity transition [34]. In addition, it is well known that tumors are stiffer than their surrounding tissues, making them detectable by clinical exams and magnetic resonance elastography [35].

These experiments have attracted increasing interest from soft-matter physicists to understand the underlying mechanics of these biological materials. Even though cells have complex inner structures and the cell nucleus and other organelles have contributed to the collective mechanical properties of tissues at some level, the mechanical properties of many epithelial layers can be well approximated by considering only the network of interfaces without details of organelle structures. This allows physicists to build simulation models for dense biological tissues with a reasonable number of variables to study the mechanical and dynamical properties.

Mongera et al. have discovered recently that during in vivo experiments of zebrafish embryo development, the embryo tissue undergoes a rigidity transition in the process of the vertebrate body axis formation, revealing that rigidity transitions play a functional role in embryonic development [36]. Mitchel et al. reported that there are two ways of tissue rigidity transition in differentiated primary human bronchial epithelial cells: one is partial epithelial-to-mesenchymal

transition (pEMT), where junctional integrity and layer integrity are disrupted without building of cooperative motion in a long timescale; the other is unjamming transition (UJT), where cells shape become elongated and cooperative motion increases over time [37].

As with other living systems or complex system research, the experimental study of biological tissues has to deal with genetic heterogeneity, random noise, and measurement limitations. To identify the essential elements and understand the rigidity transition theoretically, people have developed various models describing a dense cell tissue that fills the two-dimensional space with packing fractions equal to 1, as the most common and simplest state a biological tissue is a homogeneous confluent phase where there is no free space between any of the cells which share identical to similar properties. Examples include the cellular Potts model [38], the vertex model [39], the Voronoi model [40, 41], and other variants [42, 43, 44]. In most of these models, cell dynamics and mechanics are governed by an effective energy function in terms of cell morphological properties such as sectional area, edge length, or perimeter. In the vertex-based model, the target shape index as a parameter is shown to drive unjamming transition at a critical point 3.81 [29], which are tested in multiple in-vitro experiments [45, 46].

As the examples discussed show, epithelial tissues not only provide essential mechanical support and stability at these transition zones but also actively participate in the dynamic remodeling of tissue structures in response to varying mechanical stresses. They exhibit a remarkable balance between solid-like properties for structural stability and fluid-like properties for adaptability, reflecting the dynamic demands of biological systems. The solid-like characteristics provide essential support, protection, and mechanical signaling, crucial for maintaining the functional integrity of organs and facilitating mechanical signaling. Conversely, fluid-like properties allow for cell migration, essential in processes like wound healing and developmental morphogenesis, enabling tissues to adapt and reorganize in response to physiological demands or environmental stress. Epithelial tissues are adept at sensing changes in tissue stiffness and rigidity, adapting their behavior

through processes like proliferation, differentiation, or apoptosis. This dynamic interplay between rigidity transitions and the mechanical deformation and dynamic shape changes of biological tissues adds a layer of complexity to our understanding of biomechanics, intricately linked with the functional and regulatory processes of the body.

To further understand the mechanical properties of epithelial tissues, we aim to study them in the context of their interactions with rigidity transitions and associated dynamic changes. This approach will provide insights into how these tissues respond and adapt to the shifts between rigidity and flexibility, crucial for their function and behavior. We plan to investigate the questions in three aspects: First, we will use a Voronoi-based implementation of the vertex model to quantitatively study the mechanical response of dense biological tissue to large deformation, by applying incrementally increasing external strain and then allow the tissue to relax to a force balanced state. Second, we plan to lift the space-filling restriction of the vertex model and study how rigidity transition happens in the non-confluent regime. Third, by defining different cell phases by qualitative changes in division rate, cell size and shape, and collective motion, we will try to understand how in-vitro cells in different phases emerge, interact, and transit.

## Chapter 2

### Rheology of Biological Tissues

The statistical rigidity of a material, such as epithelial tissue, can be indicated by its shear modulus  $G$ , which quantifies the material's resistance to shear deformation. When a shear force is applied to a material, the shear modulus measures the ratio of the shear stress  $\sigma$  to the shear strain ( $\gamma$  for simple shear or  $\epsilon$  for pure shear). A positive shear modulus indicates a rigid material that resists shape changes, while a zero shear modulus suggests a fluid-like material that can change shape without costing energy. Similar to fiber networks and spring networks [47], in biological tissues a rigidity transition may be indicated by a sudden jump in the shear modulus, transitioning from a state of virtual quiescence to a finite positive value.

Previous theoretical studies have calculated tissue shear modulus  $G$  using the Born-Huang formulation [48], which makes the harmonic approximation: for tissues at energy minimum states, the potential energy of the tissue is expanded in a Taylor series up to the second-order term, and the shear modulus is obtained based on this linear response to an infinitesimal affine strain  $\delta\gamma \rightarrow 0$  [49]. In 2015, Bi et al. reported that in confluent tissues with constant cell density, changes in cell-cell adhesion and cortical tension can induce a rigidity transition, signaled by the vanish of shear modulus and energy cost of cell rearrangements [29]. In 2019, Yan and Bi analyzed the eigenvalues of the Hessian matrix, which is a classic approach in linear response theory and is formed by the second derivatives of the potential energy with respect to the vertex positions in the tissue. As the presence of zero eigenvalues in the Hessian matrix corresponds to ‘floppy modes’ or ‘zero modes’ that allow deformations of the system without changes in the total energy, the number of floppy modes serves as a rigidity order measure that distinguishes between rigid and fluid states of the tissue, and a fluid-to-solid transition driven by multicellular rosette density and intracellular tensions is identified [43]. Interestingly, such a transition can also be induced by the heterogeneity

in single-cell properties: even if the overall softness of the cells increases, the tissue could exhibit increasing rigidity when the statistical fluctuations increase, which provides a possible explanation for the fact that tumor cells are in general softer than healthy cells but tumors are usually more rigid than surrounding tissues [50].

It is noteworthy to emphasize that, in a manner analogous to fiber networks which exhibit enhanced rigidity in response to the application of external strain, experiments have attested to the suspended epithelial monolayer's propensity to display strain-stiffening behavior [51]. This intriguing parallel between biological tissues and structural networks underscores the pivotal role played by topological connectivity in dictating their mechanical response. To gather more insight to elucidate fundamental principles governing the rigidity transitions in biological tissues and understand the interplay between structural configurations and mechanical properties in diverse material systems, we will use a numerical model to study the mechanical response of biological tissues under shear deformations [52]. Moreover, the previous studies mentioned above investigated the shear modulus exclusively under linear response assumption, which limits the validation of the conclusions to small perturbations. We would like to overcome this limitation and study the exact mechanical response of a sheared tissue involving large deformations and nonlinear effects.

## 2.1 Voronoi Model under Simple Shear

To study the response of biological tissues to externally imposed shear strain, we adopt a minimal Voronoi-based model, within which each cell  $i$  is endowed with a reference point  $\mathbf{r}_i$ , and it contains all the space that is closest to its reference point, i.e., cell shape is determined by the corresponding Voronoi tessellation. The degrees of freedom are the cell reference point positions. The resulting network of polygons is shown to be a good description of a confluent epithelium at a coarse-grained level [39, 26].

In previous papers [39, 29, 40], the total effective energy functional, which governs the me-

chanics of the cell layer, is expressed for a  $N$  cells' system as

$$E(\{\mathbf{r}_i\}) = \sum_{i=1}^N K_A(A_i - A_{i,0})^2 + K_P(P_i - P_{i,0})^2, \quad (2.1)$$

where cell areas  $\{A_i\}$  and perimeters  $\{P_i\}$  are functional of the positions of cell reference points  $\{\mathbf{r}_i\}$ .  $\{A_{i,0}\}$  and  $\{P_{i,0}\}$  are respectively the preferred areas and preferred perimeters.  $K_A$  and  $K_P$  are the area and perimeter elasticities. The first term, quadratic in the cell areas  $\{A_i\}$ , originates from the incompressibility of cell volume, giving rise to a 2D area elasticity constant  $K_A$  and preferred area  $A_0$  [39, 26]. The second term quadratic in the cell perimeters  $\{P_i\}$  arises from the contractility of the cell cortex, with an elastic constant  $K_P$  [39]. Here  $P_0$  is the target cell perimeter [29], representing the interfacial tension set by the competition between the cortical tension and the adhesion between adjacent cells [26].

To focus on the effect of applied shear strain rather than the heterogeneity between cells, here it is reasonable to assume that the parameters  $K_A, K_P, A_0, P_0$  are uniform in a tissue. Then, since the value of  $A_0$  only affects the energy function by an unimportant additive constant, we set  $A_0$  to be the average area per cell  $\bar{A}$ . By choosing  $K_P\bar{A}$  as the energy unit and  $\sqrt{\bar{A}}$  as the length unit, the dimensionless energy can be written as

$$E = \sum_{i=1}^N \kappa_A(a_i - 1)^2 + (p_i - p_0)^2, \quad (2.2)$$

where  $\kappa_A = K_A\bar{A}/K_P$  is the rescaled area elasticity which controls the cell area stiffness as compared to the perimeter stiffness, as  $a_i = A_i/\bar{A}$  and  $p_i = P_i/\sqrt{\bar{A}}$  are the rescaled area and perimeter of the  $i$ th cell.  $p_0 = P_0/\sqrt{\bar{A}}$  is an important control parameter called the preferred cell shape index.

Then we impose quasi-static simple shear using Lees-Edwards boundary conditions. The Lees-Edwards boundary condition was first proposed by David Lees and Stuart Edwards in 1972 as a way to model the behavior of fluids in systems with shear flow [53]. It is a method used to simulate

the dynamics of systems with periodic boundary conditions, such as in molecular dynamics simulations. The basic idea behind the Lees-Edwards boundary condition is to apply a relative velocity between two opposite boundaries of the simulation box while keeping the other boundaries at a fixed position. This creates a shear flow within the simulation box, which can be used to model the behavior of fluids under shear stress. As the Lees-Edwards boundary condition provides a useful tool for understanding the behavior of fluids, granular materials, polymers, biological tissues, and other systems under shear flow, it is widely used in the field of soft matter physics, such as the study of the rheological properties of materials, including polymer melts or granular materials under shear, and complex fluids, such as suspensions and emulsions, in response to shear stress, and the blood flow through vessels [54]. Below is an example of pseudocode for implementing the Lees-Edwards boundary condition in a simple shear simulation:

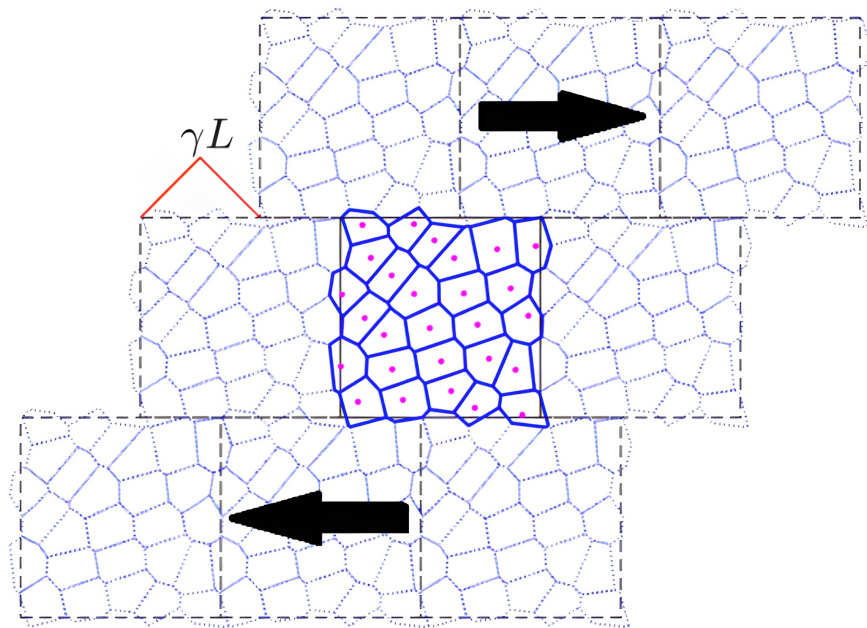


Figure 2.1: Illustration of the Lees-Edwards boundary conditions applied in a vertex model simulation under simple shear deformation. The central highlighted region depicts a lattice with cells outlined in blue and vertices marked by pink dots, undergoing shear deformation indicated by the solid black arrows. The periodic boundary conditions are visualized by the tiling of the central lattice configuration in the surrounding space, allowing for the seamless transition of cells across opposite boundaries. The shear strain is denoted by  $\gamma$  and  $L$  represents the linear dimension of the simulation box.

---

**Algorithm 1** Lees-Edwards boundary condition for quasi-static simple shear simulation

---

**Require:** Initial cell positions  $\{x_i, y_i\}$ ; number of steps; strain-step  $\Delta\gamma$ ; box size  $L_x$  and  $L_y$

**Ensure:**  $\gamma = 0$

```
1: for t in range(number of steps) do                                ▷ Loop for each time step
2:    $\gamma = \gamma + \Delta\gamma$ 
3:   for i in range(number of cells) do          ▷ Update position and apply boundary condition
4:      $x_i = x_i + \Delta\gamma * y_i$ 
5:      $x_i = x_i - \text{Floor}(x_i/L_x) * L_x$ 
6:   end for
7:   do energy minimization
8:   while doing energy minimization do
9:     for i in range(number of cells) do
10:      if  $y_i \geq L_y$  then                                ▷ Particle crosses top boundary
11:         $y_i = y_i - L_y$ 
12:         $x_i = x_i + \gamma * L_y$ 
13:      else if  $y_i < 0$  then                         ▷ Particle crosses bottom boundary
14:         $y_i = y_i + L_y$ 
15:         $x_i = x_i - \gamma * L_y$ 
16:      end if
17:       $x_i = x_i - \text{Floor}(x_i/L_x) * L_x$ 
18:    end for
19:  end while
20: end for
```

---

Starting from a strain-free ( $\gamma = 0$ ) force-balanced state, the strain  $\gamma$  is increased in increments of  $\Delta\gamma = 2 \times 10^{-3}$ , while cell center positions are subject to an affine displacement  $\Delta\mathbf{r}_i = \Delta\gamma y_i \hat{x}$ . Following each strain step, Eq. 2.2 is relaxed using the FIRE algorithm [55] until all forces  $\mathbf{F}_i \equiv -\partial E / \partial \mathbf{r}_i$  are vanishingly small ( $< 10^{-14}$ ). We used 84 random initial configurations for each parameter choice and  $N = 400$  cells unless otherwise indicated.

## 2.2 Nonlinear Shear Response

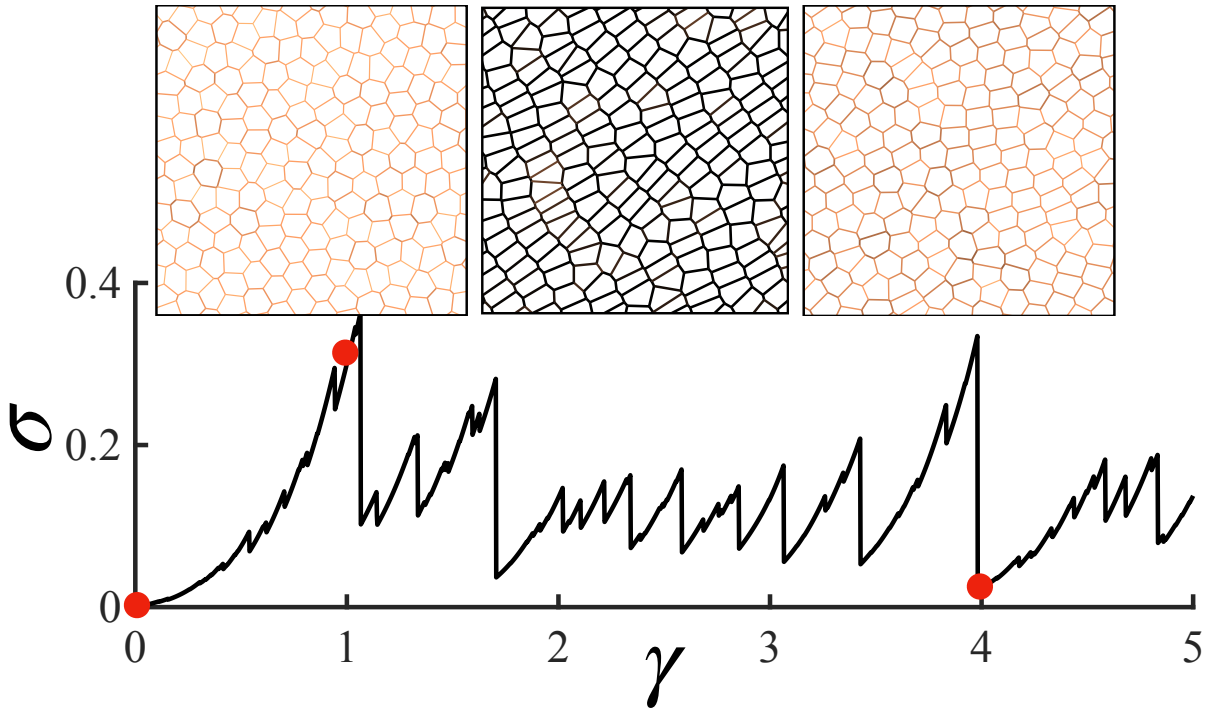


Figure 2.2: Representative tissue stress trace and tension network snapshots with  $p_0 = 3.75$  as an example of  $p_0 < 3.81$ . The strains of snapshots are  $\gamma = 0, 1, 4$ , respectively, which are marked by red dots on the trace. The snapshot edges are color-coded according to the edge tension defined by Eq. (2.3).

To investigate the mechanical response of these tissues, we calculate the tension  $\mathbf{T}_{ij}$  along an edge  $\mathbf{l}_{ij}$  shared by cells  $i$  and  $j$  from the geometry of cells using the equation

$$\mathbf{T}_{ij} = \frac{\partial E}{\partial \mathbf{l}_{ij}} = 2[(p_i - p_0) + (p_j - p_0)] \hat{\mathbf{l}}_{ij}; \quad (2.3)$$

**COMMENT:** typo above in the unit vector. JH: it is a unit vector along edge  $l_{ij}$ .

and the global tissue shear stress,  $\sigma$ , follows as [46]

$$\sigma = \frac{1}{N} \sum_{i < j} T_{ij}^x l_{ij}^y, \quad (2.4)$$

where  $T_{ij}^x$  and  $l_{ij}^y$  are the  $x$ -component of  $\mathbf{T}_{ij}$  and  $y$ -component of  $\mathbf{l}_{ij}$ , respectively. It is known that for  $p_0 < p_0^* = 3.81 \pm 0.01$  geometric incompatibility leads to rigidity of unsheared tissues, characterized by positive shear modulus and bulk modulus calculated by the finite linear-response theory [29]. When  $p_0 > p_0^*$ , both the shear modulus and bulk modulus vanish, signaling a floppy state of tissue [47].

These predictions are confirmed by our shear simulation results at  $\Gamma \approx 0$ . As an example of  $p_0 < p_0^*$  tissues, Fig. 2.2 shows the stress-strain trace of a tissue with  $p_0 = 3.75$ . The stress is zero at the initial strain-free state and immediately starts to increase once a strain is applied, resulting from a positive shear modulus at the strain-free state, as previously reported. The system exhibits global intermittent dynamics featured by slow buildups and rapid release of stress. During the shearing process, the stress accumulates as tension networks appear and grow across the tissue until  $T_1$  rearrangements are triggered and stress rapidly drops to a lower value. In our simulations with  $p_0 < 3.81$ , stress never returns to zero once the tissue is sheared, which suggests that originally solid-like tissues always stay rigid with a finite shear modulus, and it cannot spontaneously return to an unstrained state at zero temperature. The increasing elastic modulus indicates that for tissues that are originally solid-like, the stress-stiffening response increases the shear modulus.

An obvious observation is that the stress accumulations between two successive rapid drops are not straight lines in these two representative stress traces. Actually, during strain steps without  $T_1$  rearrangements, it is generally true that given a fixed  $p_0$  parameter, stress increases faster in a high-stress regime than in a low-stress regime, which is different from an elastic solid whose

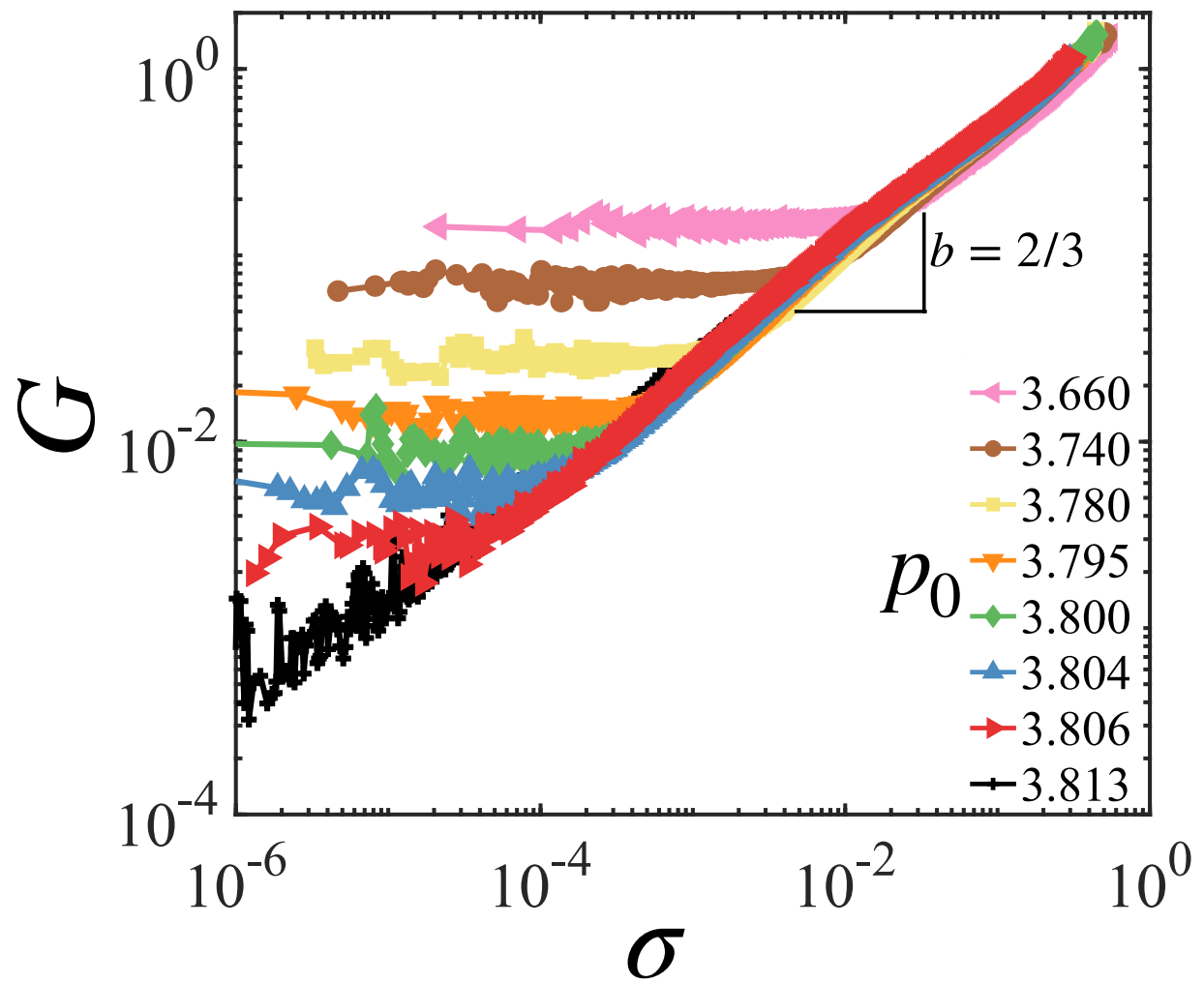


Figure 2.3: The shear modulus  $G$  vs. stress  $\sigma$  at various  $p_0 < p_0^*$  and  $\kappa_A = 0$ .

stress is proportional to the strain. To quantify the nonlinearity and extract a constitutive equation for the tissue, we use  $\sigma$ , instead of  $\gamma$ , as a state variable and plot  $G$  as a function of  $\sigma$  in Fig.2.3 for various  $p_0 \in [3.66, 3.81]$ . At small  $\sigma$ , the shear modulus roughly stays at a plateau of  $G = G_0$  that is independent of  $\sigma$ , corresponding to linear elasticity. At higher stress, the elastic response is nonlinear and  $G \propto \sigma^b$ , with  $b = 2/3$ . Using  $G = \partial\sigma/\partial\gamma$  and eliminating  $G$ , this yields a constitutive relation  $\sigma \propto \gamma^{\frac{1}{1-b}} = \gamma^3$ . As the  $G$  versus  $\sigma$  curves of different  $p_0$  tissues all follow this simple pattern, we can propose a scaling formula to unify them

$$G/G_0 = \mathcal{G} \left( \frac{\sigma}{\sigma_c} \right), \quad (2.5)$$

where  $\mathcal{G}$  is a universal function that is independent of  $p_0$ . We plot all data in Fig.2.4, along with the  $G_0$  and  $\sigma_c$  values as functions of  $p_0$ . The linear and nonlinear regimes are separated by a critical stress threshold  $\sigma_c$ , i.e. the data collapse to a universal curve that is composed of a low shear modulus plateau at  $\sigma < \sigma_c$  and a power-law increase with an exponent of  $b = 2/3$ . At the same time, the critical stress also shows power-law scaling as  $\sigma_c(p_0) \sim |p_0 - p_0^*|$ , and the linear-response modulus  $G_0$  follows  $|p_0 - p_0^*|$  [29, 43]. Thus, the Eq. (2.5) can be summarized through a scaling ansatz to describe the behavior of  $G$  in the vicinity of the critical point  $p_0^*$

$$G = |p_0 - p_0^*|^\phi \mathcal{G} \left( \frac{\sigma}{|p_0 - p_0^*|^\Delta} \right). \quad (2.6)$$

This form provides an excellent collapse of all our data onto a single master curve independent of  $p_0$  as shown in Fig.2.4. From the scaling collapse, we obtain  $G_0 \propto |p_0 - p_0^*|^\phi$  and  $\sigma_c \propto |p_0 - p_0^*|^\Delta$ , where  $\Delta = 3/2$  and  $\phi = 1$ . Crucially, the stress-stiffening scaling collapse (Eq.(2.6)) is directly related to the cell shape-stress scaling relation (Eq.(2.19)) as  $b = \phi/\Delta$ .

Such a nonlinear shear response is beyond the scope of previous studies that use linear response assumption, and it is highly relevant under physiological conditions. Since epithelial tissues that

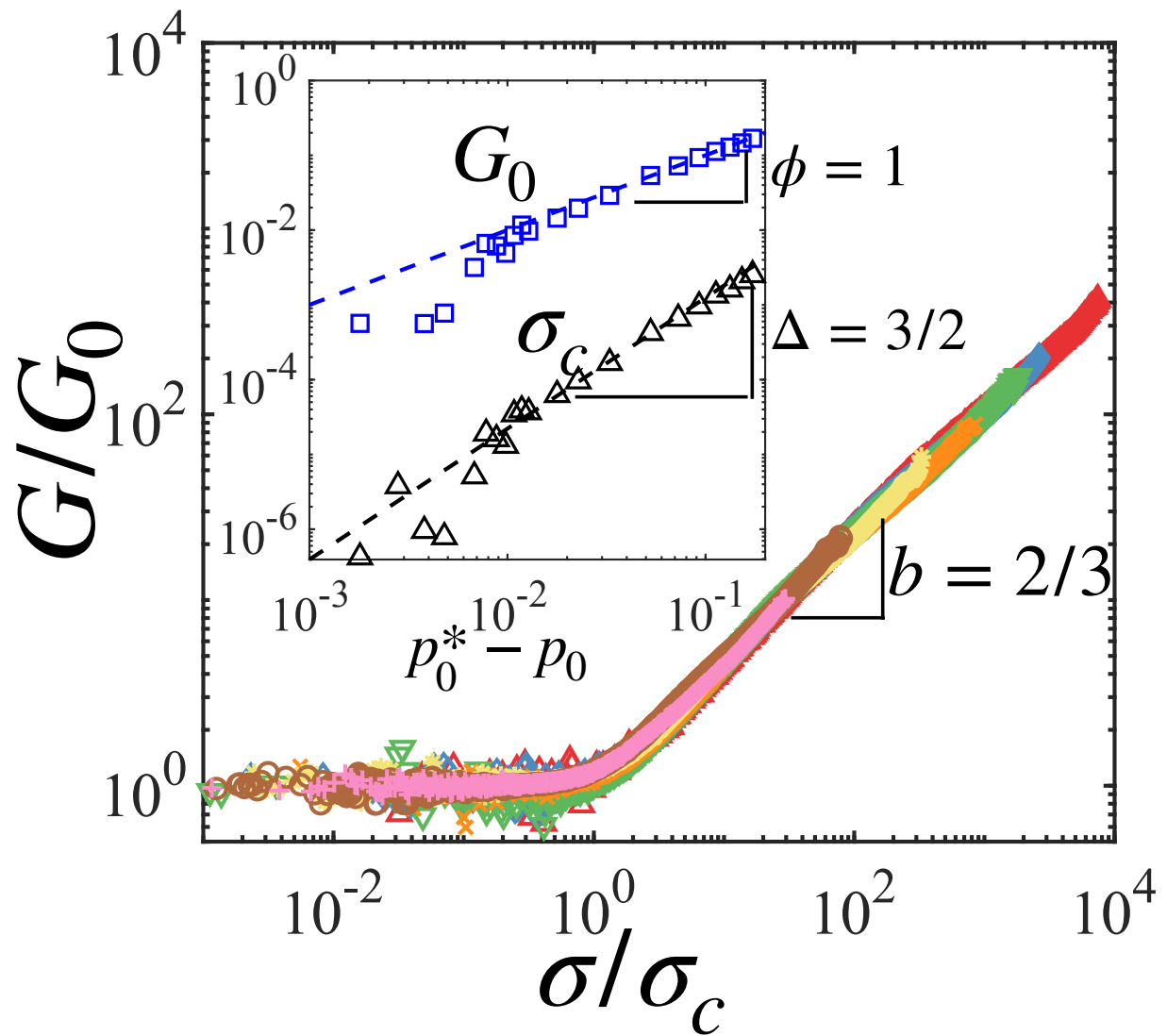


Figure 2.4: Rescaled  $G/G_0$  vs  $\sigma/\sigma_c$  for the same set of  $p_0$  values as in Fig. 2.3.

form barriers and filters in organs often experience various strains and stresses in the body, their nonlinear response to such conditions can significantly influence their mechanical stability and functionality, and the nonlinear shear response characterizes how these tissues maintain rigidity and resist deformation under such conditions.

## 2.3 Strain-driven Solidification

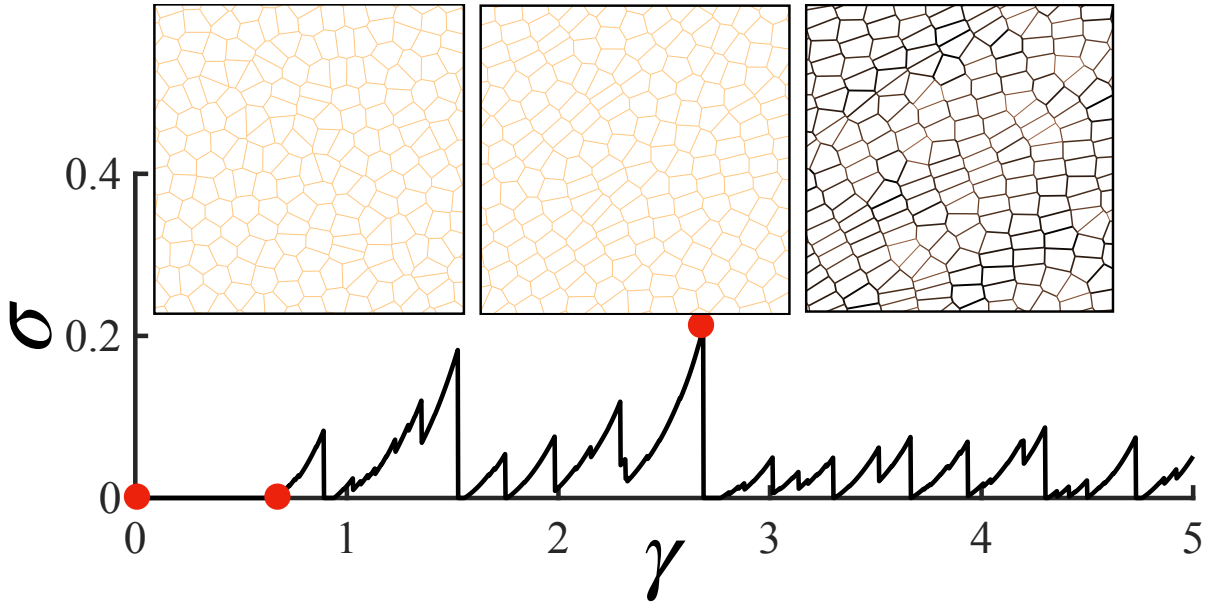


Figure 2.5: Representative tissue stress trace and tension network snapshots with  $p_0 = 3.89$  as an example of  $p_0 > 3.81$ . The strain values of the sample snapshots are  $\gamma = 0, 0.65, 2.66$ , respectively, which are marked by red dots on the trace. The snapshot edges are color-coded according to the edge tension defined by Eq. (2.3).

In addition to the stress-stiffening phenomenon discussed above, there is another nonlinear shear response in the system. Fig. 2.5 shows the stress response and snapshots of tissue with  $p_0 = 3.89$ , as an example of  $p_0 > p_0^*$ . In accordance with linear response predictions, it is observed that at  $\gamma = 0$ , the stress remains invariant in response to strain, thereby indicating that the shear modulus has a zero magnitude. This characteristic behavior is a hallmark of a fluid state. Intriguingly,  $\sigma$  remains flat at zero at the small strain stage until a critical strain  $\gamma_C$ , which is marked as the second red dot in the plot. This means that for tissues that are fluid-like at the beginning, strain-stiffening

transits them to a positive shear modulus. In addition, after being solidified the stress also exhibits a mixture of accumulations and rapid drops like originally solid-like tissues, and even at large strain, tissues can return to and stay in a zero-stress state for a range of strain steps. In other words, tissues that are originally fluid-like can be solidified by a critical strain  $\gamma_C$ , and they can reenter and exit a fluid-like state in the following shearing process.

In tissues strained beyond  $\gamma_C$  both the stress  $\sigma$  and the shear modulus  $G$  are nonlinear functions of the applied strain  $\gamma$ . One would immediately ask what has happened during the shear-induced rigidity transition at  $\gamma_C$ . First, as illustrated in Fig.2.6(a), where the shear modulus  $G$  is plotted as a function of the strain difference  $\gamma - \gamma_C$ , the strain-induced rigidity transition in biological tissues is significantly influenced by the parameter of area stiffness  $\kappa_A$ . When  $\kappa_A$  is set to zero, the onset of rigidity in the tissue exhibits a discontinuous nature characterized by a steep jump at the critical strain  $\gamma_C$ , which remains finite even when  $\kappa_A$  is slightly above zero. As  $\kappa_A$  increases, this jump discontinuity decreases monotonically. Especially when  $\kappa_A \geq 10^{-3}$ , the jump discontinuity becomes negligibly small that the increase in  $G$  appears continuous, making it challenging to distinguish from a gradual increase in rigidity. This trend is evident in the inset of Fig.2.6(a), where we plot the  $G$  values at  $\gamma = \gamma_C \pm \Delta\gamma$ , i.e. right below and above the critical strain. Below the critical strain ( $\gamma \rightarrow \gamma_C^-$ ), the tissue behaves as a marginally rigid solid, and  $G$  increases linearly with  $\kappa_A$  in this regime [56, 47]. On the other hand, above the critical strain ( $\gamma \rightarrow \gamma_C^+$ ),  $G$  is not sensitive to  $\kappa_A$  value and stays at a stable plateau. The difference in the rigidity  $G$  at the rigidity transition thus exhibits a decrease as  $\kappa_A$  increases. This serves as a macro-scale description of what happens in the shear-induced rigidity transition.

In addition, to capture how the microscale deformations in disordered systems deviate from idealized and uniform predictions, researchers define the non-affinity parameter  $\delta\Gamma$  [57, 58, 59]

$$\delta\Gamma = \frac{1}{N\bar{A}\Delta\gamma^2} \langle \left( \delta\mathbf{r}_i - \delta\mathbf{r}_i^{\text{affine}} \right)^2 \rangle, \quad (2.7)$$

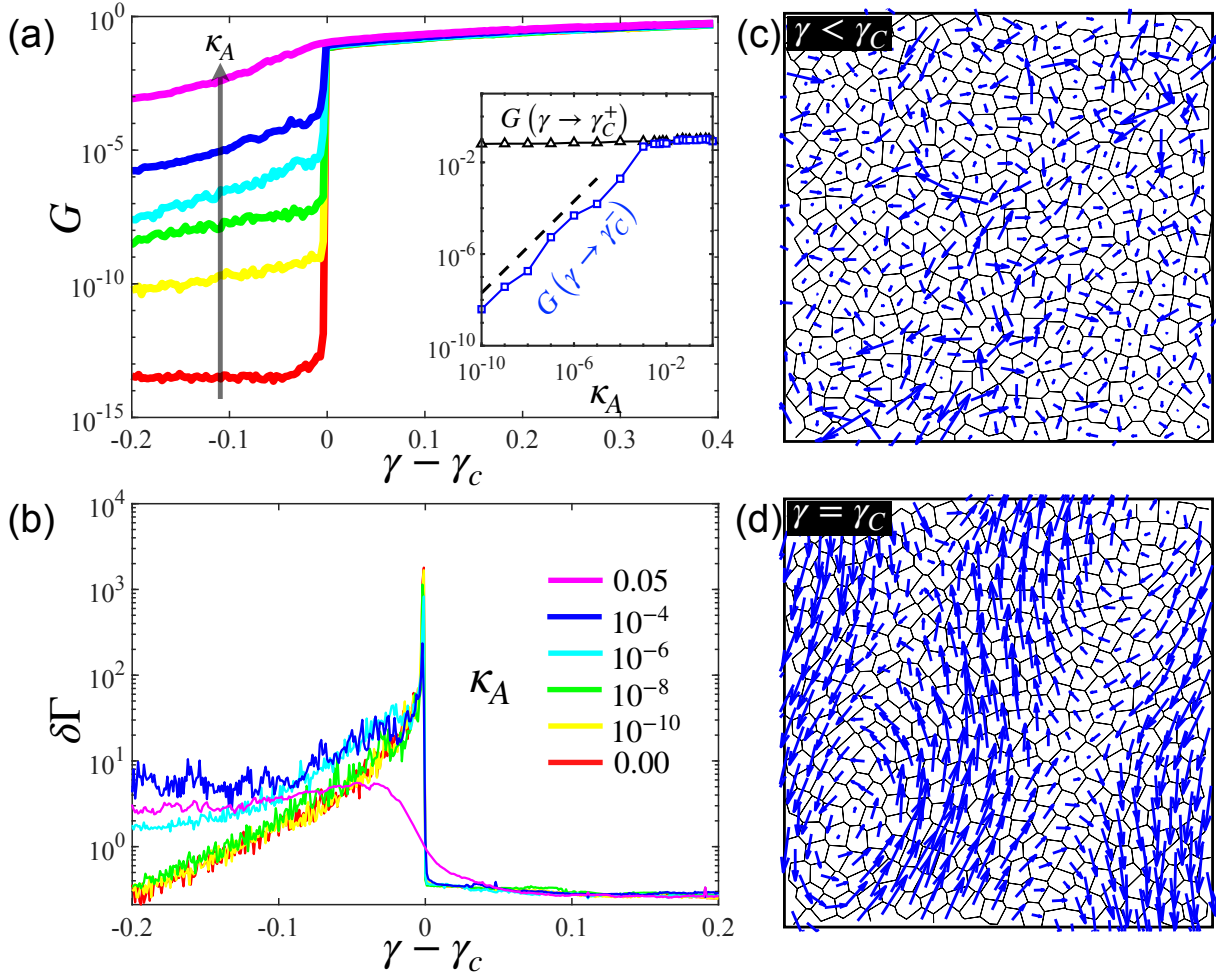


Figure 2.6: **Strain-driven rigidity transition.** (a) The shear modulus  $G$  near the onset of the strain-driven solidification for  $p_0 = 3.84$  and varying values of area elasticity  $\kappa_A = 0, 10^{-10}, 10^{-8}, 10^{-6}, 10^{-4}, 0.05$ . Here, the colors correspond to the legend in panel (b). **Inset:** The value of  $G$  immediately below and above the transition show a gap that narrows with increasing  $\kappa_A$ . The dashed line indicates a slope of 1 on the log-log plot. The transition is discontinuous in  $G$  at  $\gamma = \gamma_C$  (b) The Non-affinity parameter  $\Delta\Gamma$  near the onset of the transition for  $p_0 = 3.84$  and varying values of area elasticity  $\kappa_A$ . Maps of non-affine cell displacements before (c) and at (d) the onset of strain stiffening for  $\kappa_A=0$ .

where  $\delta\mathbf{r}_i$  is the displacement of cell  $i$  after a strain step and  $\delta\mathbf{r}_i^{\text{affine}} = \Delta\gamma y_i \hat{x}$  is the affine deformation of the cell located at  $\mathbf{r}_i = (x_i, y_i)$ . In Fig.2.6(b), we show the non-affinity parameter around  $\gamma = \gamma_C$  to quantify the behavior of the fluctuations near the strain-driven rigidity transition. At low area elasticity ( $\kappa_A \lesssim 10^{-3}$ ),  $\delta\Gamma$  increases monotonically with strain and exhibits a sharp peak at the critical strain  $\gamma_C$ . This peak aligns with the rigidity transition, marking a significant change in the tissue's mechanical properties. In contrast, at higher  $\kappa_A$ , the peak in  $\delta\Gamma$  is not pronounced. This indicates a more gradual and smooth crossover from the state of a marginal solid to a fully rigid solid, as opposed to a sharp, discontinuous transition. This smooth crossover is indicative of more complex mechanical behavior in tissues with higher area stiffness, highlighting the nuanced interplay between microscopic cellular displacements and macroscopic mechanical properties. Fig.2.6(c) is a representative snapshot of  $\gamma < \gamma_C$ , which shows that as the tissue is a marginally rigid solid, the non-affine cell displacements are local and of different magnitudes, corresponding to the plateau region of  $\gamma - \gamma_C < 0$  in panel (b). Lastly, panel (d) shows the non-affine cell displacements at the onset of strain stiffening, where the non-affine cell displacements are global and long-range correlated, contributing to the sharp peak in panel (b). After the tissues are stiffened, the non-affine cell displacements are minimal, which is typical for a regular solid, corresponding to the lower plateau in panel (b).

## 2.4 Correlating Mechanical Response and Cell Shapes

The strain stiffening behavior above  $\gamma_C(p_0)$  can be understood in terms of shear-induced changes in the structural properties of the cellular network. Past work on vertex models has shown that the observed cell shape index, given by  $q \equiv \langle p/\sqrt{a} \rangle$ , is an important metric of the rheological state of the tissue [45, 37]. Motivated by this, we have examined the evolution of this order parameter with applied shear. For materials with fixed topology, such as fiber networks, the applied strain  $\gamma$  indicates the material deformation level. However, in our model, cell rearrangements will release the accumulated strain and induce a mismatch between  $\gamma$  and tissue deformation. The applied strain

$\gamma$  is history-dependent and does not uniquely define the state of the tissue due to plastic events and non-affine deformations. In other words, due to the avalanche events, the actual strain carried by a tissue at  $\gamma = 6$  is not necessarily larger than another tissue at  $\gamma = 3$ .

This mismatch inspires us to find a better indicator to capture the carried strain in tissues. For this goal, here we define a new order parameter called the true strain  $\gamma_{\text{true}}$  [60], which is calculated based on the cell geometry directly, to quantify the degree of deformation of the tissue. For a given tissue snapshot, first, we characterize the tissue shape tensor  $\Psi$  as

$$\Psi = \langle \Psi_i \rangle = \frac{1}{N} \sum_{i=1}^N \Psi_i, \quad (2.8)$$

where  $\Psi_i$  is the monocellular shape tensors of the  $i$ -th cell, whose components are defined as

$$\Psi_{i,\alpha\beta} = \frac{1}{A_i} \int \alpha \beta dA_i. \quad (2.9)$$

Here,  $\alpha$  and  $\beta$  represent  $x$  or  $y$ , while the origin is set to the cell's geometric centroid.  $A_i$  is the area of the  $i$ -th cell. The tensor  $\Psi_i$  has three independent components because  $\Psi_{i,xy} = \Psi_{i,yx}$  by definition, making  $\Psi$  to be symmetric.

For an unsheared tissue containing a sufficiently large number of cells, due to the isotropic symmetry such a tissue possesses, we know immediately that  $\Psi_{xx} = \Psi_{yy}$  and  $\Psi_{xy} = \Psi_{yx} = 0$ . However, deformations applied to these tissues could break the isotropic symmetry in some way. For example, simple shear deformations specific a shear flow along  $x$ -axis so that the symmetry between  $x$ -direction and  $y$ -direction is no longer conserved. This simple example gives us some hints that the tissue shape tensor  $\Psi$  can be used to induce statistical information about the deformation a tissue carries. For this goal, given an instantaneous snapshot of a tissue, we assume that the cells

are under an overall deformation field described by a deformation tensor  $\mathbf{D}$  such that

$$\mathbf{D} \vec{r}^{(0)} = \begin{bmatrix} D_{xx} & D_{xy} \\ D_{yx} & D_{yy} \end{bmatrix} \begin{bmatrix} x^{(0)} \\ y^{(0)} \end{bmatrix} = \begin{bmatrix} x \\ y \end{bmatrix} = \vec{r}, \quad (2.10)$$

where  $\vec{r}$  is the new position column vector of  $\vec{r}$  after deformation. Both the average shape tensor  $\Psi$  and monocellular shape tensor  $\Psi_i$  follow the relation

$$\begin{cases} \Psi_{xx} = D_{xx}^2 \Psi_{xx}^{(0)} + 2D_{xx}D_{xy}\Psi_{xy}^{(0)} + D_{xy}^2 \Psi_{yy}^{(0)} \\ \Psi_{xy} = D_{xx}D_{yx}\Psi_{xx}^{(0)} + (D_{xx}D_{yy} + D_{xy}D_{yx})\Psi_{xy}^{(0)} + D_{xy}D_{yy}\Psi_{yy}^{(0)} \\ \Psi_{yy} = D_{yx}^2 \Psi_{xx}^{(0)} + 2D_{yx}D_{yy}\Psi_{xy}^{(0)} + D_{yy}^2 \Psi_{yy}^{(0)}. \end{cases} \quad (2.11)$$

The above relation can be proved by noticing that after deformation  $\mathbf{D}$ ,  $x = D_{xx}x^{(0)} + D_{xy}y^{(0)}$ , and area  $A^{(0)}$  is stretched to  $|\mathbf{D}|A^{(0)}$ , where  $|\mathbf{D}|$  denotes the determinant of  $\mathbf{D}$ . Then the new  $\Psi_{xx}$ , as an example, can be written as

$$\begin{aligned} \Psi_{xx} &= \frac{1}{A} \int x^2 dA = \frac{1}{|\mathbf{D}|A^{(0)}} \int [D_{xx}x^{(0)} + D_{xy}y^{(0)}]^2 d(|\mathbf{D}|A^{(0)}) \\ &= \frac{1}{A^{(0)}} [D_{xx}^2 \int x^{(0)2} dA^{(0)} + 2D_{xx}D_{xy} \int x^{(0)}y^{(0)} dA^{(0)} + D_{xy}^2 \int y^{(0)2} dA^{(0)}] \\ &= D_{xx}^2 \Psi_{xx}^{(0)} + 2D_{xx}D_{xy}\Psi_{xy}^{(0)} + D_{xy}^2 \Psi_{yy}^{(0)} \end{aligned} \quad (2.12)$$

Now, since every cell in the tissue is under the same  $\mathbf{D}$ , the conservation of the average cell area requires  $|\mathbf{D}| = 1$ . In addition, Eqs. (2.11) gives  $|\Psi| = |\mathbf{D}|^2 |\Psi^{(0)}|$ , as a consequence  $|\Psi| = |\Psi^{(0)}|$ . When the tissue is strain-free, we expect the average cell shape to be isotropic, i.e., the undeformed shape tensor is a multiple of the 2D identity matrix, in which  $\Psi_{xx}^{(0)} = \Psi_{yy}^{(0)} = \sqrt{|\Psi|}$

and  $\Psi_{xy}^{(0)} = \Psi_{yx}^{(0)} = 0$ . Then the above equation can be simplified to

$$\begin{cases} \frac{\Psi_{xx}}{\sqrt{|\Psi|}} = D_{xx}^2 + D_{xy}^2 \\ \frac{\Psi_{xy}}{\sqrt{|\Psi|}} = D_{xx}D_{yx} + D_{xy}D_{yy} \\ \frac{\Psi_{yy}}{\sqrt{|\Psi|}} = D_{yx}^2 + D_{yy}^2 \end{cases} \quad (2.13)$$

The deformation tensor is under-constraint. Without losing generality, we set the deformation matrix to be symmetric, i.e.  $D_{xy} = D_{yx}$ . Solving the equations leads to

$$\begin{cases} D_{xx} = \frac{\Psi_{xx} + \sqrt{|\Psi|}}{|\Psi|^{\frac{1}{4}} \sqrt{\Psi_{xx} + \Psi_{yy} + 2\sqrt{|\Psi|}}} \\ D_{xy} = \frac{\Psi_{xy}}{|\Psi|^{\frac{1}{4}} \sqrt{\Psi_{xx} + \Psi_{yy} + 2\sqrt{|\Psi|}}} \\ D_{yy} = \frac{\Psi_{yy} + \sqrt{|\Psi|}}{|\Psi|^{\frac{1}{4}} \sqrt{\Psi_{xx} + \Psi_{yy} + 2\sqrt{|\Psi|}}} \end{cases} \quad (2.14)$$

The resulting symmetric  $\mathbf{D}$  has orthogonal eigenvectors, with eigenvalues  $\lambda_{\pm}$  whose product is 1:

$$\lambda_{\pm} = \frac{1}{2} \left[ (D_{xx} + D_{yy}) \pm \sqrt{(D_{xx} - D_{yy})^2 + 4D_{xy}^2} \right] \quad (2.15)$$

$$= \frac{1}{2|\Psi|^{\frac{1}{4}}} \left[ \sqrt{\Psi_{xx} + \Psi_{yy} + 2\sqrt{|\Psi|}} \pm \sqrt{\Psi_{xx} + \Psi_{yy} - 2\sqrt{|\Psi|}} \right]. \quad (2.16)$$

This means the overall deformation field can be seen as an affine pure shearing. The overall aligned cell elongation level is indicated by this pure shear. Thus, it is natural to define the overall effective strain to be the pure shear magnitude  $\gamma_{\text{true}} = \frac{\log(\lambda_+) - \log(\lambda_-)}{2}$ , or equivalently  $\gamma_{\text{true}} = \log(\lambda_+)$  as

$\lambda_+ \lambda_- = 1$ , which leads to

$$\gamma_{\text{true}} = \log \left\{ \frac{\sqrt{\Psi_{xx} + \Psi_{yy} + 2\sqrt{|\Psi|}} + \sqrt{\Psi_{xx} + \Psi_{yy} - 2\sqrt{|\Psi|}}}{2|\Psi|^{\frac{1}{4}}} \right\}. \quad (2.17)$$

This  $\gamma_{\text{true}}$  indicates that the tissue state can be reached from an isotropic state by applying a certain pure shear of magnitude  $\gamma_{\text{true}}$ , which indicates how much overall cell elongation in the same direction is accumulated at the state. In other words, by applying a pure shear of magnitude  $-\gamma_{\text{true}}$ , the tissue can be reversed to isotropic. It should be mentioned that this effective strain calculation solely depends on the current state, which makes it different from other previous methods that involve historical tracking. This method is designed to work in biological tissues where cells can experience rapid large-scale rearrangements, which makes the deformation tensor not smooth in time. However, it is not suitable for systems in which the local deformation changes dramatically from cell to cell, i.e. not spatially smooth.

As  $\gamma_{\text{true}}$  is calculated from the instantaneous deformation tensor of the whole tissue and therefore captures the degree of *cumulative* strain deformation. The motivation for introducing  $\gamma_{\text{true}}$  is similar to that behind the fabric tensor in granular materials [61] or the recoverable strain in rheology [62]. In Fig.2.7(a, b) we show the stress  $\sigma$  and the structural order parameter  $q$  as functions of  $\gamma_{\text{true}}$ . It is evident from Fig.2.7(b) that under shear cell shapes in the fluid stay constant at the *energetically preferred value*  $p_0$  until the fluid strain-stiffens, while in the solid  $q$  always starts out at the universal value  $p_0^*$  and grows quadratically with  $\gamma_{\text{true}}$ . This behavior is well described by

$$q = \begin{cases} p_0, & \gamma_{\text{true}} \leq \gamma_C(p_0); \\ p_0^* + c \gamma_{\text{true}}^2, & \gamma_{\text{true}} > \gamma_C(p_0). \end{cases} \quad (2.18)$$

Recent research on the development of Drosophila has reported a similar functional dependence of cell morphology on the elongation driven by active stresses generated internally [23]. In this study,

the authors effectively demonstrated that temporal alterations in cell shape and orientation within the Drosophila germband are predictive of the commencement of swift cellular rearrangements. This phenomenon is particularly pronounced in both wild-type and snail-twist mutant embryos. The findings of the study imply that the process of convergent extension is linked with a transition towards more fluid-like characteristics of the tissue. Such a transition is hypothesized to facilitate alterations in tissue morphology during rapid developmental phases.

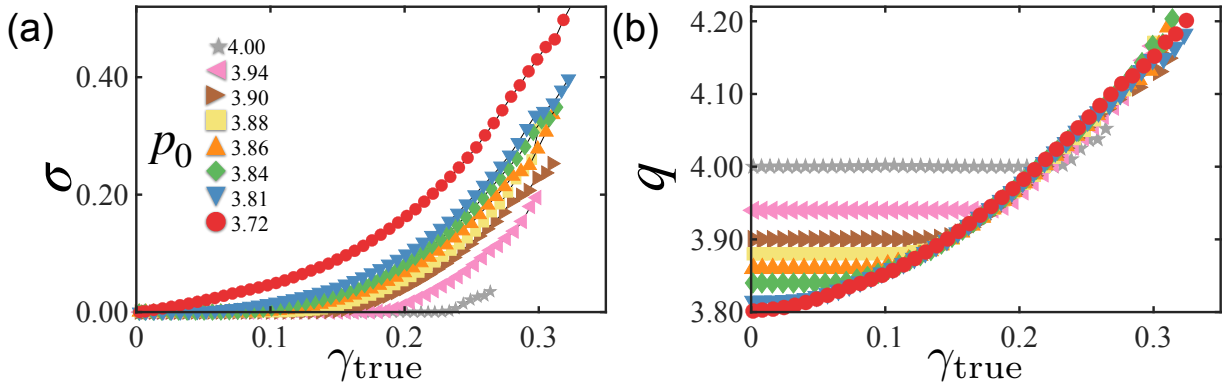


**Figure 2.7: Tissue stress and cell shapes under shear.** (a) A plot of  $\sigma$  as a function of  $\gamma_{\text{true}}$  for different  $p_0$ 's spanning the solid and liquid regimes at  $\kappa_A = 0$ . (b) The cell shape index  $q$  vs the true strain  $\gamma_{\text{true}}$  for the same range of  $p_0$  as in (a).

Eq. (2.18) indicates that we can use  $\delta q \equiv q - p_0^*$  as a morphological order parameter to capture the deviation of a cell's observed shape from its critical cell shape. Fig. 2.7(a, b) further reveals an interdependent relationship among the state variables  $\sigma$ ,  $\gamma_{\text{true}}$ , and  $\delta q$ . This interdependence suggests that a comprehensive description of the tissue state can be effectively achieved by considering only two of these variables. As an example, we use  $\delta q$  and  $\sigma$  in Fig. 2.8(a), where  $\delta q$  is plotted as a function of  $\sigma$  across a broad range of  $p_0 \in [3.72, 4]$ . The plot exhibits the typical hallmark of a critical point, with distinct behavioral patterns in two branches above and below the threshold value  $p_0^*$ . This suggests a scaling hypothesis expressed as:

$$\delta q = |p_0 - p_0^*|^\phi Q_\pm \left( \frac{\sigma}{|p_0 - p_0^*|^\Delta} \right), \quad (2.19)$$

where  $Q_{\pm}(x)$  represent the branches of a universal scaling function. These branches are applicable for conditions  $p_0 > p_0^*$  and  $p_0 \leq p_0^*$ , respectively, with  $x$  defined as  $\sigma/|p_0 - p_0^*|^{\Delta}$ .

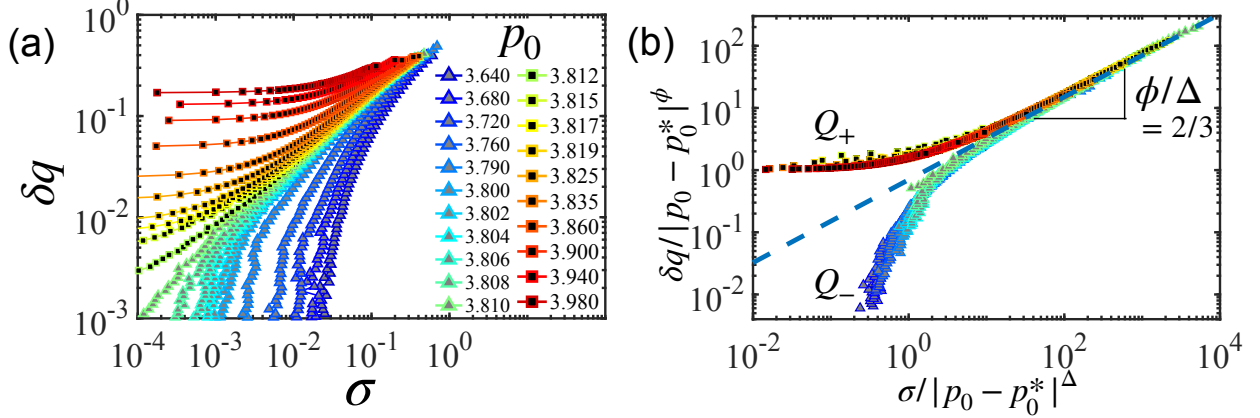


Figure 2.8: **Correlating cell shapes and tissue stress.** (a) A plot of  $\delta q \equiv q - p_0^*$  vs.  $\sigma$  for various values of  $p_0$  as indicated with  $\kappa_A = 0$ . (b) Replotting of the data from (a) using the universal scaling ansatz (as defined in Eq.(2.19)). Here  $\Delta = 3/2$  and  $\phi = 1$ .

The efficacy of this scaling hypothesis is demonstrated in Figure 2.8(b), which shows a near-perfect data collapse under this scaling, with the values of  $\Delta = 3/2$  and  $\phi = 1$  being identified. In the regime where  $p_0 > p_0^*$ , the behavior is predominantly dictated by  $Q_+(x)$ . As  $x$  approaches zero (or equivalently, as  $\sigma \rightarrow 0$ ),  $Q_+(x)$  tends towards a constant value. This implies that in this regime,  $\delta q$  is directly proportional to  $|p_0 - p_0^*|^\phi$ . Conversely, when  $p_0 < p_0^*$ , the scaling behavior is controlled by  $Q_-(x)$ . In this context, as  $\delta q$  approaches zero (or, in other terms, as  $y = \delta q/|p_0 - p_0^*|^\phi \rightarrow 0$ ), the inverse function of  $Q_-$  asymptotically approaches a constant value. This trend indicates that in this regime,  $\sigma$  is proportional to  $|p_0 - p_0^*|^\Delta$ . Furthermore, in the limiting case where  $|p_0 - p_0^*| \rightarrow 0$  and  $\sigma \gg 0$ , the two branches of the universal scaling function,  $Q_+(x)$  and  $Q_-(x)$ , converge. This convergence leads to the relationship  $Q_+(x) = Q_-(x) = x^{\phi/\Delta}$ , signifying a unified scaling behavior in this specific limit.

## 2.5 Mean-Field Model of Sheared Tissues

Fig. 2.9 summarizes the mechanical behaviors and phase diagram of a sheared tissue. Fig. 2.9(a) shows the configuration-averaged stress  $\langle \sigma \rangle$  as a function of  $\gamma$ . Generally, the higher the  $p_0$  value, the lower  $\langle \sigma \rangle$  at a given strain. At the initial stage, for  $p_0 < 3.81$ ,  $\langle \sigma \rangle$  starts to increase once a strain is applied; For  $p_0 > 3.81$ ,  $\langle \sigma \rangle$  remains zero until a critical strain  $\gamma_C$ , and this transition to positive stress happens later when  $p_0$  rises further. After  $\gamma_C$ , the stress goes up and reaches a statistical maximum around  $\gamma = 0.8 \sim 1.5$ . After  $\gamma = 2$ , the  $\langle \sigma \rangle$  values of most  $p_0$  tissues reach and fluctuate around a plateau.

$\gamma_C$  is the strain required for tissues to have a positive shear stress. Fig. 2.9(b) shows  $\gamma_C$  is zero for  $p_0 < 3.81$ , and becomes positive for  $p_0 > p_0^*$ . Some samples with  $p_0 > 3.95$  have never been solidified until the end of the simulation. For these samples, their  $\gamma_C$  values are set to the maximum strain,  $\gamma_f = 5$ , which inevitably underrates the actual  $\gamma_C$ .

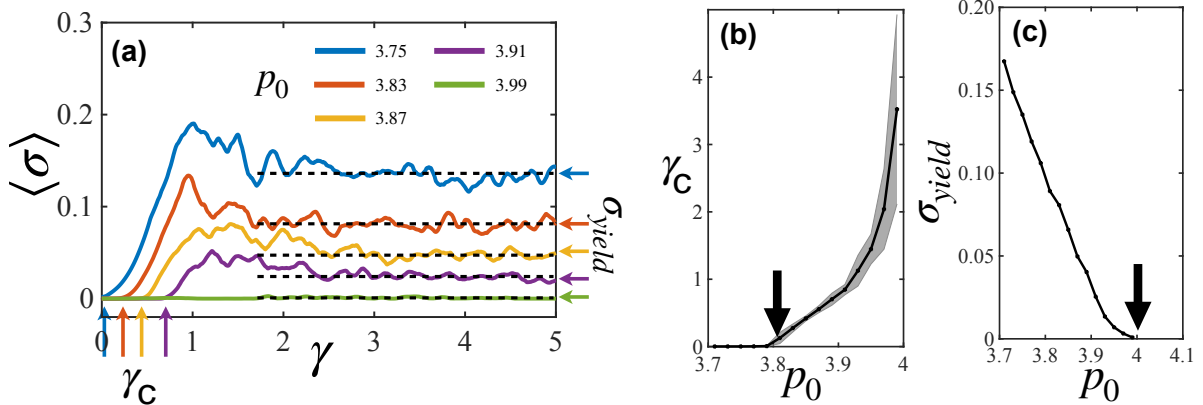


Figure 2.9: **The mechanical response of epithelial tissue to applied shear strain as a function of  $p_0$  with  $\kappa_A = 0$ .** (a) The average stress  $\langle \sigma \rangle$  as a function of strain for tissues. The vertical arrows indicate the corresponding critical strain  $\gamma_C$ , where  $\langle \sigma \rangle$  starts to become positive. The horizontal dashed lines are the yield stress  $\sigma_{yield}$  of tissues, which is the average of steady-state stress. (b) The critical strain  $\gamma_C$  as function of  $p_0$ . The solid black curve is the median over 28 samples, and the gray shadow shows the standard deviation. The arrow indicates the transition point at  $p_0^* = 3.81$ . (c) The yield stress  $\sigma_{yield}$  as function of  $p_0$  averaged over 28 samples at  $\gamma$  ranging from 1 to 5.

As shown in Fig. 2.9(c), for  $p_0 < p_0^*$ , the unstrained tissue is in a solid state, and the tissue exhibits stiffening for any finite value of  $\gamma$ , which consequently implies that  $\gamma_C(p_0) = 0$ . When the unstrained tissue is in a fluid state, i.e.  $p_0 > p_0^*$ , applying a shear strain  $\gamma$  results in a finite stress response once  $\gamma$  reaches or exceeds the critical value  $\gamma_C$ . The critical line  $\gamma_C(p_0)$  in Fig.2.9(d) delineates the boundary of a strain-induced rigidity transition, where the instantaneous shear modulus  $G \equiv \partial\sigma/\partial\gamma$  transits from zero to a finite value. For  $p_0$  values within the range  $[p_0^*, 4.03]$ , a nonzero strain is always required to induce rigidity, and  $\gamma_C(p_0)$  increases monotonically with  $p_0$ . Beyond the threshold of  $p_0 \gtrsim 4.03$ , the tissue retains its fluid-like characteristics regardless of the applied shear strain. This observation aligns with the disappearance of the yield stress  $\sigma_{yield}$  for  $p_0 > 4.03$ . This kind of shear stiffening phenomenon in the liquid phase has also been reported in recent studies focusing on a regular (crystalline) vertex model [63] and in spring-network models [47].

To gain a theoretical understanding of the emergence of nonlinear elasticity and strain-driven rigidity, we derive a mean-field theory (MFT) formulation of the vertex model. Neglecting cell-cell correlations, we consider the shear deformation of a single  $n$ -sided polygonal cell. Under affine deformations, the vertex coordinates of a polygon transform according to  $\mathbf{R}' = \hat{D}\mathbf{R}$ , where  $\hat{D}$  is the deformation tensor given by  $\hat{D} = \begin{pmatrix} D_{xx} & D_{xy} \\ D_{yx} & D_{yy} \end{pmatrix}$ . We neglect in Eq.(2.2) the contribution from a cell's area, which is typically small compared to the perimeter term and examine area-preserving affine deformations with  $\det \hat{D} = 1$ . For simple shear  $D_{yx} = 0$  and  $D_{yy} = 1/D_{xx}$ , leaving only  $D_{xx}$  and  $D_{xy}$  as independent components of  $\hat{D}$ .

The perimeter of a deformed polygon can then be expressed in terms of the components of  $\hat{D}$ .

For example, the perimeter of a quadrilateral ( $n = 4$ ) is given by

$$\begin{aligned}
P = & \sqrt{\left| \frac{y_1 - y_2}{D_{xx}} \right|^2 + |D_{xx}x_1 - D_{xx}x_2 + D_{xy}y_1 - D_{xy}y_2|^2} \\
& + \sqrt{\left| \frac{y_2 - y_3}{D_{xx}} \right|^2 + |D_{xx}x_2 - D_{xx}x_3 + D_{xy}y_2 - D_{xy}y_3|^2} \\
& + \sqrt{\left| \frac{y_3 - y_4}{D_{xx}} \right|^2 + |D_{xx}x_3 - D_{xx}x_4 + D_{xy}y_3 - D_{xy}y_4|^2} \\
& + \sqrt{\left| \frac{y_4 - y_1}{D_{xx}} \right|^2 + |D_{xx}x_4 - D_{xx}x_1 + D_{xy}y_4 - D_{xy}y_1|^2},
\end{aligned} \tag{2.20}$$

where  $(x_i, y_i)$  are the vertex positions for  $i$  ranging from 1 to  $n$ . For a deformed regular quadrilateral, i.e. a deformed square, with the unit area,  $(x_i, y_i) \in \left(\pm \frac{1}{\sqrt{2}}, \pm \frac{1}{\sqrt{2}}\right)$  and the above equation becomes

$$P = \sqrt{2} \left[ \sqrt{D_{xx}^{-2} + (D_{xx} - D_{xy})^2} + \sqrt{D_{xx}^{-2} + (D_{xx} + D_{xy})^2} \right]. \tag{2.21}$$

For any given number of sides  $n$ , the isoperimetric inequality establishes a relationship between the perimeter  $P$  of a polygon and its area, i.e., the perimeter  $P$  of any polygon with a fixed area must be greater than  $P_{reg}$ , where  $P_{reg}$  is the perimeter of a regular polygon with the same area. For example, for a square (where  $n = 4$ ),  $P_{reg}$  is 4, as this is the perimeter of a regular square with unit area. In this context, the condition  $P(D_{xx}, D_{xy}) \geq P_{reg}$  defines a specific set of conditions or a ‘manifold’ in the plane defined by the deformation tensor components  $D_{xx}$  and  $D_{xy}$ . Here,  $P(D_{xx}, D_{xy})$  is the perimeter of a deformed polygon as given by the equation referred to as Eq. (2.21). This manifold represents all the possible deformed polygons that meet the isoperimetric constraint, i.e., their perimeters are equal to or greater than the perimeter of the corresponding regular polygon with a unit area.

The highest value of  $D_{xy}$  along the isoperimetric contour defines  $D_{xy}^{\max}(P)$ , which represents the maximum simple shear that a cell can withstand while keeping both its area and perimeter

constant. The maximum shear, denoted as  $\gamma = \gamma_C = D_{xy}^{\max} \propto (p_0 - p_0^*)^{1/2}$ . This proportionality precisely corresponds to the point of strain-driven solidification at  $\gamma = \gamma_C$  observed in simulations, and the exponent 1/2 in this relationship aligns exceptionally well with the scaling of  $\gamma_C$  near the critical perimeter  $p_0^*$ .

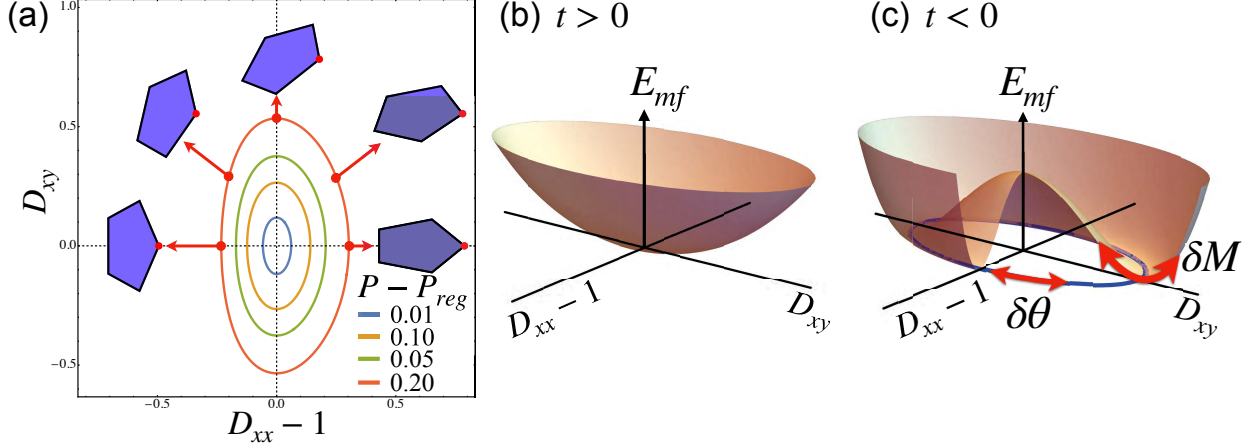


**Figure 2.10: Illustration of the Mean Field Theory (MFT).** (a) We use a single polygon as a representative cell in the MFT. When the perimeter of a polygon is larger than that of its regular counterpart, deformations can lead to a family of isoperimetric shapes defined by the contours shown for a 5-sided polygon at various values of  $P > P_{reg} \approx 3.812$ . (b) The MFT energy landscape as a function of  $(D_{xx} - 1, D_{xy})$  for  $t > 0$  has a unique ground state at  $D_{xx} = 1, D_{xy} = 0$ , as depicted in Eq.(2.23). (c) The MFT energy landscape as a function of  $(D_{xx} - 1, D_{xy})$  for  $t < 0$  has degenerate ground states which are connected by Goldstone modes in the  $\delta\theta$  direction, as depicted in Eq.(2.23).

In the deformation tensor space, the isoperimetric contours are centered at the point  $(D_{xx} = 1, D_{xy} = 0)$ , which represents the identity deformation. For small deviations from the regular perimeter  $P_{reg}$ , these contours can be closely approximated by an ellipse. To analyze this, we introduce polar coordinates with a radius  $M(\theta)$  and a polar angle  $\theta$ , where  $D_{xx} - 1 = M(\theta) \cos \theta$  and  $D_{xy} = M(\theta) \sin \theta$ . Expanding the perimeter equation (Eq. (2.21)) to the second order in  $M$  yields the approximation:

$$P \approx P_{reg} + \frac{15}{32} P_{reg} \left[ 1 + \frac{3}{5} \cos(2\theta) \right] M(\theta)^2. \quad (2.22)$$

Using this approximation (Eq. (2.22)), we can reformulate the vertex model energy (Eq. (2.2)) into a Landau-type energy expression:

$$E_{mf} = \frac{1}{2}t\alpha m(\theta, M)^2 + \frac{1}{4}\beta m(\theta, M)^4, \quad (2.23)$$

where  $m(\theta, M) = [1 + \frac{3}{5}\cos(2\theta)]^{1/2}M$  is the order parameter,  $\alpha = \frac{60}{32}p_0^{*2}$  and  $\beta = \frac{30}{32}p_0^{*2}$  are positive constants, and  $t = \frac{(p_0^* - p_0)}{p_0^*}$  controls the proximity to a continuous phase transition in  $m(\theta, M)$ .

For  $t > 0$ , the energy function  $E_{mf}$  has a single minimum at  $m^* = 0$  (as shown in Fig. 2.10b), corresponding to a rigid state. Conversely, when  $t < 0$ , the minimum  $m^*(\theta, M)$  aligns with the isoperimetrically degenerate liquid state. In the energy landscape, these states are interconnected by a Goldstone mode, as depicted in Fig. 2.10c [64, 65].

The MFT also explains the origin of the nonlinear elasticity and the critical exponents in the system. For  $t > 0$ ,  $E_{mf}$  has a single minimum at  $m^* = 0$ , which corresponds to an undeformed solid state. Using Eq.(2.23), deformations away from it can be expressed as

$$\begin{aligned} \sigma &= \partial E_{mf} / \partial m = \alpha tm + \beta m^3 \\ G &= \partial^2 E_{mf} / \partial m^2 = \alpha t + 3\beta m^2. \end{aligned} \quad (2.24)$$

For small  $m$  values, this formulation recovers linear elasticity with  $G_0 = \alpha t \propto (p_0^* - p_0)$ . In the regime of large  $m$  values, the response is nonlinear, characterized by  $G \propto \sigma^{2/3}$ . The cross-over stress between the two regimes can be estimated by  $\alpha t \approx 3\beta m^2$ , as at the crossover, the linear and nonlinear terms in the expression for  $G$  are of the same order. We get  $\sigma_c = \alpha tm + \beta m^3 = 2\beta\alpha^{3/2}t^{3/2} \propto (p_0^* - p_0)^{3/2}$ . These theoretical predictions align remarkably well with the results obtained from simulations.

## 2.6 Discussion and Conclusion

In this project, we use a Voronoi-based vertex model as a numerical framework for probing the nonlinear mechanical behavior of dense biological tissue under large shear deformations. On the one hand, for a tissue that initially possesses fluid-like characteristics in its undeformed state, this fluid nature is lost via strain-driven solidification once a critical strain threshold is reached. Through the application of Mean Field Theory (MFT), we have established that these fluid states comprise a subset of isoperimetric degenerate ground state tissue configurations, linked by way of a Goldstone mode. This isoperimetric degeneracy persists until a critical strain is denoted as  $\gamma_C$ , beyond which the tissue undergoes a marked transition towards strain-induced stiffening, resulting in a substantial increase in rigidity. This transition in strain-induced rigidity is characterized by a discontinuity, as evidenced by a discernible leap in the shear modulus.

On the other hand, in regions surpassing  $\gamma_C$ , solid tissues also manifest pronounced nonlinear tendencies and stress-stiffening behaviors, aligning closely with empirical observations reported in prior experimental studies [51]).

The focal point of our study has centered on the shear-startup properties exhibited by the tissue, emulating behaviors akin to those observed in experiments involving tissue stretching [66, 51, 67]. A forthcoming avenue of interest lies in comprehensively exploring the rheological response of the tissue under conditions of steady shear at finite strain rates.

Noteworthy findings of this study reveal that the tissue's yield stress ( $\sigma_{yield}$ ) and shear modulus ( $G$ ) do not converge at the same value of the cell shape index ( $p_0$ ). This observation strongly intimates that the realms of steady flow and shear startup are governed by distinct critical points, thus emphasizing the nuanced and multifaceted nature of the tissue's mechanical response.

Our results have inspired follow-up studies. For example, by combining simulations and continuum theory to examine the nonlinear shear rheology of a vertex model across a full range of

shear rates, Fielding et al. formulate a new rheological constitutive model that links cell shape to flow [68]. This continuum model incorporates elements of shear-driven solidification and nonlinear elasticity in epithelial tissues and shows abilities to capture the zero-shear solid-liquid transition and strain stiffening transitions mentioned above, as well as the full nonlinear stress versus strain behavior following the inception of shear and the steady-state flow curves of stress versus shear rate. Moreover, the mechanical response and solid-liquid transition in tissues are examined across a full spectrum of shear rates, which goes beyond the scope of quasistatic shearing, enhancing our understanding of tissue mechanics at a fundamental level.

## Chapter 3

### Beyond Confluence: A Voronoi-based Model with Extracellular Spaces

In various critical biological contexts, including embryonic development, tissue remodeling, wound healing, and invasive processes, the imperative capacity of cells to engage in collective migration has been extensively documented [34, 69]. This collective migratory behavior represents a fundamental mechanism underlying the precise orchestration of cellular dynamics during these pivotal events. Furthermore, during these processes, the mesenchymal phenotypes [70] exhibit a distinctive array of cellular behaviors during movement. These behaviors are characterized by discernible features, including a polarized morphology and dynamic alterations in the cytoskeletal framework. A salient trait of these mesenchymal cells is their inclination to display lower confluence, which culminates in a reduced occurrence of triple junctions. This nuanced reduction in cell-cell contact endows mesenchymal cells with an enhanced adaptability to dynamic microenvironments. This heightened adaptability, in turn, augments their capacity for both individual and collective migratory processes, and invasive behavior, as well as an increased responsiveness to a spectrum of chemical and mechanical cues. In stark contrast, epithelial tissues maintain an intricately organized structural configuration, characterized by a densely packed arrangement of cells. This structural organization is further fortified by an extensive network of intercellular contacts, including adherent junctions, tight junctions, and desmosomes [71]. Collectively, these junctions collaborate to forge a cohesive barrier, an indispensable requisite for crucial physiological functions, including absorption, secretion, and the provision of a protective epithelial layer.

Unlike mesenchymal cells, in many biological processes, epithelial cells form a confluent surface where there is no free space between any of the cells and find themselves encased by their neighboring cells, evoking an analogy with the confinement observed in glassy materials [72]. Despite these constraints, cells within an epithelium retain the capacity to engage in collective

movement, orchestrating their locomotion as coherent sheets rather than discrete entities. This orchestrated movement is contingent upon the synchronized interactions between adjacent cells, thus ensuring the preservation of tissue integrity and function [34]. This profound dichotomy in cellular behavior serves as a lynchpin in elucidating the multifaceted roles that these distinct tissue types assume in physiological processes. Furthermore, it begets a myriad of critical challenges in the realms of active matter physics and non-equilibrium statistical mechanics [73, 74, 75]. These challenges encompass a wide spectrum of inquiries, ranging from the mechanical underpinnings of cellular movement to the collective behavior of cells within tissues, delineating a fertile ground for interdisciplinary research at the interface of biology and physics. Additionally, understanding these cellular behaviors at a fundamental level holds implications for a myriad of fields including tissue engineering, regenerative medicine, and targeted therapeutics.

These kinds of confluent situations are well captured by previous vertex models. However biological tissues are not always confluent, and non-confluent tissues are not trivial versions of their confluent counterparts. First, non-confluent tissues are often found in regions that are undergoing rapid growth or repair. For example, the wound healing process describes tissue closing up an intercellular gap by growth and collective motion. When a wound is healing, the surrounding epithelial tissue must rapidly migrate and proliferate to close the wound. Tissues during wound healing are usually not fully packed together, which allows more movement and dynamic interactions between cells. Obviously, for the same reason, non-confluent tissues are easier for nearby cancer cells to migrate and invade compared to confluent tissues. Second, non-confluent epithelial tissues exhibit different mechanical and dynamical properties, such as stiffness, viscosity, migration, and proliferation rate, than confluent epithelial tissues. These properties can be influenced by the extracellular matrix, cell-cell adhesion and pressure, and cytoskeleton, making it an interesting object to study the underlying mechanisms. For example, increasing tissue confluence leads to a significantly decreased migratory responsiveness of renal epithelial cells to the dedifferentiating morphogenic

signals of hepatocyte growth factor (HGF) and an increased tendency to organize into epithelial tubes [76]. Studying the behavior and properties of non-confluent epithelial tissues is important for understanding how these properties are regulated and how they can be manipulated to promote the tissue wound repair process or inhibit cancer invasion progression. In addition, under some conditions, individual cells or small cell clusters can escape from the bulk confluent tissue and exhibit different phenotypes. This could be relevant for processes such as cancer metastasis [77]. In-vivo experiments in developing zebrafish embryos have revealed that both the intercellular unoccupied spaces and the dynamics of cell–cell contacts influence the physical and biological states of the tissue [36].

Previous studies on epithelial tissues have utilized confluent vertex models and Voronoi-based models to reveal density-independent rigidity transitions in dense epithelial systems. However, the ability of these models to accurately describe cell movements and tissue properties in low cell density is limited. Therefore, various efforts have been made to devise alternative models that can more accurately describe non-confluent biological tissues. One such model is the cellular Potts model, which has the capability of generating non-confluent phases if the cell-medium energy is lower than cell-cell energy [78]. A generalized version of the vertex model, the so-called active foam model, has also been developed, which allows for a deformable free-shape connected boundary but is not capable of accommodating topology changes [79]. This model allows for more complex cell shapes, which can be beneficial for studying cellular behavior in more realistic conditions. The Subcellular Element model, on the other hand, comprises individual cells composed of numbers of “elements” that have short-range viscoelastic interactions, leading to adaptive cell shapes and intercellular spaces [80, 81]. As the Subcellular Element model excels in capturing the intricate details of cell mechanics in a dynamic, grid-free manner, it demonstrates effectiveness in simulating the complex and dynamic nature of cellular structures and processes, especially in mesoscopic scales [82, 83, 84, 85]. Another model, developed by Kim et al., adds intermediate

non-physical vertices into the vertex model to allow for more complex cell shapes. They further introduced extracellular spaces by simulating them as ‘virtual cells’ with different rules [86]. This approach allows for the investigation of the interplay between cells and their environment.

In addition, Nonomura has proposed a multiphase field model, in which cells are treated as deformable and overlapping active particles, to allow the emergence of intercellular gaps [44]. By representing interfaces as continuous transitions over a finite width, the phase-field approach simplifies the mathematical treatment of problems that would otherwise require complex boundary conditions and geometrical considerations. Due to its unique ability to seamlessly capture the evolution of interfaces and complex shapes without explicitly tracking boundaries, the multiphase field model is a powerful tool in the study of cellular dynamics, cell morphology, collective cell migration, and fluid flows [87, 88, 89, 90, 91]. As it can easily handle topological changes such as domain division, people have also used it in biological processes involving cell division [92].

It is important to note that while these various models have made progress in accurately describing non-confluent biological tissues, they have also become increasingly complex to achieve this goal. For instance, the Subcellular Element model may be computationally expensive due to the large number of elements in each cell. The vertex model with intermediate non-physical vertices and the multiphase field model may also be complex and difficult to interpret. However, these models also become increasingly complex and difficult to implement and can require significant computational resources. Therefore, it is important to continue to explore simpler models that accurately describe the behavior of cells and tissues, while also maintaining the simplicity and ease of use of earlier vertex models.

Due to the reasons mentioned above, there has been a growing need to develop new models that achieve this balance between accuracy and simplicity. One such effort was made by Teomy et al., who extended the confluent Voronoi approach to create the Finite Voronoi model (FVM) [42]. This model aimed to bridge the gap between confluent and non-confluent tissue mechanics models. In

the FVM, a maximal size for the cells guarantees that the resulting tissues are non-confluent at sufficiently low densities. The model has received considerable attention because of its ability to capture the characteristics of epithelial tissues and their behaviors. While the FVM has been subject to extensive static morphological and thermal fluctuation analysis, there has been little exploration of the dynamical organization of the multicellular structure and collective motility. Further investigation of the dynamics of the FVM is crucial for understanding the collective behavior of cells in tissues and their mechanical properties.

As the FVM provides a promising foundation for the development of a simpler and more computationally efficient model that can capture the dynamical behavior of the multicellular system, we adopt the following Active Finite Voronoi (AFV) model from the previous study to more effectively model and understand the complex biological systems of living organisms [93].

### 3.1 Active Finite Voronoi (AFV) Model

Among the efforts to bridge the gap between the confluent tissue mechanics and non-confluent cell motility, Teomy and co-workers built a Finite Voronoi model (FVM) by introducing a length scale  $l$  to the Voronoi model, requiring that each cell must not occupy space exceeding the maximum allowed distance  $l$  from the reference point that describes its location. As a result, for Voronoi tessellation edges lie within the distance to their corresponding cell reference points, and cell boundaries are described by polygonal segments at the cell-cell interface. On the other hand, for Voronoi tessellation edges beyond the  $l$  vicinity, cell boundaries are replaced by circular arcs of radius  $l$ , leading to the emergence of cell-unoccupied region interfaces and intercellular gaps. For an isolated cell, i.e. its reference point is far away from other cells' reference points, the cell contour will be a circle of radius  $l$ . Similar to the vertex model, the effective energy function is

$$\tilde{E} = \sum_{i=1}^N [K_A(\tilde{A}_i - \tilde{A}_0)^2 + K_P \tilde{P}_i^2] + \lambda^{(c)} \sum 2l^{(c)} + \lambda^{(n)} \sum l^{(n)}, \quad (3.1)$$

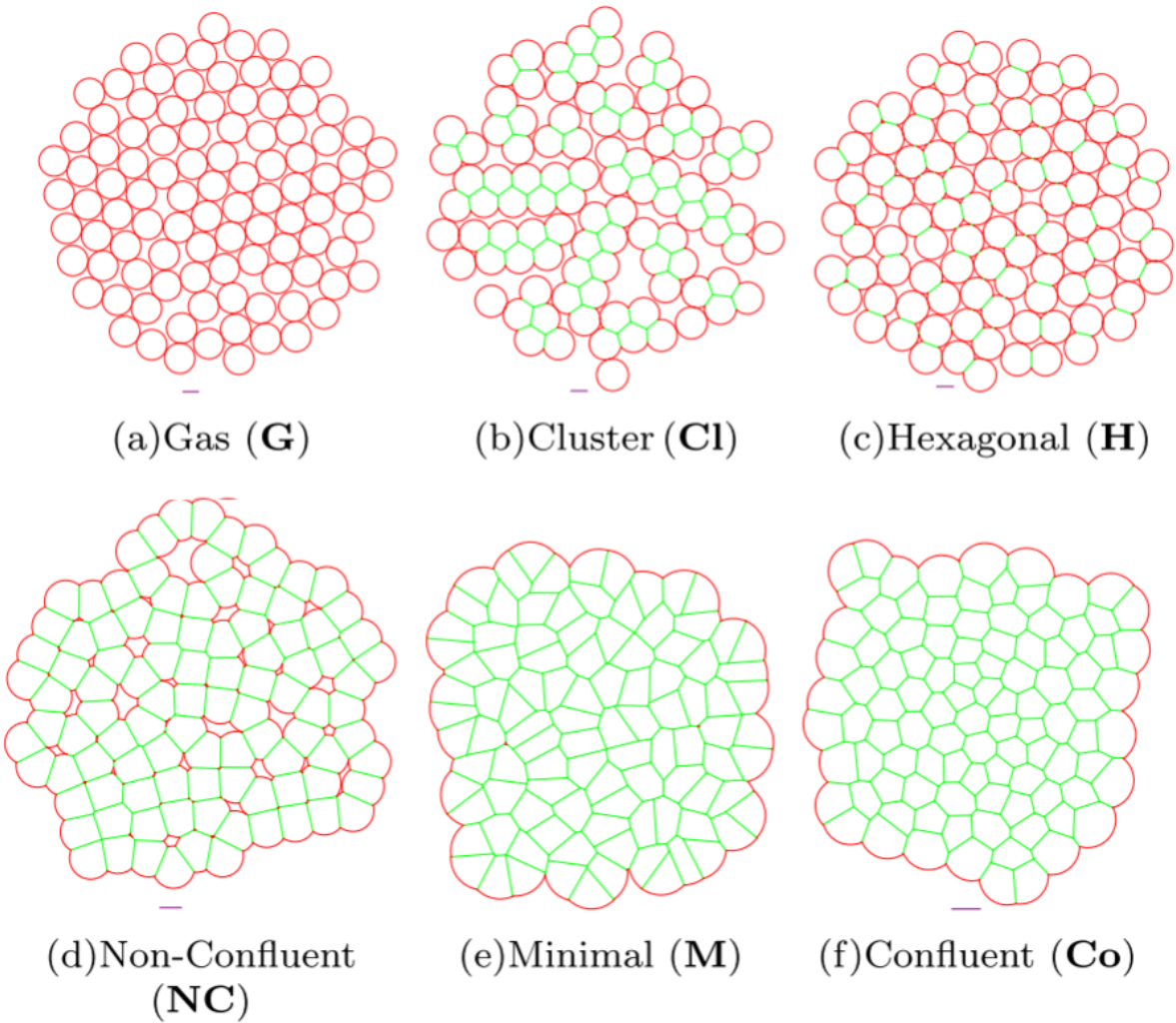


Figure 3.1: The static phases of the Finite Voronoi model (FVM) adapted from [42]. The shown snapshots are systems starting from the same initial condition with  $N = 100$  cells and zero temperature. Green lines are straight edges between adjacent cells, and red lines are the non-contacting edges in the form of circular arcs. The purple line below each configuration is of length  $R = 1$  to see the different scales.

where  $K_A$  and  $K_P$  are the area and perimeter elasticities.  $\{\tilde{A}_i\}$  and  $\{\tilde{P}_i\}$  are cell perimeters and areas, and  $A_0$  is the preferred area. The first term arises from the resistance of cell volume change. The second term  $K_P \tilde{P}_i^2$  results from energy cost of cortex deformation [39, 26].  $\lambda^{(c)}$  and  $\lambda^{(n)}$  are correspondingly cortical tensions on contacting edges and non-contacting edges. In epithelial cells, non-contacting edges tend to carry higher tension than contacting edges in similar conditions. This cortical tension difference originates from rich feedback between adhesion molecules and cytoskeletal dynamics [94]: as the normal projection of cortical tension on non-contacting edges (cell-unoccupied region interfaces) is balanced by cortical elasticity, the tension required for force balance is lower for contacting edges (cell-cell interfaces) due to the contribution of adhesion from neighboring cells. The factor of 2 in the third term comes from the fact that each contacting edge is shared by two cells. Using the relation  $\sum_{i=1}^N \tilde{P}_i = \sum_{i=1}^N \tilde{L}_i^{(n)} + \sum 2l^{(c)}$ , where  $\tilde{L}_i^{(n)}$  is the total length of non-contacting edges in the  $i$ -th cell, the above equation can be simplified to

$$\tilde{E} = \sum_{i=1}^N K_A (\tilde{A}_i - \tilde{A}_0)^2 + K_P \left( \tilde{P}_i + \frac{\lambda^{(c)}}{2K_P} \right)^2 + (\lambda^{(n)} - \lambda^{(c)}) \tilde{L}_i^{(n)} - \left( \frac{\lambda^{(c)}}{2K_P} \right)^2, \quad (3.2)$$

where the last term is a constant and can be dropped. This equation can be further simplified in two ways: On one hand,  $l$  is used as the length unit in the system to dedimensionalize perimeter and area quantities, i.e. let  $P_i = \tilde{P}_i/l$ ,  $L_i^{(n)} = \tilde{L}_i^{(n)}/l$ ,  $A_i = \tilde{A}_i/l^2$ , and  $A_0 = \tilde{A}_0/l^2$  be all dimensionless. We also introduce  $P_0 = -\frac{\lambda^{(c)}}{2K_P l}$  as the adimensional preferred cell perimeter. On the other hand,  $K_A$  is extracted from the tensions and elastic coefficients, which gives  $k_P = K_P/K_A$ , along with  $\Lambda = (\lambda^{(n)} - \lambda^{(c)})/K_A$ , the normalized tension difference coefficient between contacting edges and non-contacting edges. A big  $\Lambda$  value will encourage cells to form cell-cell interfaces with neighbors and eliminate intercellular gaps to reduce the total length of non-contacting edges. With these transformations, the simplified tissue effective energy function can be expressed as

$$E = \sum_{i=1}^N (A_i - A_0)^2 + k_P (P_i - P_0)^2 + \Lambda L_i^{(n)}, \quad (3.3)$$

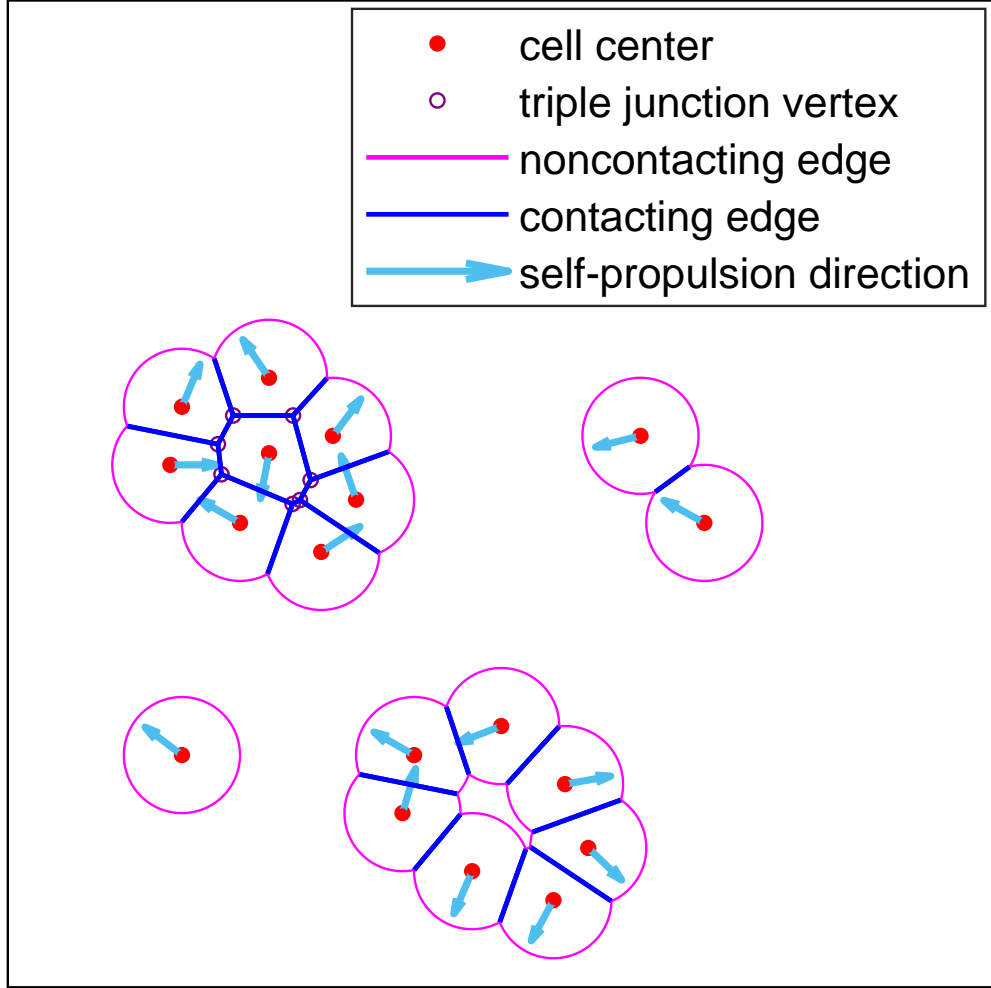


Figure 3.2: An example of a tissue snapshot from the AFV model illustrating its salient features. The red dots denote the cell centers. The blue lines represent contacting edges shared by two cells, and the pink curves represent non-contacting edges, which are circular arcs with radius  $l$ . Triple junction vertices that connect three cells are indicated by hollow purple dots. The cyan arrows indicate the polarity directions of the self-propulsion force applied to the cell centers. Note that isolated cells are circular.

The characterization of cell movement can be a complex process that involves numerous mechanisms. First, the effective mechanical interaction force experienced by cell  $i$  is defined as  $\mathbf{F}_i = -\nabla_i E$ . Additionally, cells can move due to the self-propelled force applied to their centers. To simplify the representation of motile cell dynamics, we adopt the concept of polarity as a simplified representation without diving into the detailed mechanism of the front or rear characterization of cell movement. To model this behavior, as in SPP and SPV models, cells are assigned a polarity

vector  $\hat{n}_i = (\cos \theta_i, \sin \theta_i)$ , where  $\theta_i$  is the polarity angle that decides the direction of  $\hat{\mathbf{n}}_i$ . The self-propulsion force of constant magnitude  $v_0/\mu$  is applied along  $\hat{\mathbf{n}}_i$ , where the mobility  $\mu$  is the inverse of a frictional drag. These forces cooperatively control the over-damped equation of motion of cell center  $\mathbf{r}_i$  as

$$\frac{d\mathbf{r}_i}{dt} = \mu \mathbf{F}_i + v_0 \hat{\mathbf{n}}_i. \quad (3.4)$$

The polarity vector  $\hat{n}_i$  allows for the directional movement of cells while the self-propulsion force,  $v_0/\mu$ , enables cells to move in the direction determined by the polarity vector. The inverse proportionality of mobility  $\mu$  to the frictional drag experienced by the cell ensures that the force applied to the cell does not negatively affect its motion. Specifically, here we model the dynamics of a motile cell as a unit vector that undergoes Brownian rotational diffusion,

$$\partial \theta_i = \eta_i(t), \langle \eta_i(t) \eta_j(t') \rangle = 2D_r \delta(t - t') \delta_{ij}, \quad (3.5)$$

where  $\eta_i(t)$  is a white Gaussian noise process with zero mean and variance  $2D_r$ . The magnitude of the angular diffusivity,  $D_r$ , is a measure of the memory of stochastic noise on self-propelled force angle in the system. This leads to a polarity persistence timescale  $\tau = 1/D_r$ . When  $D_r$  is small, the polarity direction  $\hat{\mathbf{n}}_i$  changes slowly, resulting in a more persistent self-propelling force. However, for large values of  $D_r$ , the corresponding persistence timescale  $\tau \rightarrow 0$  is much shorter than other dynamics time scales in the system. In this case, Eq. (3.5) approaches simple memoryless Brownian motion. The value of  $D_r$  has a significant impact on the mechanical properties and behavior of the tissue. It has been observed in the SPV model that increasing  $D_r$  can significantly decrease tissue fluidity at fixed cell motility. This interesting phenomenon suggests that a solid-like tissue at large  $D_r$  can be fluidized and start to flow simply by reducing its  $D_r$  value [40]. This approach allows us to study the impact of random rotational diffusion on the cell's movement.

In this study, we aim to investigate the dynamics of cells in a medium-density environment. We simulate a system consisting of  $N = 400$  cells under periodic boundary conditions. The size of the box  $L$  is chosen such that the packing fraction  $\phi = 0.5 = N\pi/L^2$ . This choice is advantageous as it maintains the density of self-propelled cells even with high diffusivity, and simulates scenarios where cells can freely enter and exit the field of interest while keeping the overall cell count relatively stable. The results presented correspond to specific parameter values, such as  $k_P = 1$ ,  $D_r = 1$ , and  $\Lambda = 0.2$ , reflecting a relatively small difference in contacting and non-contacting edge tensions. Unless otherwise specified,  $A_0 = \pi$  to reflect the preferred area in an isolated state. Modifying these parameters would not change the phase diagram's qualitative features, but would only shift the phase boundaries' locations.

To initiate the simulation, we initialize the system with  $P_0$  ranging from 4 to 9 as a single connected bulk and relax it to a steady state at zero temperature. We then introduce  $v_0$  ranging from 0 to 2.7 and perform molecular dynamics simulations using Euler's method, with  $10^6$  integration steps and a step size of  $dt = 0.01$ . The resulting data are then analyzed to investigate the system's behavior and its various phases. By systematically varying the simulation parameters, we can identify the critical values that mark the onset of different phases and examine the properties of each phase in detail.

### **3.2 Motility and Cell-Cell Interactions Induce a Clustering Transition**

During various biological processes like embryonic development, tumor progression, and wound healing, migrating cells often undergo transitions between dispersed individual states and clustered multicellular collectives [95]. The importance of these transitions in inducing arrested motility and coordinated behaviors has been recognized in confluent scenarios. However, the behaviors and origins of such transitions in non-confluent low-density scenarios remain unclear. Recently, an in-vivo experiment has shown that a small decrease in adhesion-dependent cell connectivity below a critical value leads to a rigidity phase transition in zebrafish blastoderm [96]. It is essential to

understand the underlying mechanisms that drive such transitions and how these transitions are affected by various factors to gain a more comprehensive understanding of cell migration.

In recent years, vertex-based models have been widely used to study cell dynamics in tissues, especially scenarios where tightly packed cells form confluent epithelial monolayers [27]. However, the abilities of these models to simulate how cell connectivity affects global dynamics and tissue properties are limited. On the other hand, the previous study using the FVM [42] has not analyzed the structural organization of cell clusters over time. Thus, we would like to fill this gap in the literature about cellular connectivity and clustering, since the structural organization of cell clusters is a crucial aspect of tissue behavior.

We characterize the level of cell clustering by first analyzing the normalized giant cluster size. The term ‘giant cluster’ refers to the largest cluster in the given configuration of cells. The normalized giant cluster size is defined as the ratio of the number of cells in the giant cluster to the total number of cells in the system, denoted as  $N_{GC}/N \in (0, 1]$ . This serves as an order parameter for cluster formation, as it quantifies the extent to which cells are clustered together. To identify contiguous clusters, we consider two cells to belong to the same cluster if they share a contacting edge or if the distance between their centers is less than  $2l$ . The presence of a contacting edge between two cells indicates that they are in direct physical contact, which can facilitate the formation of clusters. This definition allows us to track the evolution of cluster size and structure over time. Our analysis builds on previous studies of phase transitions in cell clustering, such as the work by Meder et al. who identified the existence of a critical point at which the system undergoes a phase transition from a dispersed to a clustered state [97]. By characterizing the clustering behavior of cells using the normalized giant cluster size and the definition of contiguous clusters, we hope to gain insights into the mechanisms underlying this phase transition and the factors that influence the formation and stability of cell clusters.

In Fig. 3.3(a), we plot the normalized giant cluster size  $N_{GC}/N$  as a function of motility  $v_0$

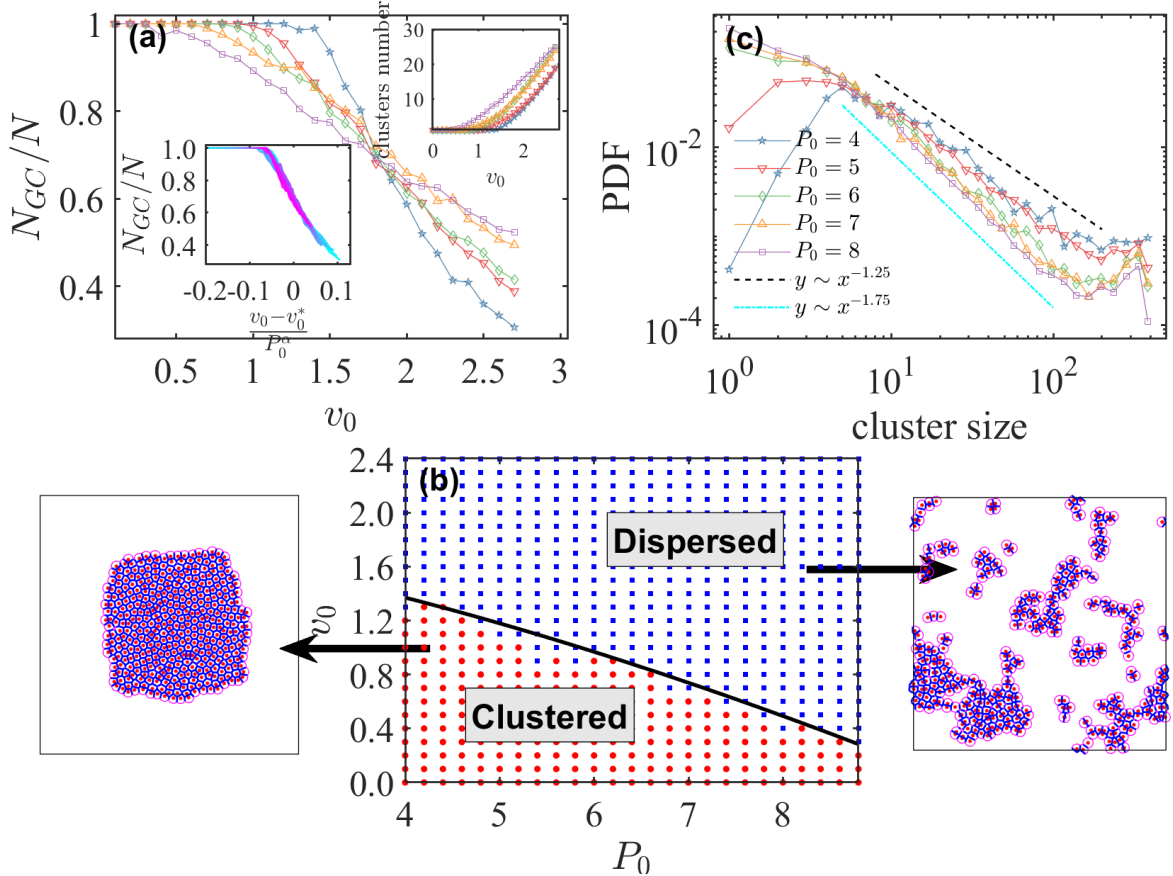


**Figure 3.3: Formation of multicellular clusters in the AFV model.** (a) The normalized giant cluster size  $N_{GC}/N$  as function of  $v_0$  at different  $P_0$  and  $\Lambda = 0.2$ . An initially connected tissue undergoes a segregation transition at a critical activity  $v_s(P_0)$ . (a-left-inset)  $N_{GC}/N$  vs  $(v_0 - v_0^*)/P_0^\alpha$  for different  $P_0$  values. (a-right-inset) The number of contiguous clusters as a function of  $v_0$  for different  $P_0$ . (b) Tissue clustering phase diagram in the  $v_0$ - $P_0$  plane for  $\Lambda = 0.2$ . The red data points correspond to a clustered state, as the blue points correspond to dispersed tissues. The black line corresponds to  $v_s(P_0)$ . The two sample tissue snapshots are from  $P_0 = 4.2, v_0 = 0.1$  (clustered state) and  $P_0 = 4.2, v_0 = 2.1$  (dispersed state). The red dots in the snapshots are cell centers, the blue lines are contacting edges between adjacent cells, and the pink arcs are the non-contacting edges. The black rectangles annotate the periodic boundaries. (c) shows the probability distribution function (PDF) of cluster size for  $N = 400$  systems at  $v_0 = v_0^*$ . The dashed line and dot-dashed line correspond to power-laws of exponent  $-1.25$  and  $-1.75$ , correspondingly, as visual aids for eyes.

for tissues at various values of  $P_0$  and a fixed  $\Lambda = 0.2$ . A motility-driven dispersal transition is observed: at low  $v_0$ , cells stay in a single giant cluster, corresponding to  $N_{GC} = N$ . As the motility increases, the tissue breaks up into smaller clusters, indicated by a decrease in the normalized giant cluster size. Our simulations reveal a clear transition from a clustered state, where cells form a single giant cluster, to a dispersed state, where cells are organized in multiple smaller clusters, as the motility of cells increases. Remarkably, we find that the transition occurs for all values of  $P_0$  tested, albeit with different degrees of sharpness.

Strikingly, all the curves intersect at a common point  $v_0^* \approx 1.85$ , which serves as a universal crossover irrespective of  $P_0$ . Notably, for  $v_0 < v_0^*$ ,  $N_{GC}/N$  decreases as  $P_0$  increases, whereas for  $v_0 > v_0^*$ , the trend is reversed, and  $N_{GC}/N$  increases with  $P_0$ . Based on these findings, we hypothesize that a universal scaling relation could describe the behavior of  $N_{GC}/N$  below and above  $v_0^*$ . Based on these observations, we hypothesize that the behavior of  $N_{GC}/N$  below and above  $v_0^*$  could be described by a universal scaling relation

$$N_{GC}/N = G\left(\frac{v_0 - v_0^*}{P_0^\alpha}\right), \quad (3.6)$$

where  $G$  denotes a universal function.

To test this hypothesis, the data were replotted in terms of  $N_{GC}/N$  vs.  $\frac{v_0 - v_0^*}{P_0^\alpha}$  based on the above ansatz. This was done to obtain a collapse to a master curve, which would confirm the existence of a universal scaling relation. The results of the replotted data were presented in Fig. 3.3(a) bottom-left inset. A collapse to a master curve was indeed observed, with  $v_0^* = 1.85 \pm 0.06$  and  $\alpha = 3/2 \pm 0.12$ . This universal collapse supports the hypothesis that the transition will always occur at a motility threshold

$$v_s(P_0) = v_0^* - cP_0^\alpha, \quad (3.7)$$

where  $c = 0.06 \pm 0.005$  is a positive constant obtained through fitting to the location where  $N_{GC}/N$

drops below 99%.

In addition, we plot the number of clusters as a function of motility  $v_0$  in Fig. 3.3(a) top-right inset. The obtained results confirm the observations presented in the previous section, wherein it was shown that at low motility values, cells tend to form a single large cluster, while at higher values of  $v_0$ , this cluster breaks down into smaller fragments, resulting in an increased number of clusters.

Then the phase boundary between the clustered and dispersed states can be seen in Fig.3.3(b), where Eq.(3.7) is plotted. The clustered region is characterized by a high value of  $N_{GC}/N$  and a low number of clusters. When the segregation transition point is exceeded,  $N_{GC}/N$  starts to decrease and the number of clusters increases, indicating the onset of the dispersed region. For practical purposes, we classify tissues with  $N_{GC}/N < 0.99$  as being in the dispersed state, which is represented by blue dots in the figure, while those with  $N_{GC}/N \leq 0.99$  are considered to be in the clustering state, represented by red squares. Furthermore, to provide a visual representation of the two states, we include representative snapshots in the figure. It is worth noting that the phase boundary allows for a clear classification of the clustered and dispersed states, and by distinguishing between them one can analyze the mechanisms that drive the system towards either state.

The crossover point  $v_0 = v_0^* \approx 1.85$  in the phase diagram reveals an intriguing regime where the system exhibits a giant cluster of a fixed size, with  $N_{GC}/N \approx 0.7$ , regardless of the value of  $P_0$ . Given the relatively high value of motility at this point, it is natural to question how the system maintains such a large cluster size. To gain insights into this phenomenon, we investigate the cluster size distribution (CSD)  $p(n)$  for different values of  $P_0$  at the crossover point  $v_0 = v_0^*$ , as shown in Fig. 3.3(c). Our analysis indicates that the functional form of the CSD is dependent on  $P_0$ , which suggests that the maintenance of the giant cluster size may be linked to the underlying distribution of cluster sizes.

Specifically, we observe that as  $P_0$  increases, the CSD shifts towards smaller cluster sizes, with a sharper peak at the giant cluster size. This trend is consistent with the observation that the giant cluster remains a fixed size regardless of  $P_0$ , while the number of smaller clusters increases with increasing  $P_0$ . Furthermore, we find that the CSD exhibits a power-law tail for larger cluster sizes, which is indicative of the presence of rare, extremely large clusters. Interestingly, we observe that the exponent of the power-law tail also depends on  $P_0$ : At  $P_0 = 4$ , the CSD initially increases as a power law of  $n$ , where  $n$  represents the cluster size, then as the cluster size approaches the system size ( $N_{GC}$ ), the CSD begins to decay at a power-law rate of  $n^{-1.25}$ . On the other hand, when  $P_0 = 8$ , the CSD follows a faster power-law decay with an exponent of  $n^{-1.75}$ , implying that larger clusters become less probable. These findings suggest that the system's behavior is highly dependent on  $P_0$  and that increasing  $P_0$  can lead to a faster decay of the CSD.

Interestingly, similar exponents have been observed in other active matter systems with clustering or motility-induced phase separation, indicating a commonality in the underlying mechanisms of such systems [98, 99, 100, 101, 102, 103]. However, the broadness of the CSD indicates that the system does not have a typical cluster size. Thus, a multiscale analysis is required to fully capture the system's behavior, which is essential to understanding the collective dynamics of active matter systems.

It is noteworthy that the trends observed in the number of clusters in the current study are consistent with previous findings in the literature, wherein it has been shown that the clustering behavior of cells is dependent on various factors such as cell-cell adhesion, cell-matrix interactions, and motility. Furthermore, it has been demonstrated that the clustering behavior can be modulated by various external factors such as substrate stiffness and topography, which further emphasizes the complex nature of this phenomenon.

Upon meticulously quantifying the steady-state mean size of the cluster, our analytical focus now pivots toward the intricate temporal fluctuations inherent to cluster sizes. This facet of cellular

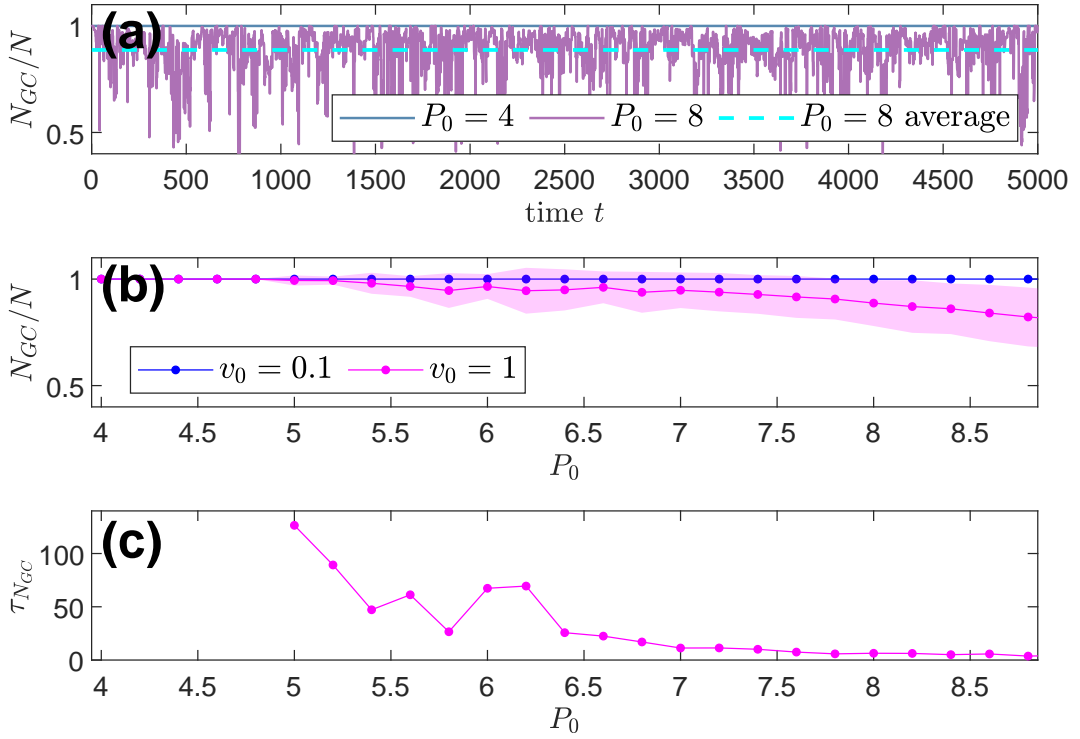


**Figure 3.4: The fluctuation in  $N_{GC}/N$  for dispersed states.** (a) Two sample  $N_{GC}/N$  traces at  $v_0 = 1$ . The solid lines correspond to realizations of  $P_0 = 4$  and  $P_0 = 8$ , respectively. The cyan dashed line indicates the average value of  $P_0 = 8$  as visual aids. (b) The  $N_{GC}/N$  average values of different  $P_0$  at  $v_0 = 0.1$  and  $v_0 = 1$ , respectively, with the shaded band representing the standard deviation. (c) The autocorrelation time of the giant cluster size,  $\tau_{N_{GC}}$ , at different  $P_0$  and  $v_0 = 1$ . For  $P_0 < 5$ , the  $\tau_{N_{GC}}$  values go to infinity and are not displayed on the plot.

behavior is of paramount importance, as it encapsulates the dynamic nature observed within cell clusters. As exemplified by the simulation videos, meticulously provided in the Supplementary Materials, these clusters undergo a continuous interplay of aggregation and disintegration events, depicting a process characterized by its high dynamism. Fig. 3.4(a) presents the temporal fluctuation of  $N_{GC}/N$  for two distinct scenarios. In the context of a clustered state, defined by  $v_0 = 1$  and  $P_0 = 4$ , where the giant cluster maintains stability, the trace of  $N_{GC}/N$  remains a constant horizontal line, signifying an unaltered giant cluster size equivalent to unity. Notably, sporadic instances arise where individual cells transiently disengage from the giant cluster, typically in proximity to the clustering transition. Conversely, as depicted in Fig. 3.4(a, b), a dispersed state ushers in continuous oscillations in the giant cluster size. These fluctuations arise from the dynamic interactions between cells, leading to the transient formation and dissolution of clusters. Through these interactions and coalescence, larger clusters emerge, resulting in an augmented giant cluster size. However, due to the inherent instability of cellular contacts in such a state, these clusters are inherently transient. As time progresses, the clusters disintegrate, resulting in a reduction of the giant cluster size. This perpetual ebb and flow of cluster formation and disintegration gives rise to a dynamic and ever-evolving landscape within the tissue, characterized by the constant evolution of its giant cluster size.

Furthermore, we embark on a thorough investigation of the temporal evolution of cluster sizes, employing the autocorrelation time  $\tau_{N_{GC}}$  of the giant cluster size. This metric serves as a measure of the timescale at which a time series loses correlation with its preceding values. Mathematically, it is defined by the equation:

$$\tau_{N_{GC}} = \sum_{\Delta t=0}^T \text{ACF}_{\Delta t}(N_{GC}), \quad (3.8)$$

where  $\text{ACF}_{\Delta t}(N_{GC})$  signifies the autocorrelation function of  $N_{GC}$  at lag  $\Delta t$ , and  $T$  represents the smallest lag leading to a non-positive autocorrelation function. A protracted autocorrelation time denotes enduring correlations, implying the presence of a stable giant cluster that persists over an

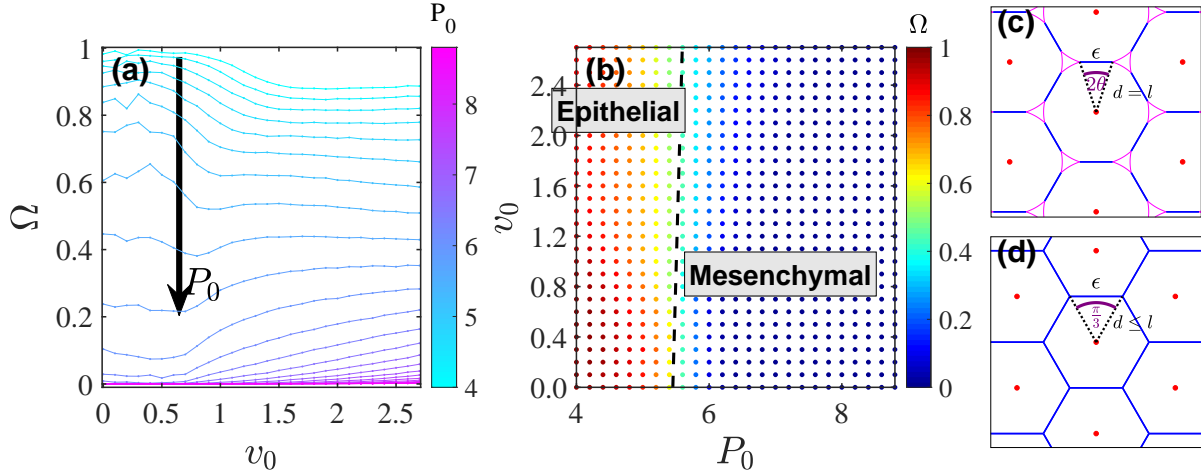


**Figure 3.5: Tissue confluency properties.** (a)  $\Omega$  [defined in Eq. (3.10)] as a function of  $v_0$  for various  $P_0$  values ranging from 4 to 8.8 with an increment of 0.2. The black arrow indicates the curves ordered with increasing  $P_0$ . (b) Tissue confluency phase diagram for  $\Lambda = 0.2$  in the  $v_0$ - $P_0$  plane. The marker color indicates the tissue  $\Omega$  value. The black dashed line corresponds to  $\Omega = 0.5$  and is used as a boundary between the epithelial/confluent state and the mesenchymal/nonconfluent state. (c-d) Illustrative snapshots of a nonconfluent/confluent hexagonal tissue, respectively, were used for our mean-field analysis.

extended temporal span. In Fig. 3.4(c), we present the results for the case of  $v_0 = 1$ . In scenarios where  $P_0 < 5$ , the giant cluster size  $N_{GC}$  consistently equals  $N$ , yielding an autocorrelation time of infinity. This signifies a state of utmost stability, where the giant cluster remains unbroken over a prolonged duration. However, as  $P_0$  surpasses the threshold of 5, the system transitions into a dispersed state. With an escalating  $P_0$ , the autocorrelation time experiences a decrease, indicative of a proclivity toward an unstable cluster state characterized by swifter and more pronounced fluctuations in cluster sizes. This analysis not only provides valuable insights into the dynamic behavior of clusters but also lays the groundwork for a comprehensive understanding of the underlying mechanisms governing these intricate processes.

### 3.3 Epithelial-Mesenchymal Transition Driven by Cell-Shape Changes and Motility

In a confluent epithelial layer, cells pack without intercellular gaps and triple junctions exist between any trio of three neighboring cells. On the other hand, a classical signature of EMT is the reduction of tight epithelial tissue organization. This is accomplished by transcriptional suppression of E-cadherin, a prototypic adhesion molecule responsible for maintaining cell-cell adherens junctions, as well as the downregulation of other adhesion molecules such as claudins [104, 105]. Indeed, tissues undergoing EMT exhibit decreased tight junctions [106, 107] and increased intercellular gaps [37]; in the developmental biology context, these changes can be imaged *in vivo* [108]. In other words, when cells lose their epithelial character as they become mesenchymal, the triple junction vertices will be lost and gradually replaced by the presence of intercellular gaps [109, 37]. This morphology change reduces tensions transmitted at cell-cell junctions and eventually helps enable cell movement [110, 111].

Enlightened by this observation, we then search for an order parameter that could reflect the ratio between triple junction vertices and intercellular gaps to quantify the degree of ‘epithelialness’ of a cell layer. Euler’s polyhedron formula asserts that for a completely confluent cluster of  $N^{(j)}$  cells in open space, the number of triple junction vertices  $V_3^{(j)}$  equals to  $E_c^{(j)} - N^{(j)} + 1$ , where  $E_c^{(j)}$  is the number of contacting edges. When intercellular gaps develop,  $V_3^{(j)}$  will decrease and deviate from  $E_c^{(j)} - N^{(j)} + 1$ . Naturally, a confluency order parameter for a cell cluster  $j$  is defined as

$$\omega^{(j)} = \frac{V_3^{(j)}}{\max(E_c^{(j)} - N^{(j)} + 1, 1)} \in [0, 1], \quad (3.9)$$

where the denominator has a lower bound of 1 to avoid dividing by 0 when the cluster is made of a string of cells. The order parameter  $\omega^{(j)} = 0$  for nonconfluent clusters without any triple junction vertex, and  $\omega^{(j)} = 1$  for confluent clusters. Then for a system containing multiple contiguous

clusters, the global confluence order parameter can be defined as a weighted average of  $\omega^{(j)}$

$$\Omega = \frac{\sum_j N^{(j)} \omega^{(j)}}{\sum_j N^{(j)}}. \quad (3.10)$$

The behavior of  $\Omega$  as a function of  $P_0$  and  $v_0$  is shown in Fig. 3.5(a). When  $P_0$  is low, cells are close-packed with each other, resulting in confluent epithelial tissues with  $\Omega \sim 1$ . As  $P_0$  increases, tissue confluence is lost gradually, indicated by a decreasing  $\Omega$ . The cell motility  $v_0$  has a weak yet opposite effect on  $\Omega$  for systems with different  $P_0$ : cell motility enhances intercellular gaps at low  $P_0$  while it tends to eliminate intercellular gaps at high  $P_0$ . In Fig. 3.5(b), we use  $\Omega = 0.5$  as the threshold to distinguish the epithelial state, where triple junctions are formed at a dominant fraction of the cell-cell interface inside clusters, and the mesenchymal state, where intercellular gaps are preferred. The E/M phase boundary is nearly vertical, indicating a strong dependence on  $P_0$ .

To understand the nature of the epithelial-to-mesenchymal transition in this model, we propose a simple mean-field calculation at zero motility. Here we consider a simple case of a hexagonal cell packing. As illustrated in Fig. 3.5(c), each cell has exactly 6 neighbors that are located on the vertices of a regular honeycomb lattice whose center coincides with the central cell center. Each contacting edge has length  $\epsilon$ , and the corresponding central angle can be set to  $2\theta$  where  $\epsilon = 2 \sin \theta$ . When  $\theta < \pi/6$ , intercellular gaps exist instead of triple junction vertices. The perimeters and area of each cell are given by

$$L^{(n)} = 2\pi - 12\theta, \quad (3.11)$$

$$A = (\pi - 6\theta) + 3 \sin \theta \cos \theta, \quad (3.12)$$

we can allocate the mechanically stable configuration by finding the minimum of Eq. (3.3) with

respect to the angle  $\theta$ , which yields

$$0 = \frac{1}{N} \frac{\partial E}{\partial \theta} = 24k_P(1 - \cos \theta)(12\theta - 12\sin \theta + P_0 - 2\pi) \\ + 24\sin^2 \theta(6\theta - 3\sin 2\theta + A_0 - 2\pi) - 12\Lambda. \quad (3.13)$$

The confluence transition occurs when the solution to Eq. (3.13) is given by  $\theta = \pi/6$ . For the parameter set used in this paper ( $\Lambda = 0.2$ ,  $A_0 = \pi$ ,  $k_P = 1$ ), this condition gives the critical point of  $P_0 = 5.73$ , below which the system is confluent. This provides a reasonable approximation for the phase boundary between epithelial and mesenchymal states in Fig. 3.5(b) in the limit of  $v_0 \rightarrow 0$ .

### 3.4 Glassy Dynamics in Confluent and Non-Confluent Regimes

So far, we have characterized the behavior of the model based on its static structural properties in the multicellular organization. Next, we analyze the dynamic organization of the model. Previous studies suggest that cells can transition from a solid-like to a fluid-like state via separate pathways. For example, during UJT, a tissue can fluidize while remaining confluent [45, 112, 33]. During EMT [111, 37], abolition of epithelial character is a necessary pre-condition for promoted cell migration. Here a natural question arises: while dispersed states must be fluid-like, are all clustered phases solid-like? Further, do the structural transitions observed in our model coincide with dynamical transitions?

To answer this question, we characterize the dynamics of cell motions in the system by measuring the mean-squared displacement (MSD). In order to exclude the contribution of collective rigid-body translations and rotations of a cluster, we compute the MSD based on the relative displacement of cells with respect to their nearest neighbors. In Fig. 3.6(ab), we plot the MSD as a function of time lag  $\Delta t$  for systems with different  $P_0$  and  $v_0$  values. For small  $v_0$  values, cells are caged at long time scales, as indicated by the plateau of MSD. We also plot the total number of  $T_1$  transitions in Fig. 3.7, suggesting arrested motility due to caging effects and broken ergodicity,

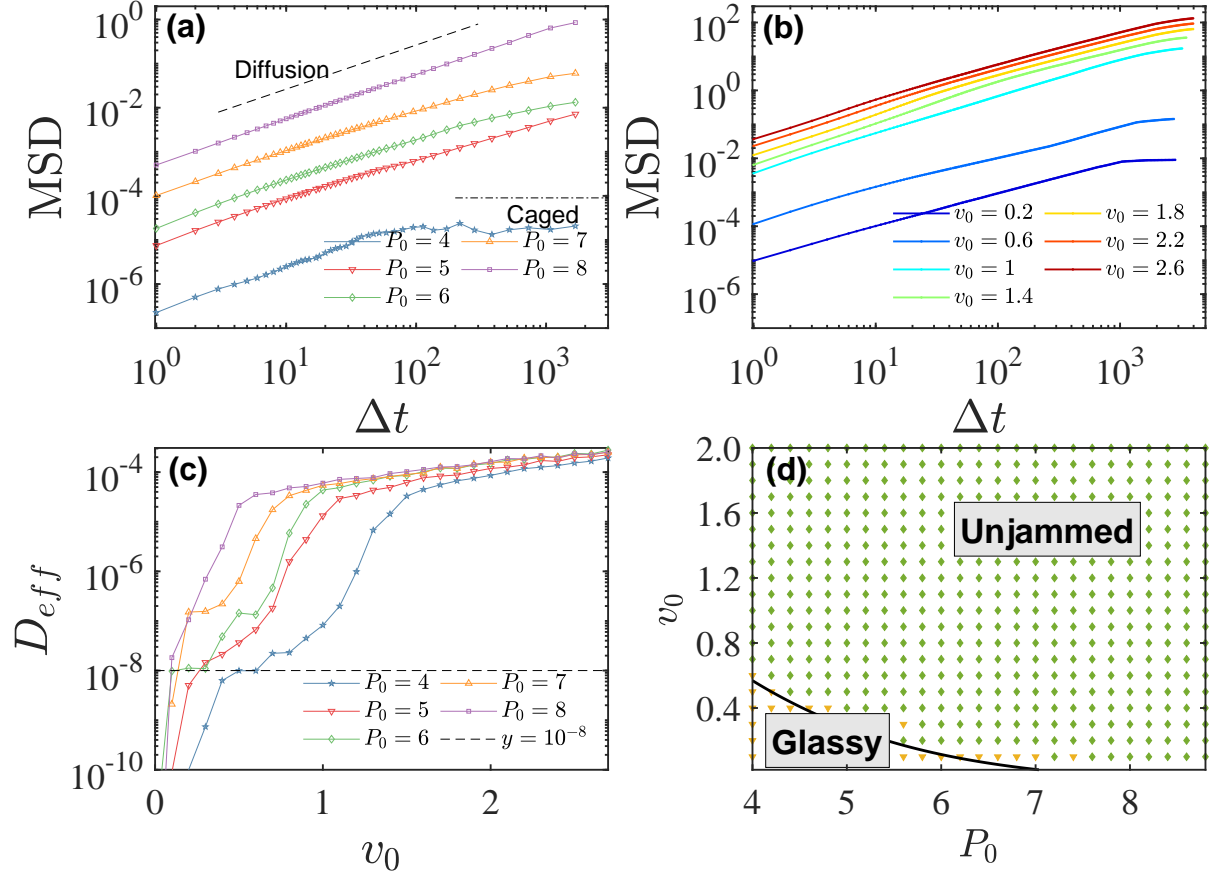


Figure 3.6: **Tissue glassy properties.** (a) MSD traces for different  $P_0$  ranging from 4 to 8 with  $\Lambda = 0.2$  and  $v_0 = 0.4$ . (b) MSD trace for different  $v_0$  with a fixed  $P_0 = 5.6$ . (c) shows  $D_{eff}$  as a function of  $v_0$  for different  $P_0$ . The black dashed line corresponds to  $D_{eff} = 10^{-8}$ . (d) Tissue diffusivity phase diagram as a function of  $P_0$  and  $v_0$ . Orange data points correspond to glassy tissue with vanishing  $D_{eff}$ ; green points correspond to flowing tissues (finite  $D_{eff}$ ).

which are characteristic signatures of glassy dynamics. As  $v_0$  increases, cells begin to uncage and the MSD increases asymptotically as  $MSD \propto \Delta t^\beta$ , where  $\beta \sim 0$  for  $P_0 \leq 4$  and  $\beta \sim 1$  for  $P_0 \geq 7$ .

Following a previous study on tissue glassy dynamics [40], we use the self-diffusivity

$$D_s = \lim_{\Delta t \rightarrow \infty} \frac{MSD(\Delta t)}{4\Delta t} \quad (3.14)$$

as an order parameter to distinguish between glassy and fluid states. We run simulations for  $10^4$  time units and use  $\Delta t = 5000$  to calculate  $D_s$ , which is much longer than the typical caging timescale in a fluid state. The calculated  $D_s$  is presented in the unit of  $D_0 = v_0^2/(2D_r)$ , the free diffusion constant of a self-propelling cell, to accommodate the effect of different motility. Then, the effective diffusivity  $D_{eff} \equiv D_s/D_0$  is used as a diffusion order parameter to distinguish glassy (jammed) and fluid (unjammed) states of cell tissues. The behavior of  $D_{eff}$  at different  $P_0$  and  $v_0$  is shown in Fig. 3.6(c). For a given low  $v_0$  value, the order parameter  $D_{eff}$  does not necessarily follow the order of  $P_0$ ; At large  $v_0$  regime, high  $P_0$  systems always correspond to high  $D_{eff}$  values. In Fig. 3.6(d), we plot the phase diagram of cell dynamics in the  $v_0$ - $P_0$  plane according to  $D_{eff}$ : The glassy states correspond to a finite  $D_{eff}$  below a noise floor of  $10^{-8}$ , and the unjammed states correspond to  $D_{eff}$  that exceeds this threshold.

The position of the dynamical phase boundary suggests that the energy barrier of cell rearrangements is lower than cluster breakup. This difference gives rise to the existence of a stable fluid-like cluster, within which cells exchange neighbors frequently yet stay as members of the same connected cluster. This property is in good agreement with experimental observations of unrestricted epithelial colonies, for example, Madin-Darby canine kidney (MDCK) cells form a confluent epithelial sheet through a highly motile expanding process lasting for one week [113, 114].

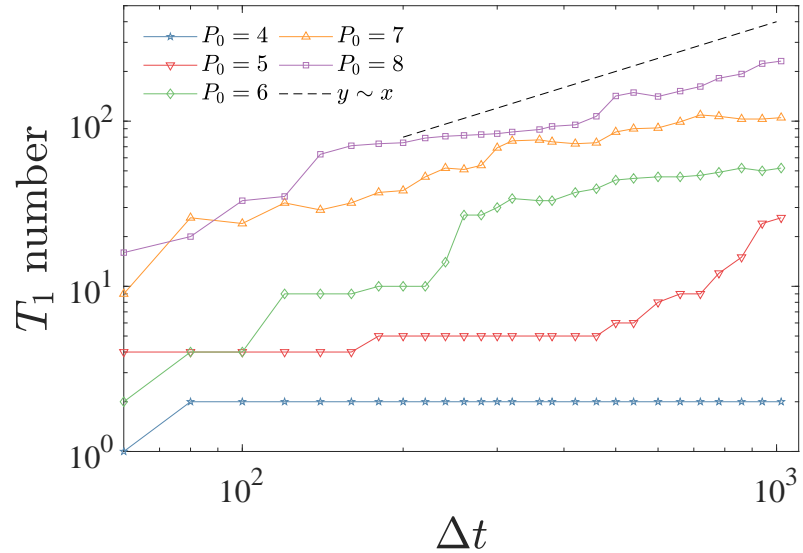


Figure 3.7: The cumulative T1 number traces for different  $P_0$  ranging from 4 to 8 with  $\Lambda = 0.2$  and  $v_0 = 0.4$ .

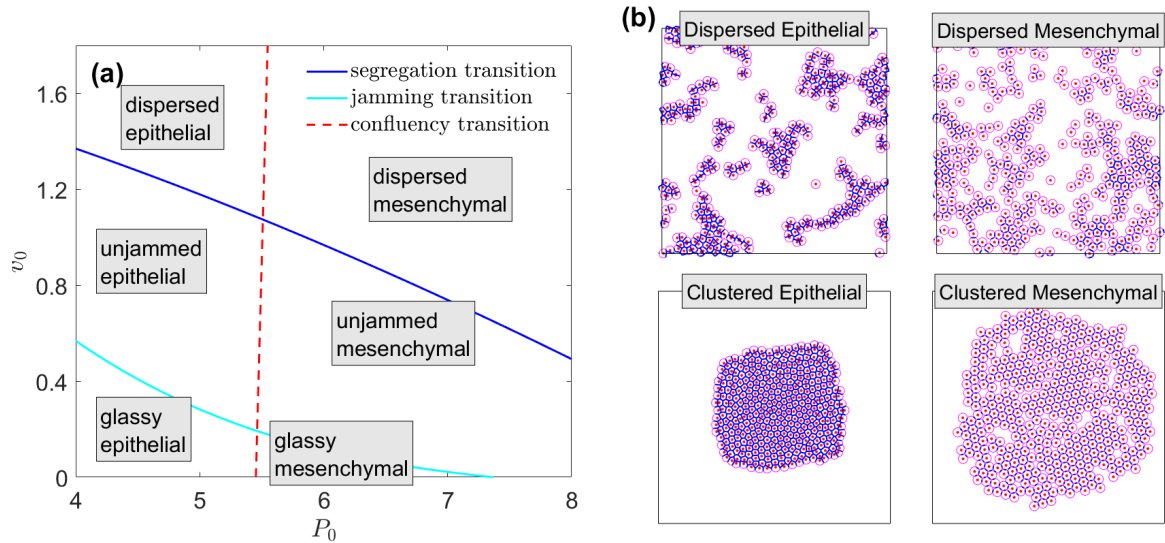


Figure 3.8: **Summary of the phase diagram.** (a) shows the phase diagram with all three phase boundaries on the  $P_0$ - $v_0$  plane for  $\Lambda = 0.2$ . It is qualitatively robust for all values of  $\Lambda$ . (b) shows sample snapshots of four phases. The  $(P_0, v_0)$  values for each state are: Clustered Epithelial phase (4, 0.1); Clustered Mesenchymal phase (8.8, 0.1); Dispersed Epithelial phase (4.4, 2.6); Dispersed Mesenchymal phase (8.8, 2.6). Note that a clustered state could be glassy or unjammed, but a dispersed state must be unjammed.

### 3.5 Phase Diagram of the AFV Model

Having individually examined the three distinct phase transitions in the preceding sections, we now consolidate our findings to comprehensively analyze the complete phase diagram of the AFV model. As elucidated, this model displays three pivotal phase transitions, encompassing a clustering-dispersed transition, an epithelial-mesenchymal transition, and a jamming-unjamming transition. These transitions collectively delineate six distinct phases, as illustrated in Fig. 3.8(a). Namely, for the epithelial side, we have a glassy (and clustered) epithelial phase, an unjammed (and clustered) epithelial phase, as well as a dispersed (and unjammed) epithelial phase; Similarly, for the mesenchymal side, we have a glassy (and clustered) mesenchymal phase, an unjammed (and clustered) mesenchymal phase, as well as a dispersed (and unjammed) mesenchymal phase.

One could immediately find that, unlike the other two transitions, the epithelial-mesenchymal transition is more vertical on the  $P_0-v_0$  plane, indicating the significance of the preferred perimeter parameter ( $P_0$ ) in dictating the transition between epithelial and mesenchymal states. It has been noted that varying levels of cellular adhesion, which can be analogous to the concept of preferred perimeter, profoundly influence tissue behavior. For instance, epithelial tissues, where cells are tightly packed and strongly adherent to one another, exhibit a dominant percentage of cell-cell triple junctions and a high degree of intercellular adhesion. Conversely, in contexts that mimic mesenchymal tissues or situations where cellular cohesion is comparatively lower, higher values of  $P_0$  are akin to conditions where intercellular gaps become more prevalent along cell-cell interfaces. This resonates with the behavior of cells in mesenchymal tissues, where individual cells exhibit less tightly regulated intercellular connections, which make them more prone to dynamic rearrangements and migrations. Therefore, the parameter  $P_0$  could effectively encapsulate the mechanical properties that underlie epithelial-mesenchymal transitions, aligning well with empirical observations in biological systems.

On the other hand, the dynamic interplay of cellular motility, quantified by the parameter  $v_0$ , plays a pivotal role in shaping tissue movements and clustering structures. In biological tissues exhibiting low cell motility, cells tend to display a more stable and static structure and exhibit limited movements. When cellular motility is low, akin to situations with low  $v_0$  values in our model, tissues exhibit a characteristic glassy state. This state is characterized by a tendency for cells to cluster together and experience dynamic arrest. As cellular motility increases, a transition ensues towards an unjammed and dispersed state, characterized by heightened cell rearrangements and increased fluidity within the tissue. These changes are particularly evident in processes such as wound healing, where increased cell motility is essential for efficient tissue repair. In situations with very high  $v_0$ , cells grapple with maintaining connectivity, culminating in a transition towards a dispersed state. This scenario reflects instances in biological systems where excessively high cell motility, if not regulated, can lead to tissue fragmentation and a loss of cohesive structure, for example highly motile cancer cells can disperse from primary tumors and invade surrounding tissues.

The interplay between the preferred perimeter and cellular motility governs the diverse spectrum of tissue phases with different structural and dynamic attributes. To further illustrate these diverse phases, Fig. 3.8(b) presents representative instantaneous tissue snapshots. These snapshots provide a visual depiction of the spatial arrangement and dynamic behavior of cells within the various phases, offering valuable insights into the emergent properties of tissues under different parameter regimes. This comprehensive examination of the AFV model's phase diagram not only enriches our theoretical understanding of tissue behavior but also establishes a solid foundation for exploring the biological implications of these distinct states in real-world contexts.

It is worth mentioning that all of these phase transitions are reversible. For example, by changing  $v_0$  from 0.2 to 2, systems with  $P_0 = 4$  undergo a segregation transition characterized by breaking apart from the bulk. Once the  $v_0$  value is reset to 0.2, small contiguous clusters gradually merge into

bigger clusters, once they collide during drifting. Given a long enough time, systems are always able to revert to the clustered state, even though the final merged clusters have some morphological differences from the original ones; for example, there are more holes inside the clusters, and the contour shapes are more irregular. Thus, there can be some microscopic hysteresis, but none at the level of the macroscopic phase structure.

There are a variety of experimental systems that can be studied with this new model. Wong's group has demonstrated [95] that under the right conditions, cells can form disconnected fractal clusters, similar in principle to those illustrated in Fig. 3.2. In a simple animal (*Trichoplax adhaerens* [115]), overall motility can introduce enough stress to cause fracture of the epithelial tissue; amazingly, the fracture can transition from brittle to ductile behavior [116]. Finally, the issue of the detachment of cell clusters from primary tumors is very much at the heart of trying to understand the initial stages of the metastatic process [117, 118]. The AFV can be used to predict cluster size distributions and thereby provide a check on the accuracy of previous attempts [119] to accomplish this task.

### 3.6 Discussion and Conclusion

In this project, we have introduced a new approach to tissue dynamics, referred to as the Active Finite Voronoi (AFV) model. This model retains the simplicity of the active Voronoi/vertex-based approach, which has made it a very popular strategy for studying confluent epithelial systems. However, the addition of a maximal size for cells allows the system to dynamically determine the degree of confluency as a function of the system parameters. The observation of the E/M transition using our model extends the behavior of the vertex-based models studied previously. Whereas the traditional vertex model is constrained to be confluent, there can only be a confluent and fluid-like phase for high  $P_0$  systems. Here a whole new non-confluent phase is observed when cells are given the possibility of developing intercellular gaps, and the confluency transition is proven to not necessarily coincide with tissue aggregation and glassy transitions. As we have seen, this enables

the system to exhibit an epithelial-mesenchymal transition, as has been observed in developmental biology, wound healing, and cancer metastasis, which underscores the model’s utility in providing mechanistic insights into the behavior of biological tissues, with implications for understanding various physiological and pathological processes.

In the AFV model, it is imperative to acknowledge that isolated cells, whether entirely detached or only loosely connected with neighboring cells, are deliberately represented in a rounded configuration. This design choice, however, constitutes a deliberate simplification, as empirical observations frequently reveal that cells lacking epithelial connections tend to adopt a more elongated, spindle-like morphology. In light of this, it is imperative to consider the potential benefits of augmenting the AFV model to afford cells additional degrees of freedom, notably the capacity for elongation. This enhancement would thereby empower isolated cells to assume non-circular geometries, aligning more closely with the diverse and dynamic forms observed in biological systems. This refinement holds substantial promise for refining the model’s fidelity to experimental realities and advancing our understanding of cellular behavior in various contexts.

In addition, it is imperative to note that our model does not account for cell proliferation or apoptosis. Consequently, any alterations in cell density stemming from processes like cell division or apoptosis may lead to a phenomenon known as density-driven jamming [30]. Moreover, it is plausible that in a biological context, as cell density escalates, the principle of contact inhibition of locomotion (CIL) [120], would come into play. This would entail a reduction in the individual cell’s self-propulsion parameter ( $v_0$ ) with heightened cell density. Interestingly, even in scenarios where tissue equilibrium is maintained through a delicate balance between cell division and apoptosis, the continuous energy injection resulting from cell division would inexorably lead to tissue fluidization [121].

Incorporating alterations in number density into the model framework would introduce an additional dimension to the phase diagram of the AFV model. This avenue of exploration holds

significant promise for future research, offering the potential to unravel novel insights into the collective behavior of cells within tissues. Regarding cell-matrix interactions, it is important to acknowledge that our current model employs a simplified representation, encapsulating solely the viscous friction between cells and the extracellular matrix or substrate. However, further enriching our analysis by integrating a more comprehensive model accounting for viscoelastic cell-matrix interactions, akin to the approach advanced by Ajeti et al. [122], could yield valuable insights. This enhanced representation would provide a more accurate reflection of the intricate interplay between cells and their surrounding matrix, which is paramount in understanding a multitude of biological phenomena, including tissue morphogenesis, wound healing, and tumor invasion. This avenue warrants consideration for future investigations, as it holds the potential to refine our understanding of cellular behavior within complex tissue environments.

## **Chapter 4**

### **Summary and Outlook**

The core focus of my doctoral research revolves around the theoretical modeling and computational simulation of phase transition phenomena within biological tissues. This research encompassed two distinct yet complementary projects, both dedicated to offering profound insights into the mechanical attributes and behaviors exhibited by biological systems.

The first project delves into the rheological behavior of the Voronoi-based cell model. This inquiry entails a meticulous examination of the constitutive relations governing confluent tissues subjected to simple shear deformation. We ascertain that an initially undeformed fluid-like tissue attains a finite rigidity after a critical strain is applied, mirroring the shear-induced rigidity observed in analogous soft matter systems. Intriguingly, this shear-driven rigidity can be explained through a critical scaling analysis near the second-order critical point that governs the liquid-solid transition of the undeformed system. Additionally, we observe that a solid-like tissue exhibits a linear response only to small strains and switches to a nonlinear response at larger strains, leading to substantial stiffening. To provide a more comprehensive understanding of shear-driven rigidity and nonlinear response in tissues, we propose a mean-field formulation for cells under shear that offers a simple physical explanation. Our findings contribute to a more comprehensive understanding of the mechanical response of biological tissues to external stresses and strains. The rheology of the Voronoi-based cell models offers a unique approach to investigating the mechanical properties of biological tissues, providing a mathematical framework that accurately represents the complex cellular structure of such systems.

The second project is dedicated to an in-depth exploration of the Active Finite Voronoi (AFV) model, which offers a robust and efficient platform to simulate and analyze the dynamics of biolog-

ical tissues during the process of phase transitions. Through the AFV model, we have identified six distinct phases defined by an aggregation-segregation transition, a dynamical jamming-unjamming transition, and an epithelial-mesenchymal transition. These identified transitions furnish valuable insights into the underlying mechanisms driving phase transitions within biological systems, shedding light on the collective behavior of cells during the transition from individual, non-confluent states to collective, confluent states. By analyzing the behavior of the AFV model under varying conditions, we aim to gain a deeper understanding of the mechanisms driving phase transitions in biological systems.

In summary, my theoretical research endeavors advance our understanding of the phase transition phenomena in biological tissues. It is imperative to acknowledge their inherent nature as abstractions, inevitably simplifying the intricate dynamics of authentic biological systems. To comprehensively unravel the multifaceted interplay of cellular processes within living tissues, further experiments serve as a pivotal linchpin, enabling the validation and refinement of theoretical models while capturing the richness and complexity inherent to real biological systems. With the advent of cutting-edge imaging technologies, we now face the formidable challenge of processing and analyzing vast quantities of microscopy data. Herein lies the potential of machine learning techniques, poised to revolutionize the field by significantly expediting the quantification and interpretation of cellular behaviors [123, 124, 125]. The application of machine learning, however, necessitates a judicious approach, grounded in a rigorous theoretical framework and bolstered by robust experimental validation. This symbiosis between theoretical research, experiments, and advanced computational methodologies not only promises to enhance our understanding of complex biological systems but also furnishes a wealth of measurements that serve as crucial fodder for the development and refinement of theoretical frameworks.

## Bibliography

- [1] Pierre-François Lenne and Vikas Trivedi. Sculpting tissues by phase transitions. *Nature Communications*, 13(1):664, 2022.
- [2] Maria R D’Orsogna, Yao-Li Chuang, Andrea L Bertozzi, and Lincoln S Chayes. Self-propelled particles with soft-core interactions: patterns, stability, and collapse. *Physical review letters*, 96(10):104302, 2006.
- [3] Benno Liebchen and Hartmut Lowen. Synthetic chemotaxis and collective behavior in active matter. *Accounts of chemical research*, 51(12):2982–2990, 2018.
- [4] Gašper Kokot and Alexey Snezhko. Manipulation of emergent vortices in swarms of magnetic rollers. *Nature communications*, 9(1):1–7, 2018.
- [5] Dong Choon Hyun, Nathanael S Levinson, Unyong Jeong, and Younan Xia. Emerging applications of phase-change materials (pcms): teaching an old dog new tricks. *Angewandte Chemie International Edition*, 53(15):3780–3795, 2014.
- [6] M Cristina Marchetti. Frictionless fluids from bacterial teamwork. *Nature*, 525(7567):37–39, 2015.
- [7] Stewart A Mallory, Chantal Valeriani, and Angelo Cacciuto. An active approach to colloidal self-assembly. *Annual review of physical chemistry*, 69:59–79, 2018.
- [8] Andrea Cavagna and Irene Giardina. Bird flocks as condensed matter. *Annu. Rev. Condens. Matter Phys.*, 5(1):183–207, 2014.
- [9] Erwin Schrodinger. *What is life? The physical aspect of the living cell*. At the University Press, 1951.
- [10] Elena Vecino, F David Rodriguez, Noelia Ruzafa, Xandra Pereiro, and Sansar C Sharma. Glia–neuron interactions in the mammalian retina. *Progress in retinal and eye research*, 51:1–40, 2016.
- [11] Thomas Lecuit and Pierre-Francois Lenne. Cell surface mechanics and the control of cell

- shape, tissue patterns and morphogenesis. *Nature reviews Molecular cell biology*, 8(8):633–644, 2007.
- [12] Cameron Walker, Elijah Mojares, and Armando del Río Hernández. Role of extracellular matrix in development and cancer progression. *International journal of molecular sciences*, 19(10):3028, 2018.
- [13] Emantha Nikolopoulou, Gabriel L Galea, Ana Rolo, Nicholas DE Greene, and Andrew J Copp. Neural tube closure: cellular, molecular and biomechanical mechanisms. *Development*, 144(4):552–566, 2017.
- [14] Andy Wullaert, Marion C Bonnet, and Manolis Pasparakis. Nf- $\kappa$ b in the regulation of epithelial homeostasis and inflammation. *Cell research*, 21(1):146–158, 2011.
- [15] Marcello Guarino, Barbara Rubino, and Gianmario Ballabio. The role of epithelial-mesenchymal transition in cancer pathology. *Pathology*, 39(3):305–318, 2007.
- [16] Sabine E Groeger and Joerg Meyle. Epithelial barrier and oral bacterial infection. *Periodontology 2000*, 69(1):46–67, 2015.
- [17] Thomas Fuhs, Franziska Wetzel, Anatol W Fritsch, Xinzhi Li, Roland Stange, Steve Pawlizak, Tobias R Kießling, Erik Morawetz, Steffen Grosser, Frank Sauer, et al. Rigid tumours contain soft cancer cells. *Nature Physics*, 18(12):1510–1519, 2022.
- [18] Matthew A Heinrich, Ricard Alert, Abraham E Wolf, Andrej Košmrlj, and Daniel J Cohen. Self-assembly of tessellated tissue sheets by growth and collision. *Biorxiv*, pages 2021–05, 2021.
- [19] Ashley Rich, Richard G Fehon, and Michael Glotzer. Rho1 activation recapitulates early gastrulation events in the ventral, but not dorsal, epithelium of drosophila embryos. *Elife*, 9:e56893, 2020.
- [20] Carl-Philipp Heisenberg and Yohanns Bellaïche. Forces in tissue morphogenesis and patterning. *Cell*, 153(5):948–962, 2013.
- [21] Denis Krndija, Fatima El Marjou, Boris Guirao, Sophie Richon, Olivier Leroy, Yohanns

- Bellaïche, Edouard Hannezo, and Danijela Matic Vignjević. Active cell migration is critical for steady-state epithelial turnover in the gut. *Science*, 365(6454):705–710, 2019.
- [22] Andy Aman and Tatjana Piotrowski. Cell migration during morphogenesis. *Developmental biology*, 341(1):20–33, 2010.
- [23] Xun Wang, Matthias Merkel, Leo B. Sutter, Gonca Erdemci-Tandogan, M. Lisa Manning, and Karen E. Kasza. Anisotropy links cell shapes to tissue flow during convergent extension. *Proceedings of the National Academy of Sciences*, 117(24):13541–13551, 2020.
- [24] Denis L Weaire and Stefan Hutzler. *The physics of foams*. Oxford University Press, 1999.
- [25] Marc Durand and Howard A Stone. Relaxation time of the topological t 1 process in a two-dimensional foam. *Physical review letters*, 97(22):226101, 2006.
- [26] D. B. Staple, R. Farhadifar, J. C. Röper, B. Aigouy, S. Eaton, and F. Jülicher. Mechanics and remodelling of cell packings in epithelia. *The European Physical Journal E*, 33(2):117–127, Oct 2010.
- [27] Silvanus Alt, Poulami Ganguly, and Guillaume Salbreux. Vertex models: from cell mechanics to tissue morphogenesis. *Philosophical Transactions of the Royal Society of London B: Biological Sciences*, 372(1720):20150520, 2017.
- [28] Monirosadat Sadati, Nader Taheri Qazvini, Ramaswamy Krishnan, Chan Young Park, and Jeffrey J Fredberg. Collective migration and cell jamming. *Differentiation*, 86(3):121–125, 2013.
- [29] Dapeng Bi, J. H. Lopez, J. M. Schwarz, and M. Lisa Manning. A density-independent rigidity transition in biological tissues. *Nature Physics*, 11(12):1074–1079, 2015.
- [30] Thomas E Angelini, Edouard Hannezo, Xavier Trepat, Manuel Marquez, Jeffrey J Fredberg, and David A Weitz. Glass-like dynamics of collective cell migration. *Proceedings of the National Academy of Sciences*, 108(12):4714–4719, 2011.
- [31] Jin-Ah Park, Lior Atia, Jennifer A Mitchel, Jeffrey J Fredberg, and James P Butler. Collective migration and cell jamming in asthma, cancer and development. *Journal of cell science*,

129(18):3375–3383, 2016.

- [32] Simon Garcia, Edouard Hannezo, Jens Elgeti, Jean-François Joanny, Pascal Silberzan, and Nir S. Gov. Physics of active jamming during collective cellular motion in a monolayer. *Proceedings of the National Academy of Sciences*, 112(50):15314–15319, 2015.
- [33] Chiara Malinverno, Salvatore Corallino, Fabio Giavazzi, Martin Bergert, Qingsen Li, Marco Leoni, Andrea Disanza, Emanuela Frittoli, Amanda Oldani, Emanuele Martini, et al. Endocytic reawakening of motility in jammed epithelia. *Nature materials*, 16(5):587, 2017.
- [34] Peter Friedl and Darren Gilmour. Collective cell migration in morphogenesis, regeneration and cancer. *Nature reviews Molecular cell biology*, 10(7):445–457, 2009.
- [35] Linda Oswald, Steffen Grosser, David M Smith, and Josef A Käs. Jamming transitions in cancer. *Journal of Physics D: Applied Physics*, 50(48):483001, oct 2017.
- [36] Alessandro Mongera, Payam Rowghanian, Hannah J Gustafson, Elijah Shelton, David A Kealhofer, Emmet K Carn, Friedhelm Serwane, Adam A Lucio, James Giammona, and Otger Campàs. A fluid-to-solid jamming transition underlies vertebrate body axis elongation. *Nature*, 561(7723):401, 2018.
- [37] Jennifer A Mitchel, Amit Das, Michael J O’Sullivan, Ian T Stancil, Stephen J DeCamp, Stephan Koehler, Oscar H Ocaña, James P Butler, Jeffrey J Fredberg, M Angela Nieto, et al. In primary airway epithelial cells, the unjamming transition is distinct from the epithelial-to-mesenchymal transition. *Nature communications*, 11(1):1–14, 2020.
- [38] François Graner and James A Glazier. Simulation of biological cell sorting using a two-dimensional extended potts model. *Physical review letters*, 69(13):2013, 1992.
- [39] Reza Farhadifar, Jens-Christian Röper, Benoit Aigouy, Suzanne Eaton, and Frank Jülicher. The influence of cell mechanics, cell-cell interactions, and proliferation on epithelial packing. *Current Biology*, 17(24):2095 – 2104, 2007.
- [40] Dapeng Bi, Xingbo Yang, M. Cristina Marchetti, and M. Lisa Manning. Motility-driven glass and jamming transitions in biological tissues. *Phys. Rev. X*, 6:021011, Apr 2016.

- [41] Bo Li and Sean X. Sun. Coherent motions in confluent cell monolayer sheets. *Biophysical Journal*, 107(7):1532–1541, 2015/08/23 2015.
- [42] Eyal Teomy, David A Kessler, and Herbert Levine. Confluent and nonconfluent phases in a model of cell tissue. *Physical Review E*, 98(4):042418, 2018.
- [43] Le Yan and Dapeng Bi. Multicellular rosettes drive fluid-solid transition in epithelial tissues. *Phys. Rev. X*, 9:011029, Feb 2019.
- [44] Makiko Nonomura. Study on multicellular systems using a phase field model. *PloS one*, 7(4):e33501, 2012.
- [45] Jin-Ah Park, Jae Hun Kim, Dapeng Bi, Jennifer A. Mitchel, Nader Taheri Qazvini, Kellan Tantisira, Chan Young Park, Maureen McGill, Sae-Hoon Kim, Bomi Gweon, Jacob Notbohm, Robert Steward, Stephanie Burger, Scott H. Randell, Alvin T. Kho, Dhananjay T. Tambe, Corey Hardin, Stephanie A. Shore, Elliot Israel, David A. Weitz, Daniel J. Tschumperlin, Elizabeth P. Henske, Scott T. Weiss, M. Lisa Manning, James P. Butler, Jeffrey M. Drazen, and Jeffrey J. Fredberg. Unjamming and cell shape in the asthmatic airway epithelium. *Nat Mater*, 14(10):1040–1048, Oct 2015.
- [46] Xingbo Yang, Dapeng Bi, Michael Czajkowski, Matthias Merkel, M. Lisa Manning, and M. Cristina Marchetti. Correlating cell shape and cellular stress in motile confluent tissues. *Proceedings of the National Academy of Sciences*, 2017.
- [47] Matthias Merkel, Karsten Baumgarten, Brian P. Tighe, and M. Lisa Manning. A minimal-length approach unifies rigidity in underconstrained materials. *Proceedings of the National Academy of Sciences*, 116(14):6560–6568, 2019.
- [48] Max Born and Kun Huang. *Dynamical theory of crystal lattices*. Oxford university press, 1996.
- [49] Craig E Maloney and Anael Lemaitre. Amorphous systems in athermal, quasistatic shear. *Physical Review E*, 74(1):016118, 2006.
- [50] Xinzhi Li, Amit Das, and Dapeng Bi. Mechanical heterogeneity in tissues promotes rigidity

and controls cellular invasion. *Physical review letters*, 123(5):058101, 2019.

- [51] Andrew R. Harris, Loic Peter, Julien Bellis, Buzz Baum, Alexandre J. Kabla, and Guillaume T. Charras. Characterizing the mechanics of cultured cell monolayers. *Proceedings of the National Academy of Sciences*, 109(41):16449–16454, 2012.
- [52] Junxiang Huang, James O Cochran, Suzanne M Fielding, M Cristina Marchetti, and Dapeng Bi. Shear-driven solidification and nonlinear elasticity in epithelial tissues. *Physical Review Letters*, 128(17):178001, 2022.
- [53] AW Lees and SF Edwards. The computer study of transport processes under extreme conditions. *Journal of Physics C: Solid State Physics*, 5(15):1921, 1972.
- [54] M. P. Allen and D. J. Tildesley. *Computer Simulation of Liquids*. Clarendon Press, New York, NY, USA, 1989.
- [55] Erik Bitzek, Pekka Koskinen, Franz Gähler, Michael Moseler, and Peter Gumbsch. Structural relaxation made simple. *Phys. Rev. Lett.*, 97:170201, Oct 2006.
- [56] Michael Moshe, Mark J Bowick, and M Cristina Marchetti. Geometric frustration and solid-solid transitions in model 2d tissue. *Physical review letters*, 120(26):268105, 2018.
- [57] Stephen A. Langer and Andrea J. Liu. Effect of random packing on stress relaxation in foam. *The Journal of Physical Chemistry B*, 101(43):8667–8671, 1997.
- [58] B. A. DiDonna and T. C. Lubensky. Nonaffine correlations in random elastic media. *Phys. Rev. E*, 72:066619, Dec 2005.
- [59] C. P. Broedersz and F. C. MacKintosh. Modeling semiflexible polymer networks. *Rev. Mod. Phys.*, 86:995–1036, Jul 2014.
- [60] Morton E. Gurtin, Eliot Fried, and Lallit Anand. *The Mechanics and Thermodynamics of Continua*. Cambridge University Press, 2010.
- [61] JD Goddard. Continuum modeling of granular assemblies: quasi-static dilatancy and yield. In *Physics of dry granular media*, pages 1–24. Springer, 1998.
- [62] Piyush K. Singh, Johnny Ching-Wei Lee, Kshitish A. Patankar, and Simon A. Rogers. Re-

- visiting the basis of transient rheological material functions: Insights from recoverable strain measurements. *Journal of Rheology*, 65(2):129–144, 2021.
- [63] Sijie Tong, Navreeta K. Singh, Rastko Sknepnek, and Andrej Kosmrlj. Linear viscoelastic properties of the vertex model for epithelial tissues, 2021.
- [64] Haruki Watanabe and Ashvin Vishwanath. Criterion for stability of goldstone modes and fermi liquid behavior in a metal with broken symmetry. *Proceedings of the National Academy of Sciences*, 111(46):16314–16318, 2014.
- [65] Haruki Watanabe. Counting rules of nambu–goldstone modes. *Annual Review of Condensed Matter Physics*, 11:169–187, 2020.
- [66] Xavier Trepat, Linhong Deng, Steven S An, Daniel Navajas, Daniel J Tschumperlin, William T Gerthoffer, James P Butler, and Jeffrey J Fredberg. Universal physical responses to stretch in the living cell. *Nature*, 447(7144):592–595, 2007.
- [67] Nargess Khalilgharibi, Jonathan Fouchard, Nina Asadipour, Ricardo Barrientos, Maria Duda, Alessandra Bonfanti, Amina Yonis, Andrew Harris, Payman Mosaffa, Yasuyuki Fujita, et al. Stress relaxation in epithelial monolayers is controlled by the actomyosin cortex. *Nature physics*, 15(8):839–847, 2019.
- [68] Suzanne M. Fielding, James O. Cochran, Junxiang Huang, Dapeng Bi, and M. Cristina Marchetti. Constitutive model for the rheology of biological tissue. *Phys. Rev. E*, 108:L042602, Oct 2023.
- [69] Peter Friedl, Joseph Locker, Erik Sahai, and Jeffrey E Segall. Classifying collective cancer cell invasion. *Nature cell biology*, 14(8):777, 2012.
- [70] Raghu Kalluri and Robert A. Weinberg. The basics of epithelial-mesenchymal transition. *The Journal of Clinical Investigation*, 119(6):1420–1428, 6 2009.
- [71] Ben N.G. Giepmans and Sven C.D. van IJzendoorn. Epithelial cell-cell junctions and plasma membrane domains. *Biochimica et Biophysica Acta (BBA) - Biomembranes*, 1788(4):820–831, 2009. Apical Junctional Complexes Part II.

- [72] Ludovic Berthier and Giulio Biroli. Theoretical perspective on the glass transition and amorphous materials. *Rev. Mod. Phys.*, 83:587–645, Jun 2011.
- [73] M. C. Marchetti, J. F. Joanny, S. Ramaswamy, T. B. Liverpool, J. Prost, Madan Rao, and R. Aditi Simha. Hydrodynamics of soft active matter. *Rev. Mod. Phys.*, 85(3):11431189, 2013.
- [74] Vincent Hakim and Pascal Silberzan. Collective cell migration: a physics perspective. *Reports on Progress in Physics*, 80(7):076601, apr 2017.
- [75] Ricard Alert and Xavier Trepat. Physical models of collective cell migration. *Annual Review of Condensed Matter Physics*, 11(1):77–101, 2020.
- [76] Shuta Ishibe, J Erika Haydu, Akashi Togawa, Arnaud Marlier, and Lloyd G Cantley. Cell confluence regulates hepatocyte growth factor-stimulated cell morphogenesis in a  $\beta$ -catenin-dependent manner. *Molecular and cellular biology*, 26(24):9232–9243, 2006.
- [77] Wai Leong Tam and Robert A Weinberg. The epigenetics of epithelial-mesenchymal plasticity in cancer. *Nature medicine*, 19(11):1438–1449, 2013.
- [78] Athanasius FM Marée, Verônica A Grieneisen, and Paulien Hogeweg. The cellular potts model and biophysical properties of cells, tissues and morphogenesis. In *Single-cell-based models in biology and medicine*, pages 107–136. Springer, 2007.
- [79] Daniel L Barton, Silke Henkes, Cornelis J Weijer, and Rastko Sknepnek. Active vertex model for cell-resolution description of epithelial tissue mechanics. *PLoS computational biology*, 13(6):e1005569, 2017.
- [80] Sebastian A Sandersius and Timothy J Newman. Modeling cell rheology with the subcellular element model. *Physical biology*, 5(1):015002, 2008.
- [81] Timothy J Newman. Modeling multicellular structures using the subcellular element model. *Single-cell-based models in biology and medicine*, pages 221–239, 2007.
- [82] Mitsusuke Tarama, Kenji Mori, and Ryoichi Yamamoto. Mechanochemical subcellular-element model of crawling cells. *Frontiers in Cell and Developmental Biology*, 10:1046053,

2022.

- [83] Markus Basan, Jens Elgeti, Edouard Hannezo, Wouter-Jan Rappel, and Herbert Levine. Alignment of cellular motility forces with tissue flow as a mechanism for efficient wound healing. *Proceedings of the National Academy of Sciences*, 110(7):2452–2459, 2013.
- [84] Ali Nematbakhsh, Wenzhao Sun, Pavel A Brodskiy, Aboutaleb Amiri, Cody Narciso, Zhiliang Xu, Jeremiah J Zartman, and Mark Alber. Multi-scale computational study of the mechanical regulation of cell mitotic rounding in epithelia. *PLoS computational biology*, 13(5):e1005533, 2017.
- [85] Christopher Revell, Raphael Blumenfeld, and Kevin J Chalut. Force-based three-dimensional model predicts mechanical drivers of cell sorting. *Proceedings of the Royal Society B*, 286(1895):20182495, 2019.
- [86] Sangwoo Kim, Marie Pochitaloff, Georgina A Stooke-Vaughan, and Otger Campàs. Embryonic tissues as active foams. *Nature Physics*, pages 1–8, 2021.
- [87] Dennis Wenzel and Axel Voigt. Multiphase field models for collective cell migration. *Physical Review E*, 104(5):054410, 2021.
- [88] Adrian Moure and Hector Gomez. Phase-field model of cellular migration: Three-dimensional simulations in fibrous networks. *Computer Methods in Applied Mechanics and Engineering*, 320:162–197, 2017.
- [89] EABF Lima, JT Oden, and RC Almeida. A hybrid ten-species phase-field model of tumor growth. *Mathematical Models and Methods in Applied Sciences*, 24(13):2569–2599, 2014.
- [90] Leonid Berlyand, Mykhailo Potomkin, and Volodymyr Rybalko. Phase-field model of cell motility: Traveling waves and sharp interface limit. *Comptes Rendus. Mathématique*, 354(10):986–992, 2016.
- [91] Benjamin Loewe, Michael Chiang, Davide Marenduzzo, and M Cristina Marchetti. Solid-liquid transition of deformable and overlapping active particles. *Physical Review Letters*, 125(3):038003, 2020.

- [92] Amin Doostmohammadi, Sumesh P Thampi, Thuan B Saw, Chwee T Lim, Benoit Ladoux, and Julia M Yeomans. Celebrating soft matter’s 10th anniversary: Cell division: a source of active stress in cellular monolayers. *Soft Matter*, 11(37):7328–7336, 2015.
- [93] Junxiang Huang, Herbert Levine, and Dapeng Bi. Bridging the gap between collective motility and epithelial–mesenchymal transitions through the active finite voronoi model. *Soft Matter*, 2023.
- [94] M. Lisa Manning, Ramsey A. Foty, Malcolm S. Steinberg, and Eva-Maria Schoetz. Coaction of intercellular adhesion and cortical tension specifies tissue surface tension. *Proceedings of the National Academy of Sciences*, 107(28):12517–12522, Jul 2010.
- [95] Susan E. Leggett, Zachary J. Neronha, Dhananjay Bhaskar, Jea Yun Sim, Theodora Myrto Perdikari, and Ian Y. Wong. Motility-limited aggregation of mammary epithelial cells into fractal-like clusters. *Proceedings of the National Academy of Sciences*, 116(35):17298–17306, Aug 2019.
- [96] Nicoletta I Petridou, Bernat Corominas-Murtra, Carl-Philipp Heisenberg, and Edouard Hannezo. Rigidity percolation in embryo morphogenesis: Physics meets biology (again). *Cell*, 184(7):1914–1928, 2021.
- [97] Doris Meder, Maria Joao Moreno, Paul Verkade, Winchil LC Vaz, and Kai Simons. Phase coexistence and connectivity in the apical membrane of polarized epithelial cells. *Proceedings of the National Academy of Sciences*, 103(2):329–334, 2006.
- [98] Cristián Huepe and Maximino Aldana. Intermittency and clustering in a system of self-driven particles. *Physical Review Letters*, 92(16):168701, Apr 2004.
- [99] Yingzi Yang, Vincent Marceau, and Gerhard Gompper. Swarm behavior of self-propelled rods and swimming flagella. *Physical Review E*, 82(3):031904, Sep 2010.
- [100] Marjolein N. van der Linden, Lachlan C. Alexander, Dirk G. A. L. Aarts, and Olivier Dauchot. Interrupted motility induced phase separation in aligning active colloids. *Physical Review Letters*, 123(9):098001, Aug 2019.

- [101] Demian Levis and Ludovic Berthier. Clustering and heterogeneous dynamics in a kinetic monte carlo model of self-propelled hard disks. *Physical Review E*, 89(6):062301, Jun 2014.
- [102] Gabriel S. Redner, Caleb G. Wagner, Aparna Baskaran, and Michael F. Hagan. Classical nucleation theory description of active colloid assembly. *Physical Review Letters*, 117(14):148002, Sep 2016.
- [103] Emanuela Zaccarelli. Colloidal gels: equilibrium and non-equilibrium routes. *Journal of Physics: Condensed Matter*, 19(32):323101, Aug 2007.
- [104] Jean Paul Thiery, Hervé Acloque, Ruby YJ Huang, and M Angela Nieto. Epithelial-mesenchymal transitions in development and disease. *cell*, 139(5):871–890, 2009.
- [105] Samy Lamouille, Jian Xu, and Rik Deryck. Molecular mechanisms of epithelial-mesenchymal transition. *Nature reviews Molecular cell biology*, 15(3):178–196, 2014.
- [106] Junichi Ikenouchi, Miho Matsuda, Mikio Furuse, and Shoichiro Tsukita. Regulation of tight junctions during the epithelium-mesenchyme transition: direct repression of the gene expression of claudins/occludin by snail. *Journal of cell science*, 116(10):1959–1967, 2003.
- [107] Daisuke Kyuno, Akira Takasawa, Shin Kikuchi, Ichiro Takemasa, Makoto Osanai, and Takashi Kojima. Role of tight junctions in the epithelial-to-mesenchymal transition of cancer cells. *Biochimica et Biophysica Acta (BBA)-Biomembranes*, 1863(3):183503, 2021.
- [108] Jeffrey D Amack. Cellular dynamics of emt: lessons from live in vivo imaging of embryonic development. *Cell Communication and Signaling*, 19(1):1–16, 2021.
- [109] Susan E Leggett, Jea Yun Sim, Jonathan E Rubins, Zachary J Neronha, Evelyn Kendall Williams, and Ian Y Wong. Morphological single cell profiling of the epithelial-mesenchymal transition. *Integrative Biology*, 8(11):1133–1144, 2016.
- [110] Robert Nunan, Jessica Campbell, Ryoichi Mori, Mara E Pitulescu, Wen G Jiang, Keith G Harding, Ralf H Adams, Catherine D Nobes, and Paul Martin. Ephrin-bs drive junctional downregulation and actin stress fiber disassembly to enable wound re-epithelialization. *Cell reports*, 13(7):1380–1395, 2015.

- [111] M Angela Nieto, Ruby Yun-Ju Huang, Rebecca A Jackson, and Jean Paul Thiery. Emt: 2016. *Cell*, 166(1):21–45, 2016.
- [112] Lior Atia, Dapeng Bi, Yasha Sharma, Jennifer A Mitchel, Bomi Gweon, Stephan A Koehler, Stephen J DeCamp, Bo Lan, Jae Hun Kim, Rebecca Hirsch, et al. Geometric constraints during epithelial jamming. *Nature physics*, 14(6):613–620, 2018.
- [113] Alberto Puliafito, Lars Hufnagel, Pierre Neveu, Sebastian Streichan, Alex Sigal, D. Kuchnir Fygenson, and Boris I. Shraiman. Collective and single cell behavior in epithelial contact inhibition. *Proceedings of the National Academy of Sciences*, 109(3):739–744, Jan 2012.
- [114] Matthew A Heinrich, Ricard Alert, Julienne M LaChance, Tom J Zajdel, Andrej Košmrlj, and Daniel J Cohen. Size-dependent patterns of cell proliferation and migration in freely-expanding epithelia. *eLife*, 9:e58945, Aug 2020.
- [115] Bernd Schierwater. My favorite animal, trichoplax adhaerens. *BioEssays*, 27(12):1294–1302, 2005.
- [116] Vivek N Prakash, Matthew S Bull, and Manu Prakash. Motility-induced fracture reveals a ductile-to-brittle crossover in a simple animal’s epithelia. *Nature Physics*, 17(4):504–511, 2021.
- [117] P Bronsert, K Enderle-Ammour, M Bader, S Timme, M Kuehs, A Csanadi, G Kayser, I Kohler, D Bausch, J Hoeppner, et al. Cancer cell invasion and emt marker expression: a three-dimensional study of the human cancer–host interface. *The Journal of pathology*, 234(3):410–422, 2014.
- [118] Alexandru Dan Grigore, Mohit Kumar Jolly, Dongya Jia, Mary C Farach-Carson, and Herbert Levine. Tumor budding: the name is emt. partial emt. *Journal of clinical medicine*, 5(5):51, 2016.
- [119] Mrinmoy Mukherjee and Herbert Levine. Cluster size distribution of cells disseminating from a primary tumor. *PLOS Computational Biology*, 17(11):e1009011, 2021.
- [120] Roberto Mayor and Carlos Carmona-Fontaine. Keeping in touch with contact inhibition of

locomotion. *Trends in Cell Biology*, 20(6):319–328, 2010.

- [121] Yiwen Tang, Siyuan Chen, Mark J Bowick, and Dapeng Bi. Cell division and motility enable hexatic order in biological tissues. *arXiv preprint arXiv:2303.00129*, 2023.
- [122] Visar Ajeti, A Pasha Tabatabai, Andrew J Fleszar, Michael F Staddon, Daniel S Seara, Cristian Suarez, M Sulaiman Yousafzai, Dapeng Bi, David R Kovar, Shiladitya Banerjee, et al. Wound healing coordinates actin architectures to regulate mechanical work. *Nature physics*, 15(7):696–705, 2019.
- [123] Erick Moen, Dylan Bannon, Takamasa Kudo, William Graf, Markus Covert, and David Van Valen. Deep learning for cellular image analysis. *Nature methods*, 16(12):1233–1246, 2019.
- [124] Carsen Stringer, Tim Wang, Michalis Michaelos, and Marius Pachitariu. Cellpose: a generalist algorithm for cellular segmentation. *Nature methods*, 18(1):100–106, 2021.
- [125] Zhichao Liu, Luhong Jin, Jincheng Chen, Qiuyu Fang, Sergey Ablameyko, Zhaozheng Yin, and Yingke Xu. A survey on applications of deep learning in microscopy image analysis. *Computers in biology and medicine*, 134:104523, 2021.